THE UNIVERSITY OF CHICAGO

A MEASUREMENT OF THE E-MODE POLARIZATION OF THE COSMIC MICROWAVE BACKGROUND WITH SPT-3G

A DISSERTATION SUBMITTED TO
THE FACULTY OF THE DIVISION OF THE PHYSICAL SCIENCES
IN CANDIDACY FOR THE DEGREE OF
DOCTOR OF PHILOSOPHY

DEPARTMENT OF PHYSICS

BY
DANIEL PHILLIP DUTCHER

CHICAGO, ILLINOIS
DECEMBER 2020

TABLE OF CONTENTS

LIST OF FIGURES

All figures by author unless otherwise indicated.

LIST OF TABLES

ACKNOWLEDGMENTS

SPT is a sizable collaboration—one I've been with for several years—and there are many people who have helped me along the way. I owe a large debt of gratitude to Joshua Montgomery, Adam Jones, Steele Diggles, and the entirety of the South Pole Winterover crew, without whose heroic efforts during the winter of 2018 the data used for this thesis would not exist. I'd like to thank John Carlstrom for supporting me throughout my long graduate career, Amy Bender for her mentorship, Brad Benson for his guidance and careful playlist curation, and Tom Crawford for being an excellent role model while providing a continuous supply of pastries for group meeting. I would also like to thank Tyler Natoli for initially instructing me in the ways of the lab, Zhaodi Pan for being my trusty labmate and CMBFF all these years, and all of the SPTweens for making SPT a truly great environment in which to work. I would also like to thank Jason Henning for all of his advice and code that I made good use of, and Lennart Balkenhol for his invaluable work on the covariance matrix, likelihood, and parameter constraints. And of course I have to acknowledge my absolutely perfect partner Cici, who has never stopped supporting me even though I went to the South Pole three times and never called. Du bist mein Lebenslangerschicksalsschatz und Herzallerliebste.

ABSTRACT

Observations of the cosmic microwave background (CMB) form the pillar of our current understanding of cosmology. Maps of the temperature and polarization anisotropies of the CMB encode information about the initial conditions of the universe, its matter and energy content, and its evolution over time, setting tight constraints on the parameters of the ΛCDM cosmological model and probing the physics of inflation. Making these exquisitely precise measurements requires building increasingly sensitive instruments, with larger focal plane areas and ever-greater detector counts. SPT-3G is the latest CMB survey instrument to be installed on the 10-meter South Pole Telescope, utilizing both a larger focal plane and multi-chroic pixels to raise the detector count to $\sim$ 16,000, a tenfold increase over its predecessor. SPT-3G will conduct a multi-year survey of a 1500 deg^2 patch of sky, producing maps with an unprecedented combination of depth and angular resolution and improving constraints on the CMB power spectrum by over an order of magnitude at small angular scales. In this thesis, I describe the SPT-3G instrument, with special focus on the development and testing of the detectors. I present an analysis of data taken by SPT-3G during the 2018 observing season to produce a measurement of the E-mode polarization power spectrum and temperature-E-mode cross-power spectrum of the CMB over the angular multipole range $300 \leq \ell < 3000$, and I state the resulting constraints on cosmological parameters.

CHAPTER 1

INTRODUCTION

The cosmic microwave background (CMB) is the oldest light in the universe, produced just a few hundred thousand years after the Big Bang. The ripples in this relic radiation form a snapshot of the matter and energy distribution in the early universe, providing an incredibly rich source of information from which to learn about the beginning and eventual fate of the universe. SPT-3G is a new instrument designed to measure the CMB with an incredible combination of sensitivity and angular resolution, sharpening our understanding of cosmology and revealing any mysteries still waiting to be explored. I have spent my graduate career working on SPT-3G, joining the collaboration from essentially its inception, and have been involved with very nearly every aspect of the experiment through all stages of development; from initial planning and design, to construction and deployment, to daily operation and production of scientific results. I attempt to touch on all of these aspects in this thesis, organized as follows.

The remainder of this Introduction provides some background on the CMB, what it is and why we study it. In Chapter 2 I discuss the South Pole site, the 10-meter South Pole Telescope, and the larger design elements of SPT-3G, including the optical coupling and the receiver cryostat. The readout system and electronics are discussed in Chapter 3, while the development and characterization of the detectors is presented in Chapter 4. In Chapter 5 I detail the process of making CMB maps with SPT-3G, including the survey field, scan strategy, and the filtering choices I used for making maps with data collected during 2018. The thesis culminates in an analysis of this data to produce a measurement of the E-mode polarization power spectrum and temperature-E-mode (TE) cross-power spectrum of the CMB, and the application of these measurements to constrain cosmological parameters. Details of the analysis are discussed in Chapter 6, and the results are presented in Chapter 7.

1.1 The Cosmic Microwave Background

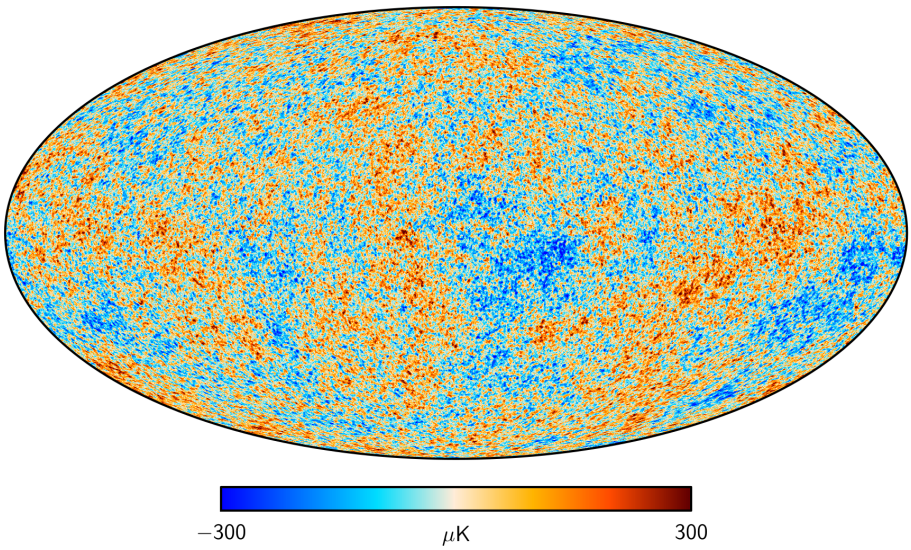

Figure 1.1: All-sky temperature map of the CMB, as seen by the *Planck* satellite. Image credit: Planck Collaboration et al. (2020a).

We live in an expanding universe. Some of the earliest evidence for this dates to when Hubble (1929) used the Doppler-shifted emission lines of galaxies to plot their radial velocity as a function of distance, finding the basic linear relation $v = H_0 d$. This relation between distance and recessional velocity is precisely what is to be expected for an isotropic and homogeneous expansion, every point in the universe moving away from every other point. The interpretation of Hubble's data as indicating an expanding universe was made by Lemaître (1931a,b), who further went on to posit that if one were to rewind this expansion backwards in time, all matter in the (visible) universe would contract to a single point.

This primeval universe would be incredibly hot and dense, with matter broken down into its fundamental particles. Standard thermodynamics tells us that as the universe expands, its temperature decreases, eventually allowing protons and neutrons to form, and (much) later, electrons and protons to bind together into neutral atoms. Photons, which until this point had been in equilibrium with and bound-up by free electrons, would now be able to travel through the universe unimpeded. These photons are still visible to us today, with their wavelengths stretched by the ratio of the size of the universe now with the size of the universe

at the time of their decoupling, placing them in the microwave region of the electromagnetic spectrum (Dicke et al. 1965). This radiation was detected by Penzias & Wilson (1965) and has come to be known as the cosmic microwave background.

Fast-forward half a century, and we now have exquisitely detailed maps of the CMB across the entire sky, as shown in Figure 1.1, providing a snapshot of the universe from a mere 380,000 years after the Big Bang. While the intensity of the CMB corresponds to a remarkably uniform temperature of 2.726 K (Fixsen 2009), there are $\mathcal{O}(100\,\mu\mathrm{K})$ deviations across the sky, corresponding to regions of space just slightly colder or warmer than average. These anisotropies, as they are called, result from quantum fluctuations in the distribution of matter in the very early universe, tiny density perturbations that have been stretched by cosmic inflation to cosmological scales, seeding the growth of the large-scale structure observed in the universe today. The statistical properties of the anisotropies—specifically their deviation about the mean as a function of angular size, a measure known as the power spectrum—contain a wealth of information. Studies of the CMB have revealed a strange universe, one dominated by the effects of dark matter and dark energy, giving rise to the standard ΛCDM cosmological model—"Λ" for Einstein's cosmological constant, which may or may not describe dark energy, and "CDM" for cold (non-relativistic) dark matter. The ΛCDM model describing our universe is parameterized by just six numbers, listed at the top of Table 1.1, with combinations of these numbers yielding the age of the universe; the energy contributions of normal matter, dark matter, and dark energy; the spatial curvature of the universe; and more. These parameters are extracted from observations of the CMB by fitting its power spectrum to ΛCDM predictions, typically solved for by fast Boltzmann codes such as CAMB (Lewis et al. 2000).[1] An in-depth discussion of the effects of specific parameters on the shape of the CMB power spectrum can be found in, e.g., Hu & Dodelson (2002).

1. https://camb.info/

Symbol	Value	Description
Free		
$\Omega_{\rm b}h^2$	$(2.242 \pm 0.014) \times 10^{-2}$	Physical baryon density parameter
$\Omega_{\rm c}h^2$	0.11933 ± 0.00091	Physical dark matter density parameter
θ_*	$0.0104119 \pm 2.9{\times}10^{-6}$	Angular scale of sound horizon at recombination
τ	0.0561 ± 0.0071	Optical depth to reionization
$A_{\rm s}$	$(2.105 \pm 0.030) \times 10^{-9}$	Amplitude of primordial scalar fluctuations
$n_{\rm s}$	0.9665 ± 0.0038	Scalar spectral index
Derived		
Ω_Λ	0.6889 ± 0.0056	Dark energy density parameter
$\Omega_{\rm m}$	0.3111 ± 0.0056	Matter density parameter
H_0	67.66 ± 0.42	Hubble parameter today, in $\mathrm{km\,s^{-1}\,Mpc^{-1}}$
t_0	13.787 ± 0.020	Age of the universe today, in Gyr
σ_8	0.8102 ± 0.0060	Matter fluctuation amplitude
Fixed		
r	0	Tensor-to-scalar ratio
$\sum m_\nu$	$0.06\,\mathrm{eV}/c^2$	Sum of neutrino masses
$N_{\rm eff}$	3.046	Effective number of relativistic particle species
$\Omega_{\rm tot}$	1	Total energy density parameter
$\frac{dn_{\rm s}}{d\ln k}$	0	Running of the scalar spectral index
w	1	Dark energy equation of state

Table 1.1: Symbols and descriptions of parameters in the ΛCDM model, with values obtained from a combination of CMB, gravitational lensing, and baryon-acoustic oscillation measurements (Planck Collaboration et al. 2020b). The Free parameters are typically taken as the base set, and a large number of Derived parameters may be constructed from combinations of them, a small sample of which is shown here. The Fixed parameters describe base ΛCDM, but they can be allowed to vary to probe model extensions. $\Omega_{\rm x}$ parameters indicate the energy density of the specified component as a fraction of the critical density $\rho_{\rm c}(t) = 3H^2/8\pi G$, and h represents the parameterization of the Hubble constant as $H_0 = 100h\,\mathrm{km\,s^{-1}\,Mpc^{-1}}$.

1.1.1 CMB Polarization

Light from the CMB anisotropies is polarized near the 10% level. Figure 1.2 demonstrates how a quadrupole anisotropy, in which hot and cold regions are separated by 90°, can give rise to linear polarization in the scattered light (Hu & White 1997). In the scattering process, incoming light causes an electron to oscillate along the direction of electric field vector, perpendicular to the direction of light propagation. In the diagram, the electron at center will have larger oscillations in the vertical direction caused by the more intense radiation from the hotter region at left, and smaller oscillations in the horizontal direction. Light that is re-radiated out of the page will therefore be partially polarized along the vertical axis.

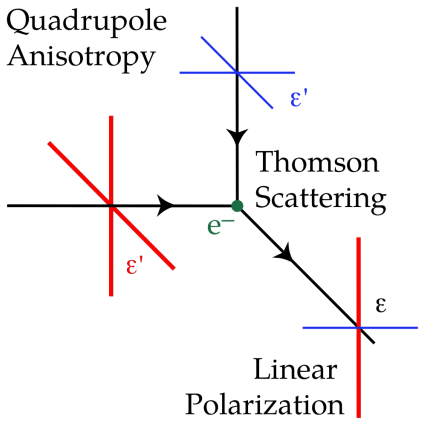

Figure 1.2: Diagram demonstrating linear polarization resulting from a quadrupole temperature anisotropy. The electron at the center scatters unpolarized light from the hotter region at left and the colder region above, resulting in net linear polarization in the scattered light coming out of the page. Figure from Hu & White (1997).

Analogous to the standard Helmholtz decomposition of a vector field, the resulting pattern of linear polarization across the sky can be decomposed into curl-free and divergence-free components, here referred to as "E-modes" and "B-modes", respectively, where the names of each mode are in reference to the similar properties of electric and magnetic field vectors. The polarization patterns associated with each of these modes are depicted in Figure 1.3. Decomposing the polarization field in this way has two key benefits: firstly, these modes are rotationally invariant and do not depend on the orientation of local coordinate axes (e.g., in

the manner that Stokes parameters do), and secondly—and more importantly—these two types of polarization are sourced by different physical processes: to first order, density perturbations can only create E-modes, while B-modes are only created by gravitational waves or gravitational lensing (Seljak & Zaldarriaga 1997; Kamionkowski et al. 1997).

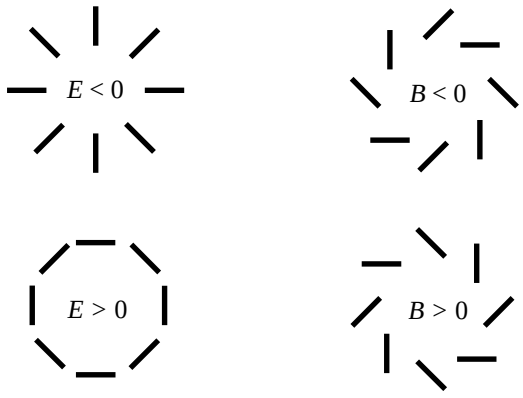

Figure 1.3: Polarization patterns for E- and B-modes

There are several advantages to measuring the polarization properties of the CMB. First and foremost, the E-mode power spectrum alone provides better constraints on cosmological parameters than measuring the temperature power spectrum alone (Galli et al. 2014). As the polarization is generated at the surface of last scattering, it is a more direct probe of the CMB than temperature fluctuations, which are more susceptible to late-time effects and foreground contamination (Hu & White 1997). Bright point sources dominate the temperature power spectrum at small angular scales (Reichardt et al. 2020; Louis et al. 2017), but, as these sources are mostly unpolarized (Gupta et al. 2019; Datta et al. 2019; Trombetti et al. 2018), the E-mode power spectrum remains relatively pure. Temperature and polarization also provide separate measures of the same underlying physics, and thus can help to break parameter degeneracies that might be present if only one field were to be measured. Lastly, the B-mode power spectrum is a unique probe of the physics of cosmic inflation, during which time tensor perturbations to the metric produced primordial gravitational waves.

1.1.2 *Measurements of the CMB*

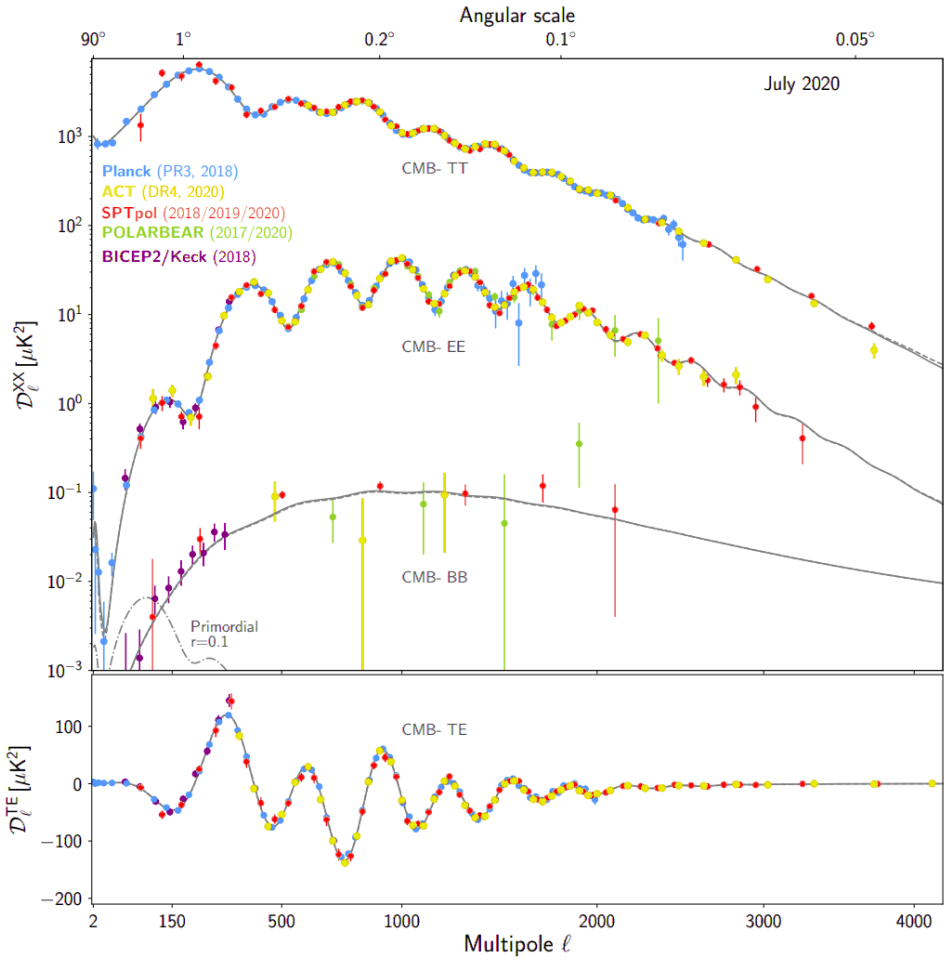

Figure 1.4: Recent measurements of CMB temperature and polarization power spectra. The B-modes measured so far are produced by gravitational lensing of E-modes; the primordial B-modes from inflation remain to be measured. Figure from Choi et al. (2020).

Figure 1.4 shows a compilation of recent measurements of the CMB temperature and polarization power spectra. Satellite missions such as *Planck* (Planck Collaboration et al. 2020a) measure the CMB across the entire sky, while ground-based instruments such as ACTpol (Choi et al. 2020), POLARBEAR (Adachi et al. 2020), BICEP/Keck, (BICEP2 and Keck Array Collaborations et al. 2018) and SPTpol (Henning et al. 2018) obtain very deep images of select patches of sky, and both methods provide exceedingly tight constraints on

cosmological parameters. So far all measurements seem to be consistent with ΛCDM, though there are some interesting tensions between experiments to be explored further. B-modes caused by inflation are also yet to be measured. Gravitational lensing distorts the much stronger E-modes into lensed B-modes, obscuring the signal from primordial gravitational waves; with more precise measurements and modeling, the contaminating signal from lensed B-modes may be removed, uncovering the underlying inflationary B-modes.

Measurements of the CMB made from the ground are typically "background-limited," with photon noise from the much brighter atmosphere dominating over noise inherent to the detectors, so the only way to build more sensitive instruments is to use more detectors and average down the noise. So-called third-generation instruments with several thousand to tens of thousands of detectors are either in the initial phases of deployment or already collecting data, including Advanced ACTpol (Henderson et al. 2016), POLARBEAR-2/Simons Array (Suzuki et al. 2016), and BICEP Array (Hui et al. 2018). This thesis centers on SPT-3G (Benson et al. 2014), the third-generation CMB survey camera recently deployed on the South Pole Telescope.

CHAPTER 2

THE SOUTH POLE TELESCOPE

2.1 The Site

The South Pole is among the best sites on Earth for mm-wave astronomy, due to its high elevation (2835 m [9310 feet]), dry atmosphere (0.25 mm precipitable water vapor (Chamberlin 2001)), and stable observing conditions, caused in part by the lack of a 24 h day-night cycle. Operations at the site are supported by the Amundsen-Scott South Pole Station (Figure 2.1), a research station originally established in 1957 by the US Navy Seabees and currently administered by the United States Antarctic Program under the National Science Foundation's Office of Polar Programs. Transportation to the site is primarily via Lockheed LC-130 aircraft, departing from McMurdo Station located on the coast of Antarctica in the Ross Sea, with a flight duration of 3 hours. Personnel are flown to McMurdo from Christchurch, New Zealand either by LC-130 (flight time 7 hours) or Boeing C-17 (flight time 5 hours), depending on the time of year. The South Pole station is only accessible during the austral summer season of November–February, during which time approximately 150 people live and work at the station, while during the rest of the year it is isolated and operated by a ∼40-person winterover crew.

Figure 2.1: The Amundsen-Scott South Pole Station. The modern elevated station building was officially dedicated in 2008.

Over the last three decades several telescopes have been built at the South Pole to take

advantage of its excellent site characteristics in order to make ground-breaking observations of the CMB, with notable examples including Python, Viper, DASI, QUaD, the BICEP/Keck series of experiments, and, of course, the 10-meter South Pole Telescope (Figure 2.2).

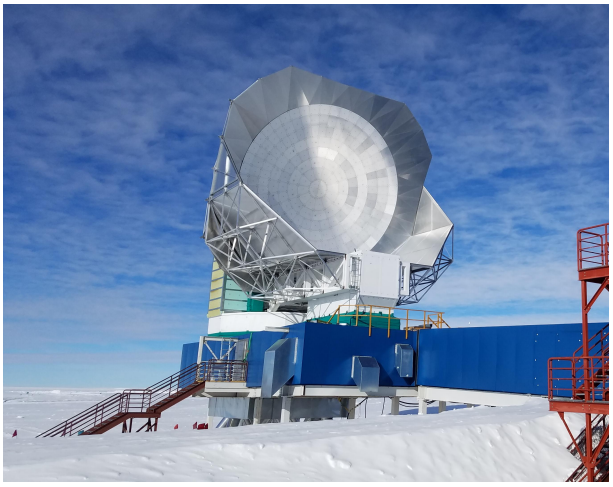

Figure 2.2: The South Pole Telescope.

The South Pole Telescope (SPT) is an off-axis Gregorian telescope with a segmented 10 m primary mirror designed for arcminute-resolution imaging at millimeter wavelengths (Carlstrom et al. 2011). First constructed over the 2006–2007 austral summer season, SPT has since been fitted with three successive generations of camera, each being used for dedicated surveys of the CMB and mm-wave sky. The SPT Sunyaev-Zel'dovich (SPT-SZ) survey took place over 2007–2011 and mapped 2500 $\deg^2$ of sky using 960 intensity-sensitive detectors across three frequency bands centered at 95, 150, and 220 GHz. SPT-SZ was succeeded by SPTpol (2012–2016) (Austermann et al. 2012), which used ∼1600 polarization-sensitive detectors at 95 and 150 GHz to primarily observe a 500 $\deg^2$ subset of the SPT-SZ field, measuring both the temperature and polarization properties of the CMB. The latest survey instrument to be installed on the South Pole Telescope, and the focus of this thesis, is SPT-3G.

2.2 The SPT-3G Instrument

SPT-3G is a major upgrade over the previous instruments on SPT, and it includes changes to essentially every telescope system downstream of the primary mirror. The secondary telescope optics are redesigned to illuminate a larger focal plane area, new optics and detector cryostats are built to house the larger lenses and detector cold stage, and the readout electronics are upgraded to a new system with a 5×-higher multiplexing factor. The 0.43 m-diameter focal plane, pictured in Figure 2.3, has been filled with dual-polarized pixels that are simultaneously sensitive to 95, 150, and 220 GHz frequency bands, achieving a ten-fold increase in detector count over SPTpol. SPT-3G was deployed on the telescope in early 2017, and it is currently conducting a multi-year survey of a 1500 $\deg^2$ field.

In this section, I give an overview of the optical design of SPT-3G and the construction of its optics and detector cryostats. In Chapter 3, I discuss the elements of the readout system, while the detectors are covered in Chapter 4.

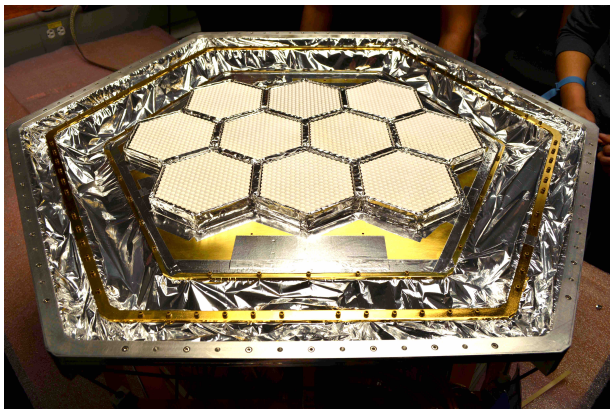

Figure 2.3: Photograph of the SPT-3G focal plane populated with ten detector modules. Photo courtesy of Brad Benson.

2.2.1 Optics and Receiver Design

Light rays from the 10 m primary mirror are focused at the end of the telescope boom, passing through a foam environmental window before entering the receiver cabin. Inside the cabin, a 2 m ellipsoidal secondary mirror redirects the light from prime focus onto a 1 m flat

tertiary mirror, which then sends the light downwards into the receiver cryostat, forming the Gregorian focus just external to the receiver window (see Figure 2.4). The additional coupling mirrors and receiver cryostat are mounted to an actuated optics bench that can be adjusted to maintain alignment with the primary. This wide-field coupling design replaces the cold secondary mirror used by both SPT-SZ and SPTpol, providing a larger field of view (2.8 $\deg^2$ compared to $\sim$1 $\deg^2$) and illuminating a 3.5$\times$ larger focal plane area.

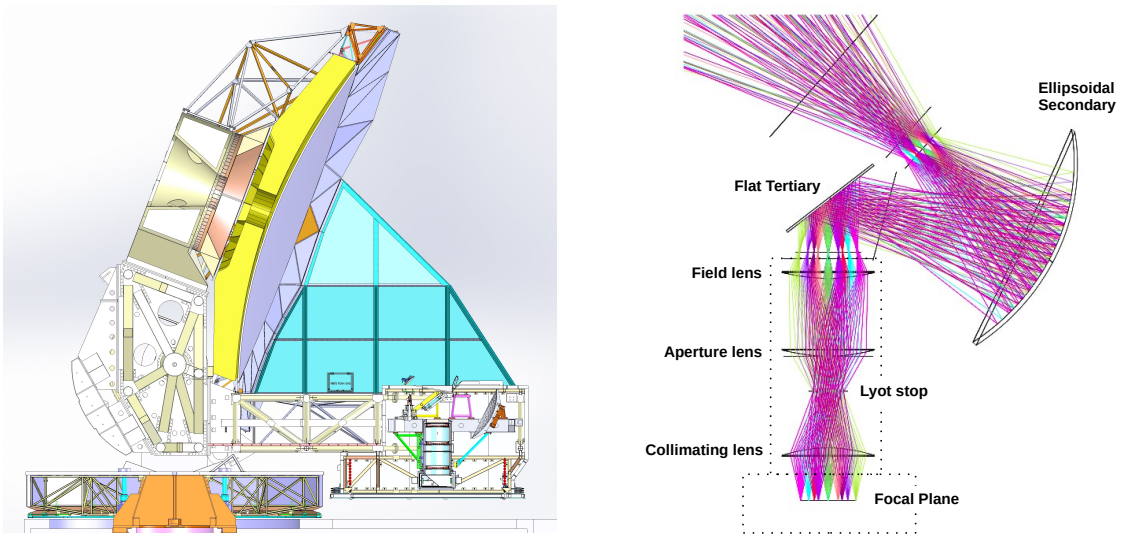

Figure 2.4: *Left:* Cross section of SPT with 10 m primary mirror. The cabin containing the receiver cryostat is at bottom right. *Right:* Ray-trace of the SPT-3G optics inside the receiver cabin (Benson et al. 2014). The coupling mirrors are at ambient temperature, while the lenses inside the cryostat (indicated by the dotted line) are held at 4 K.

The SPT-3G receiver, a cutaway rendering of which is shown in Figure 2.5, is described in Sobrin et al. (2018) and can be functionally divided into the optics and detector cryostats. The optics cryostat is cylindrical in shape, approximately 1.7 m long and 1 m in diameter, and contains the lenses that re-image the Gregorian focus onto the detectors in the focal plane. The re-imaging optics consist of three 0.72 m diameter plano-convex CoorsTek[1] alumina lenses cooled to 4 K. Each lens has a broadband antireflection (AR) coating consisting of a trilayer of polytetrafluoroethylene (PTFE) (Nadolski et al. 2020), designed to increase

1. https://www.coorstek.com/

transmission over the range 75 GHz–250 GHz.

The optics cryostat also contains a series of filters that reduce incident thermal and out-of-band radiation, so as to not overburden the cryostat cold stages or cause excess noise in the detectors. Light enters the optics cryostat through a high-density polyethylene (HDPE) vacuum window, into which a series of triangular grooves has been cut to serve as an effective broadband AR coating. On the underside of the window, a stack of Zotefoams[2] Plastazote HD30 serves as an infrared filter, with the layers thermally isolated from each other by G10 spacers, allowing successive layers to cool via radiative heat transfer. A 15 mm-thick flat alumina disc mounted at 50 K, of the same material and with the same PTFE-based AR coating as the lenses, serves as an additional infrared filter. A 0.28 m Lyot stop between the aperture and collimating lenses limits the beam illumination to the central 8 m of the primary mirror, reducing side lobes and possible pick-up of signals emitted from the ground. A metal mesh filter (Tucker & Ade 2006) mounted at the Lyot stop limits radiation above 300 GHz from impinging on the detectors. The internal metal surfaces of the optics cryostat are covered with Eccosorb[3] HR-10 to absorb stray reflections, and a series of baffling rings between the aperture and field lenses further limits any stray light rays.

The cryostat design uses three nested shells operating at progressively lower temperatures, corresponding to approximately 300 K, 50 K, and 4 K, where the shells are mechanically supported by a thermally-isolating G10 truss and cooled by two CryoMech[4] PT415 pulse-tube coolers, one on each of the detector and optics cryostats. Each shell serves as a radiation shield for the subsequent layer, with the 300 K layer providing the vacuum jacket. To reduce radiative loading from the 300 K shell, the 50 K shell is covered with multi-layer insulation consisting of aluminized mylar sheets thermally separated by a thin polyester scrim. This insulation layer is not required on the 4 K shell, as the dominant source of thermal loading

2. https://www.zotefoams.com/

3. https://www.laird.com/

4. https://www.cryomech.com/

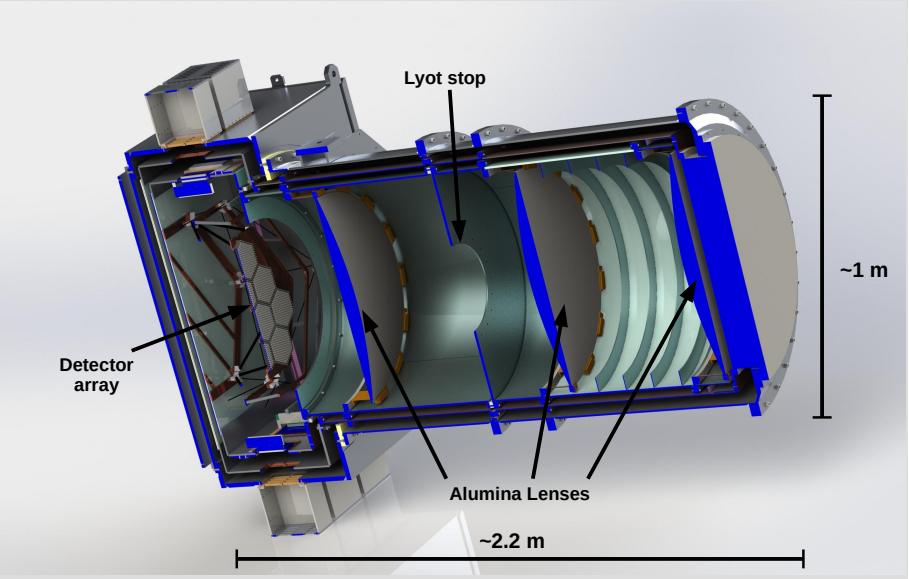

Figure 2.5: Cutaway rendering of the SPT-3G receiver (Nadolski et al. 2020). The cylindrical portion on the right houses the reimaging optics and optical filters, while the box on the left contains the detectors and their associated readout.

there is not radiation but rather conduction from the mechanical support truss. While the 300 K shell is made from aluminum 6061, the 50 K and 4 K shells are constructed from the slightly purer aluminum 1100, which exhibits better thermal conductivity at cryogenic temperatures (Woodcraft 2005). To further reduce thermal gradients across the optics cryostat, strips of high-purity 99.999% (5N) aluminum are clamped to the 4 K shell.

The detector cryostat houses the detectors and the associated cold readout electronics. The detectors are cooled to their operational temperature of ∼300 mK by a custom closed-cycle three-stage ^{4}He-^{3}He-^{3}He sorption refrigerator manufactured by Chase Research Cryogenics[5]. The detectors are installed on a tiered sub-Kelvin assembly (Figure 2.6), with each gold-plated stage thermally connected to the corresponding fridge stage with a braided oxygen-free high-conductivity (OFHC) copper heat strap and mechanically stood off from the other stages by Graphlite[6] carbon rods, a proprietary form of carbon fiber reinforced polymer (CFRP). A thin sheet of aluminized mylar is installed between the stages of the

5. http://www.chasecryogenics.com/

6. https://marskeaircraft.com/

sub-Kelvin assembly to isolate the radio frequency (RF) environments of the optics and detector cryostats, preventing RF noise that enters the cryostat window from affecting the readout electronics.

In early 2018, problems with the telescope drive system caused the cryostat to undergo repeated rapid accelerations, resulting in failure of the CFRP rods in the sub-Kelvin assembly and damage to some of the connected detector readout. The South Pole winterover crew opened the cryostat and repaired the assembly with a spare set of CFRP rods, and observations were able to resume for the latter half of 2018 with a repaired drive system and reduced detector count. During the austral summer of 2018–2019, the damaged readout was replaced, and a new sub-Kelvin assembly was installed that utilizes a redesigned truss structure and aluminum thermal stages instead of copper to reduce weight and increase structural rigidity. We have since seen nominal performance in the subsequent 2019 and 2020 observing seasons.

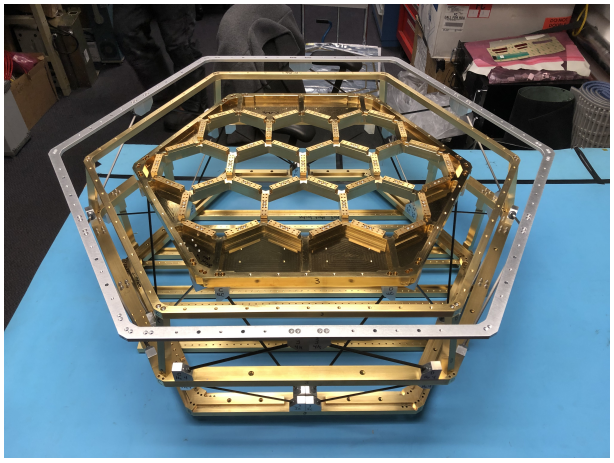

Figure 2.6: Photograph of the sub-Kelvin assembly installed in 2019. The outer aluminum ring mounts to 4 K, and a carbon-fiber truss structure stands off the 1 K, 350 mK, and 250 mK thermal stages. The hexagonal apertures in the 250 mK stage receive the detector modules. Photo courtesy of Brad Benson.

CHAPTER 3

READOUT

To operate and read out its array of detectors, SPT-3G uses the same frequency-domain multiplexed SQUID readout scheme as the previous instruments on SPT (Dobbs et al. 2012; Smecher et al. 2012), and the main components in the current processing chain have direct analogs to those used in SPTpol:

- FPGA motherboard with mezzanine daughter boards that handle the signal processing and data acquisition
- SQUID controller board generating the required biases for the SQUID amplifiers
- SQUID board on which the SQUID amplifiers are mounted, operated at 4 K
- LC board containing the inductor-capacitor filter network, operated at ∼250 mK

All of these components have been modified, upgraded, or replaced to allow for the $> 5\times$ higher multiplexing factor and $10\times$ higher detector count in SPT-3G.

3.1 Frequency-Domain Multiplexing and DfMux

For cryogenic experiments with high detector counts, the wiring required to read out each detector deposits a significant amount of heat on the cold stages, in addition to adding to instrument cost and complexity. To reduce the amount of wiring, multiple detectors can be operated using a single pair of wires in a method generically referred to as multiplexing. There are two broad categories of multiplexing common in the CMB field: time-domain multiplexing (TDM), in which each detector is only read out a fraction of the time, and frequency-domain multiplexing (FDM), in which each detector is addressed using a particular frequency channel. Within FDM, there are two further subdivisions that can roughly be classified by the range of frequencies used: MHz-based systems, usually denoted as fMux,

and GHz-based systems, more precisely referred to as microwave SQUID multiplexing or μMUX (Irwin & Lehnert 2004). The instruments on SPT have all used some form of fMux, with SPT-SZ utilizing an analog form of signal generation (AfMux) and SPTpol using a digital implementation (DfMux).

The DfMux readout system is depicted schematically in Figure 3.1. Each transition-edge sensor (TES) detector acts as a variable resistor and is placed in-series with an inductor and capacitor, forming an LCR_{TES} circuit with resonant frequency $f_0 = \frac{1}{2\pi}\frac{1}{\sqrt{LC}}$ and full-width half-power bandwidth $\Delta f = \frac{1}{2\pi}\frac{R_{\mathrm{TES}}}{L}$. By choosing different values of C while keeping L and R_{TES} uniform, each detector can be placed at its own unique resonant frequency while maintaining equal bandwidths across detectors. Several such LCR_{TES} circuits can then be connected in parallel and operated using a single pair of wires, with the number of parallel connections defining the multiplexing factor of the system. Figure 3.2 shows the admittance as a function of frequency for a 68× multiplexed circuit employed in SPT-3G, with each peak corresponding to a detector. Based on the appearance of such a plot, a multiplexed group of detectors is often referred to as a "comb" of detectors.

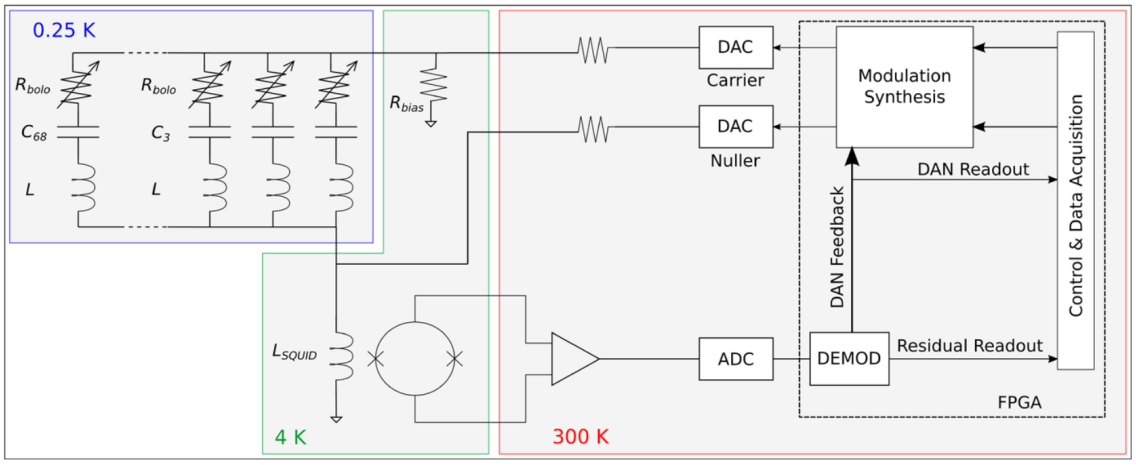

Figure 3.1: Simplified circuit of the SPT-3G DfMux readout system. Operating temperatures of the different circuit segments are indicated. Figure from Bender et al. (2019).

To operate the detectors on a comb, a corresponding comb of AC voltage biases is generated by room-temperature electronics and passed to the detectors in the cryostat. The

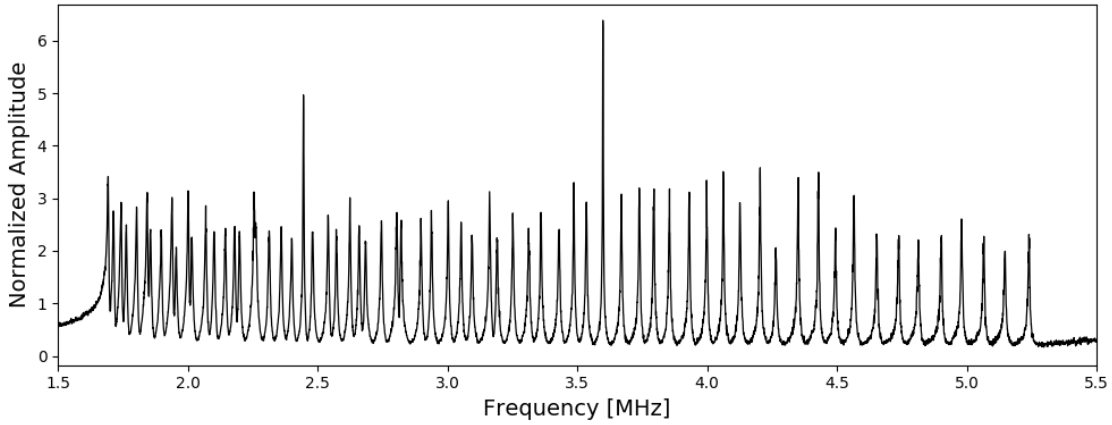

Figure 3.2: Network analysis plot showing transmitted signal vs. bias frequency for a 68× multiplexed SPT-3G detector comb. Channels with lower resistance will have taller and skinnier peaks: the two tall peaks are 1 Ω resistors, while the rest are the ∼2 Ω detectors.

constantly varying sky signal modulates the resistance of a detector, changing its resistance and amplitude-modulating the current passing through it. The comb of input biases is also referred to as the "carrier", as it carries sky information within its amplitude modulations, or equivalently within symmetric sidebands to its component frequencies in the output current. With each detector's signal occupying a unique position in frequency space, the AC currents from all detectors on a comb can be summed, passed through an amplifier, and transmitted to the data acquisition boards, where the MHz signals are demodulated (see Section 3.1.1) back to the baseband signal range of 0.01–100 Hz.

The detectors' signal is very low power—on the order of picowatts—and needs to be amplified before being passed to room-temperature electronics. As the detectors all have fairly low resistances (in our case 1–2 Ω), the choice of amplifier is restricted to having a low input impedance so as to not reflect signal. We use SQUID amplifiers (discussed more in Section 3.2), which while capable of meeting the noise and input impedance requirements, have limited dynamic range before becoming highly nonlinear. The dynamic range requirement of the SQUIDs can reduced by decreasing the amount of injected current; to first order this can be achieved by injecting a static inverted copy of the carrier comb—known as the

"nuller"—just before the input to the SQUID, leaving only the current in the sidebands that encodes the sky signal. The per-channel dynamic range requirement can be reduced yet further by utilizing digital active nulling (DAN) (de Haan et al. 2012). In the DAN scheme, a feedback circuit is used to completely null the input signal to the SQUID by adjusting the amplitude and phase of each component of the nuller in real time. The sky signal for each detector is thus encoded in the DAN readout, while the output of the SQUID serves as an error signal in the feedback circuit.

3.1.1 IQ Demodulation

An amplitude-modulated sinusoid can be written as $y_t = A_t \sin(\omega t)$, where ω is the angular frequency of the carrier wave, and A_t is the modulating signal of interest, varying on timescales $\gg \omega^{-1}$. Demodulating this signal can be done through multiplication with a sinusoid of the same frequency followed by a low-pass filter:

$$A_t \sin(\omega t)\sin(\omega t) = \frac{1}{2}A_t(1-\cos(2\omega t)) \rightarrow \frac{1}{2}A_t \ . \tag{3.1}$$

In general, complex impedances within the multiplexing circuit will induce phase delays between the injected biases voltage and the output currents. The amplitude-modulated signal then has the form $y_t = A_t \sin(\omega t + \phi)$, where ϕ is the relative phase offset. In this scenario, we can use quadrature demodulation, in which the incoming signal is multiplied by two sinusoids offset by 90°:

$$\begin{aligned} I_t &= A_t \sin(\omega t+\phi)\sin(\omega t) = \frac{1}{2}A_t[\cos\phi - \cos(2\omega t+\phi)] \rightarrow \frac{1}{2}A_t\cos\phi \\ Q_t &= A_t \sin(\omega t+\phi)\cos(\omega t) = \frac{1}{2}A_t[\sin\phi + \sin(2\omega t+\phi)] \rightarrow \frac{1}{2}A_t\sin\phi \end{aligned} \ . \tag{3.2}$$

If $\phi = 0$, all of the signal is in the in-phase component I, and none is in the quadrature phase component Q. We want the demodulated signal that is in-phase with the detector response, which to a good approximation is recovered by adjusting the phase offset ϕ to maximize I.

We obtain a more accurate phasing by recording both I and Q for each detector and using the detector's response to an injected signal to ensure all real power is in I (see Section 5.1.1 for a description of this step).

3.1.2 Readout Chain and DfMux Motherboards

The connections between components of the SPT-3G readout chain are sketched in Figure 3.3, with components explained further in the sections to follow. In brief, each DfMux motherboard has two mezzanine boards, with each mezzanine board controlling four SQUID amplifiers and synthesizing/demodulating the signals for the detectors connected to those SQUIDs. One SQUID board houses eight SQUID amplifiers and is connected to eight LC networks, which in turn are connected to the detectors.

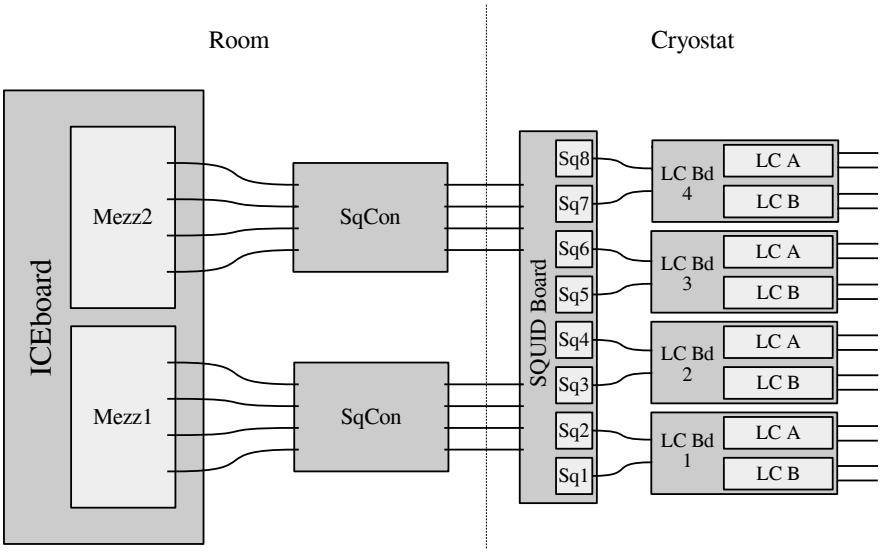

Figure 3.3: Diagram of connections within the SPT-3G readout chain. It takes three copies of the above chain to read out one detector wafer and 30 copies to read out the entire instrument. The rightmost lines are connections to the detectors (not shown).

A DfMux readout board is pictured in Figure 3.4. The ICE motherboard (Bandura et al. 2016) contains the FPGA that performs all the real-time data processing and acquisition, an ARM processor that provides a high-level network interface to the board and communication with the FPGA, and a gigabit Ethernet connection for offloading data to external computers.

Two FPGA mezzanine card connectors allow for modular connection to application-specific mezzanine boards. The fMux mezzanine boards (Bender et al. 2014) synthesize the detector biasing waveforms and contain the ADCs and DACs to transmit and receive signals from the detectors, respectively. The mezzanine boards also provide an interface for communicating with the SQUID amplifier control boards, an example of which is shown in Figure 3.4 connected to a mezzanine board via a custom readout cable. The DfMux readout boards are installed in VME crates with power and timing signals distributed by an ICE backplane, with each backplane supporting 16 boards. Two such crates are mounted directly on the SPT-3G cryostat.

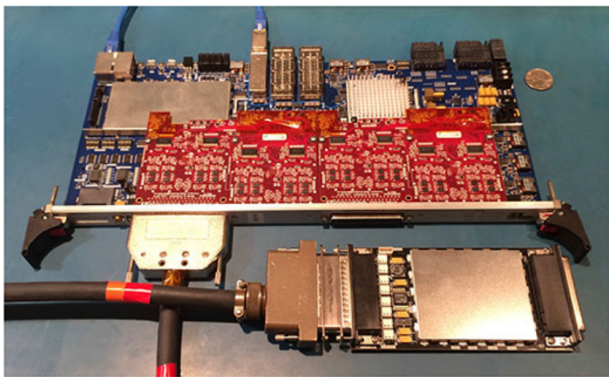

Figure 3.4: Photograph of a DfMux readout board with one mezzanine connected via a custom readout cable to a SQUID controller board. From Bender et al. (2019).

3.2 SQUID Amplifiers

A key component in fMux readout is the use of superconducting quantum interference devices (SQUIDs) as low noise, low input-impedance amplifiers. The particular type of SQUID used here is a DC SQUID (Huber et al. 2001), which consists of a superconducting loop interrupted by two parallel Josephson junctions. Current may flow through a Josephson junction without dissipating as long as it remains below the junction's critical current I_c, but above this value the junction becomes normal (resistive) and develops a voltage drop.

A circuit diagram of a DC SQUID is shown in Figure 3.5. A bias current I_b is supplied to

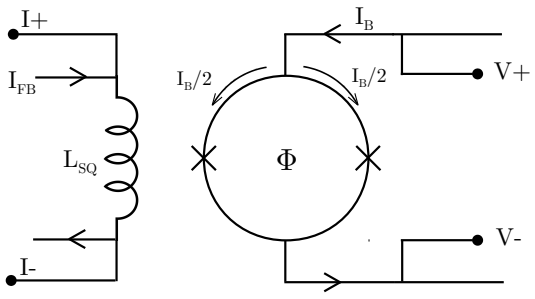

Figure 3.5: Schematic diagram of a DC SQUID amplifier. The SQUID is current-biased with I_B and flux-biased by I_{FB} running through the input coil L_{SQ}. The flux Φ through the SQUID will cause a screening current I_s (not shown) to run either clockwise or counterclockwise along the loop.

one half of the loop, sending $I_b/2$ through either arm, while an adjacent input coil inductively couples signal to the SQUID. The amount of magnetic flux Φ passing through a superconducting loop is quantized in units of $\Phi_0 = h/2e$; below $\Phi_0/2$ a circular screening current I_s will form along the loop so as to counteract the incident flux, while above $\Phi_0/2$ the current I_s reverses direction, increasing the flux to Φ_0. Once $\Phi > \Phi_0$, I_s again switches direction, and so on, creating an oscillating current with period Φ_0. In one arm of the SQUID, I_s will oppose I_b, such that the combined current through that junction is $I_b/2 - I_s$, while the current through the junction in the other arm will be $I_b/2 + I_s$. If either of these currents exceed I_c, a voltage drop will form across the SQUID that will be approximately sinusoidal in applied flux with period Φ_0:

$$V_{\mathrm{SQ}} \simeq \frac{1}{2} V_{pp} \cos(2\pi\Phi/\Phi_0) \ . \tag{3.3}$$

A measurement of this $V-\Phi$ relation for a SQUID tested for SPT-3G is shown in Figure 3.6 for different values of I_b. The shape of the curve and the the peak-to-peak voltage swing V_{pp} depend on I_b, with V_{pp} showing a local maximum before decreasing. A SQUID operated along such a $V-\Phi$ curve acts as a transimpedance amplifier, converting the current through the input coil to an output voltage with a gain defined by the slope of the $V-\Phi$ at the bias

point of the SQUID. As this gain is a measure of volts per amps, it is measured in ohms and termed the transimpedance, with symbol Z.

Some form of feedback is necessary to maintain the bias point of the SQUID and linearize its response. Previous incarnations of fMux used a shunt-feedback flux-locked-loop circuit (Dobbs et al. 2012) that relied on broadband feedback to the SQUID. This limited the available bandwidth to $\sim$1 MHz and was susceptible to a single bad channel spoiling the whole comb. With DAN feedback centered around individual frequencies, the available bandwidth is increased substantially, allowing for higher multiplexing factors. There is still a low-frequency analog feedback circuit in the DfMux electronics, intended to account for long time-scale drifts caused by changing external magnetic fields, but this has not been necessary with the NIST SA13 SQUIDs (Doriese et al. 2016) installed in SPT-3G in 2018 for unrelated performance reasons reported in Bender et al. (2018) and Silva-Feaver et al. (2018).

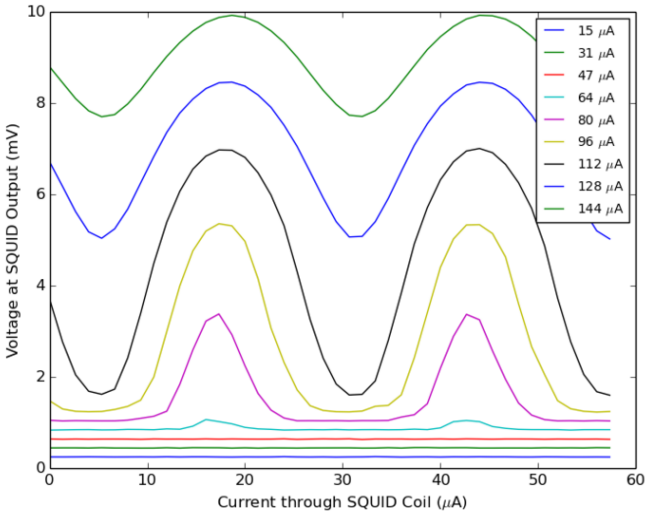

Figure 3.6: Example plot of SQUID $V-\Phi$ curves for varying levels of current bias. Data was taken using the SPT-SZ cryostat at UChicago.

The SQUIDs in SPT-3G are mounted on custom PCBs referred to as SQUID boards, with one SQUID board shown in Figure 3.7. The SQUID board design is similar to that used in SPT-SZ and SPTpol, connecting via edge connector at the 4 K shell of the cryostat

and housing eight SQUID devices magnetically shielded via a mu-metal[1] sheath. Squares of annealed niobium foil are adhered to the PCB with a thin layer of Stycast 2850FT epoxy, and the SQUIDs are affixed to the Nb foils with rubber cement and electrically connected to the circuit via wire bond. The Nb foil aids in the expulsion of any unwanted or trapped magnetic flux in the SQUIDs via the Meissner effect, in which magnetic field is expelled from a metal during its normal-to-superconducting transition. Should any flux become trapped in the SQUIDs when the cryostat is cold, a 100 Ω heater resistor positioned next to each SQUID is used to raise the board temperature above the 9.3 K transition temperature of Nb, and the board is then allowed to gently cool over a period of ∼15 minutes. This procedure is usually carried out as a precaution during a cycle of the helium refrigerator or whenever a warm readout cable is temporarily unplugged during testing. The SQUID board also contains the 30 mΩ bias resistors for establishing the bias voltages.

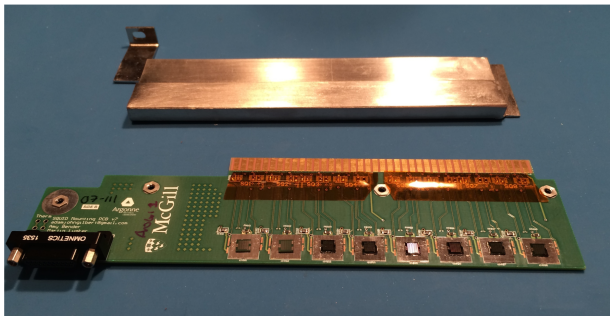

Figure 3.7: Photograph of a SQUID circuit board populated with eight SQUID devices from NIST. The board's magnetic shield (top) has been removed for the photo. From Bender et al. (2016).

The electronics handling the current biasing, flux biasing, heating, and amplification chain of the SQUIDs reside on the SQUID controller boards, located within RF boxes mounted on the outside of the cryostat. Each SQUID controller board is responsible for four of the eight SQUIDs on a SQUID board and acts as a pass-through for the detector biases on that SQUID module. SQUIDs are biased or "tuned" to their operating points at the conclusion of each fridge cycle. A full SQUID tuning consists of the following steps:

1. Amuneal A4K, https://www.amuneal.com/

1. Step through values of I_b, measuring the $V-\Phi$ curve and V_{pp} at each step. Ensure the data contain a local maximum of V_{pp}.

2. Use the dependence of V_{pp} on I_b to fit for I_b^{opt} yielding V_{pp}^{max}

3. Measure another $V-\Phi$ curve with I_b^{opt}

4. Find Φ_b corresponding to midpoint between two $V-\Phi$ extrema, where Z and dynamic range are both large.

As the optimal values of I_b and Φ_b are relatively consistent for each SQUID, we do not perform the full tuning every cycle. Instead, we apply stored values from a full tuning and compare the resulting Z to the stored Z. If the achieved Z is much lower than the stored value, a full tuning is done for that SQUID. A histogram of SQUID transimpedance values is shown in Figure 3.8, along with the fractional variation in achieved transimpedance across tunings compared to the stored value.

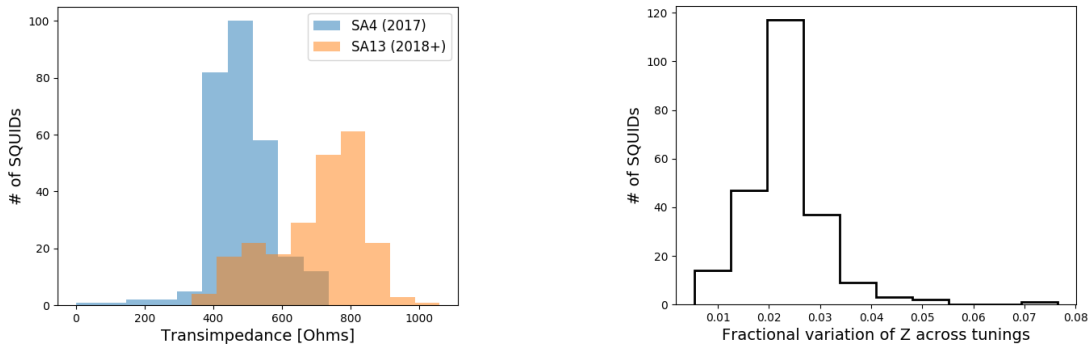

Figure 3.8: *Left:* Transimpedances for SA4 SQUIDs installed in 2017 and the SA13 SQUIDs that replaced them in 2018. *Right:* The median fractional variation of transimpedance values across tunings for SQUIDs in 2019.

3.3 LC Resonant Filters

SPT-3G employs 68× multiplexing over the bias frequency range 1.6 MHz–5.2 MHz. Each detector has approximately 5 kHz of bandwidth, set by the $\sim 2\,\Omega$ detector resistance and 60 μH

inductors. The resonant frequencies are specified by varying the values of the capacitors between approximately 16–160 pF and are logarithmically spaced across the bandwidth, with a minimum separation of 27 kHz at the low-frequency end. Lithographed spiral inductors and interdigitated capacitors are used because of their reduced scatter and low equivalent series resistance (Rotermund et al. 2016), with 68 pairs of inductors and capacitors residing on a monolithic 4.3×9.3 cm silicon chip. The inductors and capacitors are patterned using a single layer of Al, while another layer of Al on the backside of the Si chip helps to shield the inductors from external magnetic fields. The interior ends of the spiral inductors are connected via wire bond.

An LC chip is pictured in Figure 3.9 mounted on a LC PCB. Two LC chips are placed on each LC board, one on either side, with the chips held in place by a small amount of rubber cement. The differential thermal contraction between silicon and the PCB material is sufficient to crack the LC chip if it is held too rigidly, so application of adhesive must be done judiciously. After the LC chip is glued to the PCB, electrical connections are made at either end via wire bond, and an aluminum shield is installed to protect the delicate wire bonds and LC chips. The Al shield also limits inductive coupling to other chips on adjacent LC boards in the cryostat. Kapton tape on the PCB prevents the shield edges from cutting into traces on the board as a result of overzealous screw tightening. Two zero-insertion-force (ZIF) connectors on the LC board provide the connection to the detector wiring, while the connection to the SQUID board is made through broadside-coupled niobium-titanium (NbTi) stripline. Four LC boards, and thus eight LC chips, are connected to each SQUID board.

The arrangement of frequency channels on the LC chip, as well as which detector each frequency corresponds to, is carefully chosen so as to mitigate detector crosstalk. Two means by which a detector's signal can show up in that of another detector are (1) inductors coupling via their mutual inductance and (2) overlapping resonances causing the carrier bias for one detector to leak into the signal of its frequency neighbor. To address (1), adjacent channels

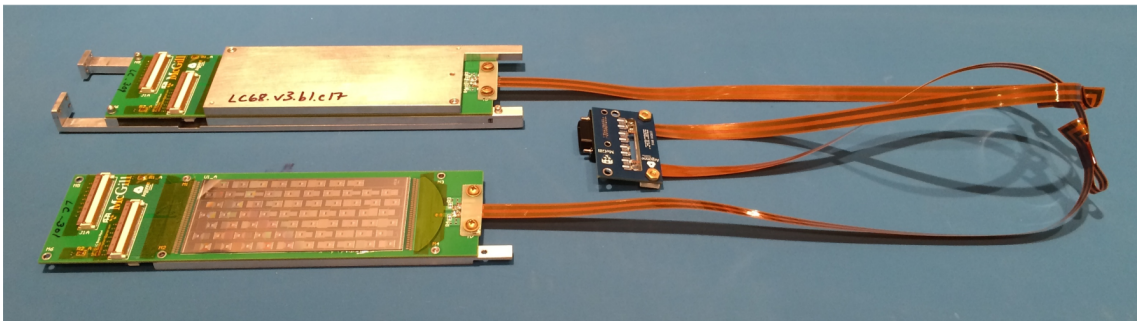

Figure 3.9: Photograph of two LC boards with the NbTi stripline and SQUID board connector. When fully assembled, four LC boards are joined together and connected to one SQUID board. The board shield has been from one LC board to reveal an LC chip. From Bender et al. (2016).

in frequency space are physically distant on the LC chip. Additional space is created between inductors by arranging the inductors and capacitors in a checkerboard pattern (though the manner in which this was done created an additional transfer function effect—see Section 3.3.2). While (2) can mostly be addressed via adequate channel spacing, some set of detectors must be chosen to be frequency neighbors, and then the question becomes what form of crosstalk is easiest to deal with.

Crosstalk between detectors of different observing frequencies is pernicious, as we use the spectral behavior of the signal to identify extragalactic point sources, disentangle foregrounds, and confirm clusters of galaxies detected via the SZ effect. Additionally, in the absence of a perfectly repeatable frequency-detector mapping, having different observing frequencies scattered throughout the comb would make it quite easy to misidentify a detector. Crosstalk between opposite polarizations within a pixel, however, results only in a degradation of polarization efficiency. Therefore, the comb is divided by detector observing band, with the 95 GHz detectors occupying the low-frequency end of the comb, the 150 GHz detectors occupying the middle, and the 220 GHz detectors occupying the high-frequency end, and polarization pairs are frequency neighbors. A plot of this frequency scheduling is shown in Figure 3.10. Two 1 Ω calibration resistors on the LC board occupy the frequency channels separating the observing bands, leaving 66 channels for actual detectors. While op-

timal for crosstalk, one disadvantage of this comb ordering is that transfer function effects, which typically worsen at higher frequencies as a result of increased reactances, disproportionately affect one band and are difficult to distinguish from effects due purely to detector fabrication parameters.

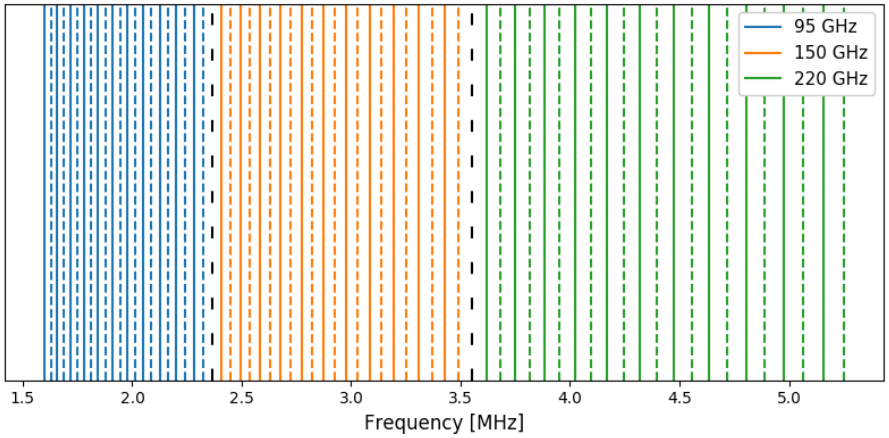

Figure 3.10: Frequency schedule within an SPT-3G comb. 95 GHz detectors *(blue)* occupy the low-frequency end of the comb, 150 GHz detectors *(orange)* are in the middle, and 220 GHz detectors *(green)* are at the high-frequency end. Within a pixel, detectors are either of "X" polarization *(dashed)* or "Y" polarization *(solid)*. The wide-dashed black line indicates the position of calibration resistors.

3.3.1 Identifying Resonances

The resonant frequencies of an LC chip are mapped out by recording the transmitted current as a function of frequency, with separate sweeps for carrier and nuller tones so that components of the circuit other than the detector comb drop out in their ratio. An example plot of such a network analysis was shown previously in Figure 3.2. Sweeping the entire 4 MHz frequency range with sufficient resolution to find optimal frequencies proved very time-consuming (∼hours), so a new method was used that first performs a coarse network analysis sufficient to identify rough peak locations, then finely samples around each peak to find the optimal frequencies. This reduced the time required for a network analysis by a factor of several.

We know what detector is connected to which LC channel based on the wiring, and we know the design frequency of each LC channel; however, the *actual* frequency of each LC channel is prone to some degree of scatter. In addition, different versions of LC chip were made, with chips of each version fabricated across several batches. Small variations in fab resulted in different batches having shifted frequencies and different degrees of frequency scatter. Furthermore, poor wire bonds to the detectors or LC chip can appear as open connections when probed at DC but be capacitively coupled at MHz frequencies, such that a channel resonance expected to be missing can show up in the comb at some higher frequency. These issues make matching a given resonance to a particular detector a nontrivial task.

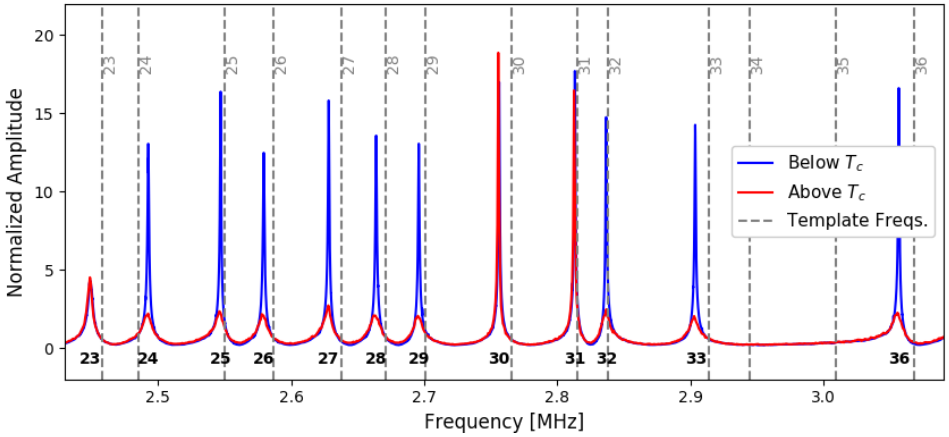

Figure 3.11: Network analyses taken with the detector stage above T_c *(red)* and below T_c *(blue)*, along with template channel frequencies from LC testing *(gray, dashed)*. Resonances are labeled with their identified channel number in bold.

Prior to their installation in the SPT-3G receiver, LC chips were tested in laboratory cryostats in order to map their resonant frequencies. The LC boards were connected to resistor boards populated with 0, 1, and 2 Ω resistors, with the resistances alternating with frequency channel to make identifying resonances easier. We were unable to test all chips individually, so we relied on testing a few chips from each fabrication batch in order to create a template of average resonance locations. When analyzing subsequent network analyses, either a chip's previous results or these batch-average templates would then be used to

automatically identify resonances with the closest matching frequency channel. When the full instrument was installed in the telescope, I visually inspected the network analyses from all 240 combs to check the data quality, verify and correct the channel matching results, and identify any resonances that should not be used. I cross-referenced these results with connectivity tests performed on each wafer before installation into the cryostat. Figure 3.11 is an example of the plots I generated to do this, showing a subset of one comb and displaying the level of agreement between template and actual frequencies, channels with opens (Ch34 and Ch35), channels with shorts (Ch30 and Ch31), and the calibration resistor (Ch23).

I performed a final verification of the resonance identification by utilizing telescope calibration observations. Each detector's sky pointing is calculated through observations of a Galactic HII region that serves as a compact source of mm-wave flux (see Section 5.1.1). This pointing information can be used to map detectors' positions within the focal plane, and misidentified detectors will show up at the wrong location. Of the ∼15,000 mapped resonances, only $\mathcal{O}$(10s) were found to be incorrect, though this same method also helped catch errors in the bookkeeping of readout connections. It should be noted that pointing information alone does not distinguish between the polarization pair of detectors in a pixel, so there likely exist $\mathcal{O}$(10s) of detectors labeled with the wrong polarization angle. This has a larger effect than being mismapped to a different pixel, as detector pointing is calibrated off the sky, but (as of the time of writing) the polarization angles are based solely on detector identity. SPT-3G now has per-detector measured polarization angles sufficient to check for these errors, but this has yet to be done.

3.3.2 Transfer Function Effect of L-C Ordering

To increase spacing between neighboring inductors on the LC chip, the capacitors and inductors are arranged in a checkerboard pattern. For the chips in SPT-3G, this was done by switching the *L-C* ordering in the circuit, such that alternating rows on the LC chip are ordered either LCR or CLR. During detector testing, I observed bimodal distributions

in detector normal resistances, most pronounced in the 220 GHz detectors, that perfectly tracked the *L*-*C* ordering of the respective channels.

The planar spiral inductors and interdigitated capacitors are distributed elements with footprints of approximately $15\,\mathrm{mm}^2$ and are separated by 1 mm of Si from the Al backing layer of the LC chip. They therefore have some capacitive coupling to the Al layer, and if we model them as parallel-plate capacitors and use the relative permittivity of Si $\epsilon_r = 11.68$, this yields a parasitic capacitance of

$$C_{\mathrm{par}} = \frac{\epsilon A}{D} = \frac{11.68\epsilon_0(15\,\mathrm{mm}^2)}{1\,\mathrm{mm}} \approx 1.5\,\mathrm{pF}\ . \tag{3.4}$$

I created a simulation of an LC chip in LTspice[2] circuit software incorporating these parasitic capacitances, as well as a small capacitance between the Al LC backing layer and the LC board ground plane, and then measured the impedance seen by each channel. Figure 3.12 shows the results from simulation compared to actual data: while there are clearly other effects present in the real data, the simulation shows the bimodality of resistance values can be explained by parasitics affected by the *L*-*C* ordering. To avoid this complication for similar LC chips made in the future, the ordering of the circuit elements should be kept consistent and rows simply offset from one another. Alternatively, the parasitics could be reduced by removing the Al backing layer of the LC chip. The data in Figure 3.12 can be used to construct an empirical correction function to measured detector resistances, as in Dutcher et al. (2018), but a complete characterization of other transfer function effects, while outside the scope of the work shown here, is crucial for accurately measuring detector properties with the DfMux system.

2. https://www.analog.com/

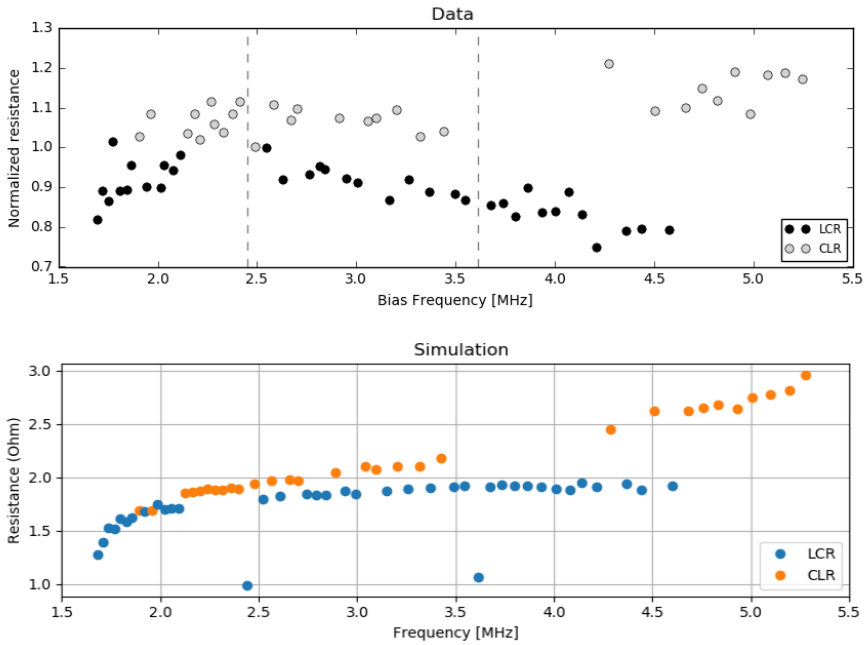

Figure 3.12: Effect of parasitic capacitances and L-C ordering on measurements of resistance. The top plot is data collected from SPT-3G in early 2018, while the bottom plot is the result of a (somewhat simplified) circuit simulation.

3.4 Cold Wiring

NbTi Striplines

The connection between the LC boards at ∼250 mK and the SQUID boards at 4 K must be made with low thermal conductance, low reactance wiring. The resistor establishing the bias voltages is located on the SQUID board, and any voltage drop across reactances between this resistor and the detectors will partially spoil the voltage bias required for stable TES operation (see Chapter 4). In addition, the stray inductance in this portion of the circuit can lead to crosstalk between detectors, as described in Dobbs et al. (2012). For this important connection, we use broadside-coupled NbTi stripline, pictured above in Figure 3.9. The construction and properties of the stripline are described in detail in Avva et al. (2018), which I briefly summarize here.

The conducting material of the stripline is a pair of 2 mm-wide, 10 μm-thick NbTi traces separate by a 30 μm polyimide core. Each 8 mm-wide stripline contains two such pairs, such

that one stripline connects to one LC board, with each pair of conductors reading out one side. Four striplines connect a set of four LC boards to one connectorized adapter board that is then plugged in to one SQUID board. Ultrasonic soldering is used to initially tin the ends of the NbTi stripline, after which they are connected with conventional soldering and clamped to boards. Two lengths of stripline are used in the SPT-3G cryostat, 60 cm and 75 cm, in order to reach all areas of the focal plane while allowing intermediate heat sinking to the 1 K and 350 mK temperature stages. The inductance of the 60 cm striplines was measured to be 21 nH, with an additional 25 nH arising from the connectors and SQUID board wiring, leading to a median 0.09% crosstalk between detectors.

Flex Cables

To make the connections between the detector wafer and and LC boards, I designed a custom flexible printed circuit, or "flex cable", as shown in Figure 3.13. The wiring traces for the detectors are routed to each edge of the hexagonal detector wafers, and connection to the flex cable is made via wire bond. The flex cable then plugs in to the LC boards via zero-insertion force (ZIF) connections, with six flex cables required for each detector wafer.

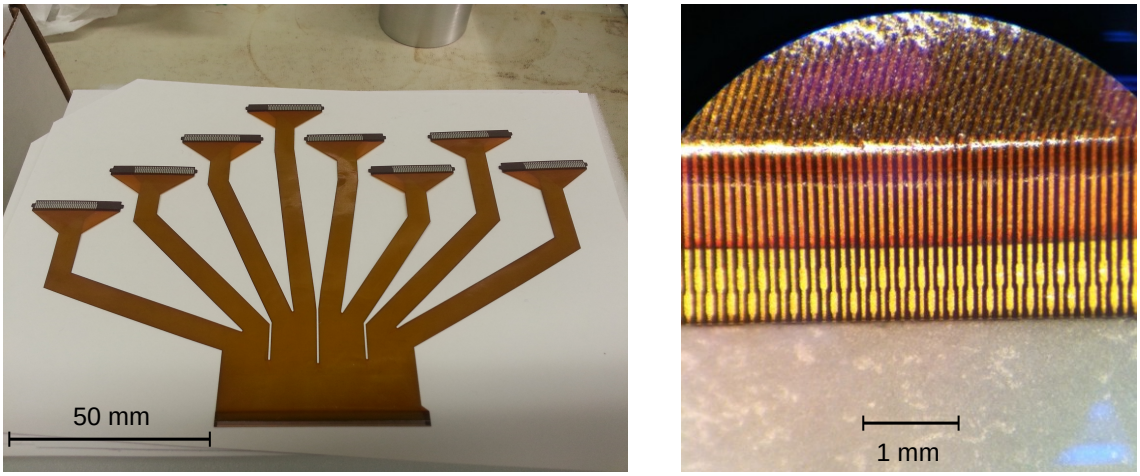

Figure 3.13: *Left:* Photograph of a wafer-to-LC flex cable. Six such cables connect to each detector wafer. *Right:* Close-up of the wire bond end of the cable, showing the gold-plated bond pads for connections to the detector wafer.

The base material of the flex cables is polyimide, and the electrical traces are 9 micron-thick copper plated in tin (T_c=3.72 K) to reduce resistivity. The stray resistance of the entire readout chain exclusive of the detectors is $\sim$0.2 Ω, a negligible fraction of which comes from the flex cable. Unlike the striplines discussed above, stray reactances in the flex cable are not a major concern, as they are within the LCR_{TES} circuit for each detector and thus are tuned out. At the wire bond end of the cable, the traces transition to bare copper to permit wire bonding. When exposed to air, copper forms an oxide layer that must be removed before wire bonding: for small numbers of devices this is a minor inconvenience and can be done manually with the use of a simple rubber eraser, but for the small feature sizes and large number of cables used throughout SPT-3G, this step proved too troublesome. Therefore 50 microinches (1.3 μm) of soft gold is added to the flex cable bond pads to ease wire bonding. The bond pads on the wafer and flex cable are staggered to create a double row of bonds with an effective pitch of 100 μm.

On the opposite end of the flex cable, the cable splits into eight legs each reading out 33 detectors. The relative lengths of each of the legs are designed to facilitate unambiguous connection to the LC boards as they are assembled into a detector module. Ninety-pin ZIF connectors are used on the LC boards, as they are compatible with readout materials from both SPTpol and POLARBEAR-2, requiring two connectors to read out 66 detectors. Each SPT-3G detector wafer contains 1614 detectors, which inconveniently is not divisible by 66; this wiring limits the total possible number of detectors read out per-wafer to 1584, or 98% of fabricated devices.

CHAPTER 4

DEVELOPING DETECTORS FOR SPT-3G

The light-detecting elements utilized in SPT-3G are transition-edge sensor (TES) bolometers. TES bolometers are a popular choice for ground-based CMB observations as they are, in principle, background-limited: the dominant source of optical power on the detectors is the atmosphere, and the largest contribution to measurement noise arises from the random arrival times of those photons. Actually achieving photon-noise-dominated performance requires careful tuning of the detector properties and reliably hitting the target values in fabrication. I spent much of my graduate career developing and testing the detectors for SPT-3G, and in this chapter I give an overview of that effort. First I go over the basics of TES bolometers and their key properties, and I explain the impact of these properties on detector sensitivity. As TES bolometers are a mature technology, these topics are already well-covered in the existing literature. I then discuss the implementation of TES bolometers within SPT-3G, including target parameter values, pixel architecture, and optical coupling, and I report on the results of detector testing both in the lab and as deployed on the telescope. I conclude by detailing the detector fabrication process and the assembly of the detector modules.

4.1 Overview of TES Bolometers

A bolometer (Langley 1880) is a device that detects electromagnetic radiation by absorbing radiant energy and converting it to heat, then using the thermal dependence of an electrical resistor to measure the deposited power. Conceptually then a bolometer consists of an absorber attached to a resistance thermometer, though structurally one material may serve both functions. After its effect is measured, the excess heat is allowed to dissipate via a weak thermal link to a cold thermal reservoir, returning the bolometer to its equilibrium state. In a TES bolometer, the resistance thermometer is a metal held in its superconducting

transition, such that a small change in temperature results in a comparatively large change in resistance (see Figure 4.1). The resulting gain in sensitivity is typically quantified through the logarithmic derivative of the R-T relation, $\alpha \equiv \frac{d\ln R}{d\ln T} = \frac{T}{R}\frac{dR}{dT}$, which for our devices is $\mathcal{O}(100)$.

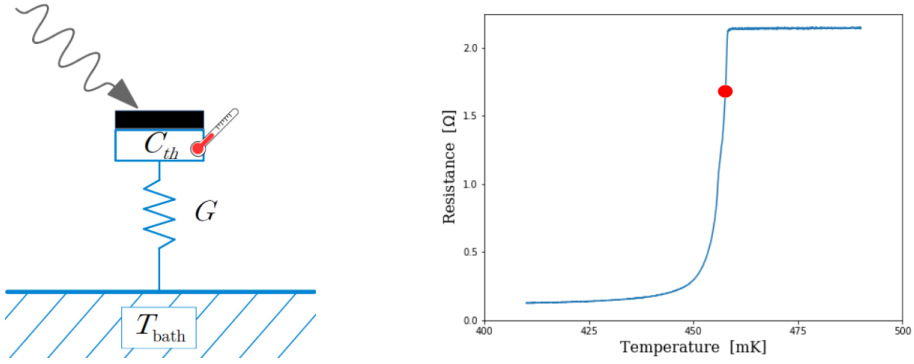

Figure 4.1: *Left:* Cartoon depiction of a bolometer. Incoming light hits an absorber, heating up a thermometer with heat capacity C. The thermometer is connected to a cold bath through a weak thermal link G. *Right:* Plot of resistance vs. temperature showing the superconducting transition of a TES. When operated at the point indicated by the red dot, the TES serves as a very sensitive thermometer.

Operating a TES within its narrow transition region requires very fine temperature control. In the first TES bolometer (Andrews et al. 1942), a stage heater was set to just below the critical transition temperature T_{c}, while the remaining power was supplied by Joule heating from the fixed sense current used to measure the TES resistance. For large arrays of TESs, this approach is infeasible as a result of device-level variation of T_{c} and susceptibility of current biases to thermal runaway: the Joule heating of a current-biased TES is given by $P_{\text{el}} = I_{\text{bias}}^2 R_{\text{TES}}$, therefore increased TES resistance leads to greater heat production which further increases the TES resistance, and so on. A more scalable approach is to hold the thermal stage well below T_{c} while supplying a tunable voltage bias to each detector to place them in their transitions. The voltage bias will tend to self-regulate, as it produces heating power given by $P_{el} = V_{\text{bias}}^2/R_{\text{TES}}$, which decreases with increased TES temperature and vice-versa. As in other applications of negative feedback, this process of electrothermal feedback (ETF) increases the dynamic range of a detector and linearizes its response. The

theoretical underpinnings of TESs operating under strong ETF have been thoroughly documented elsewhere (Irwin et al. 1998; Irwin & Hilton 2005); I summarize some of the salient points below and in Table 4.1.

$\alpha \equiv \frac{T}{R}\frac{dR}{dT}$	Sensitivity of superconducting transition
$P_{\rm bath}(T) = K(T^n - T_{\rm bath}^n)$	Power flow from bolometer to bath
$G \equiv \frac{dP}{dT} = nKT_{\rm c}^{n-1}$	Thermal conductance of bolometer link
$\mathcal{L} \equiv \frac{P_{el}\alpha}{GT_{\rm c}}$	ETF loopgain
$\tau_{\rm th,0} = C_{\rm th}/G$	Natural thermal time constant
$\tau_{\rm th} = \frac{\tau_{\rm th,0}}{\mathcal{L}+1}$	Thermal time constant under ETF
$\tau_{\rm elec} \lesssim \tau_{\rm th}/5.8$	Stability criterion

Table 4.1: Important formulas and definitions relating to TES properties and operation. Adapted from Irwin & Hilton (2005).

A bolometer can be thermally modeled as a heat capacity $C_{\rm th}$ connected to a thermal bath via a weak link with dynamic thermal conductance $G \equiv \frac{dP}{dT}$. Excess heat in the bolometer will be dissipated with a thermal time constant $\tau_{\rm th,0} = C_{\rm th}/G$, and equilibrium is reached when the electrical power $P_{\rm el}$ and optical power $P_{\rm opt}$ balance the outward heat flow:

$$C_{\rm th}\frac{dT}{dt} = P_{\rm el} + P_{\rm opt} - P_{\rm bath}. \tag{4.1}$$

For the power flowing from the TES at temperature T to the cold bath, we assume a power-law dependence

$$P_{\rm bath}(T) = K(T^n - T_{\rm bath}^n) \tag{4.2}$$

where K is a constant related to the geometry and material properties of the thermal connection, and the exponent n sets the scaling of G with T: for electron-dominated thermal transport $n \sim 2$, and for phonon-dominated transport $n \sim$3–4. The thermal conductance is then given by

$$G = nKT_{\rm c}^{n-1}, \tag{4.3}$$

where I have plugged in $T = T_c$ for a TES being held in its transition.

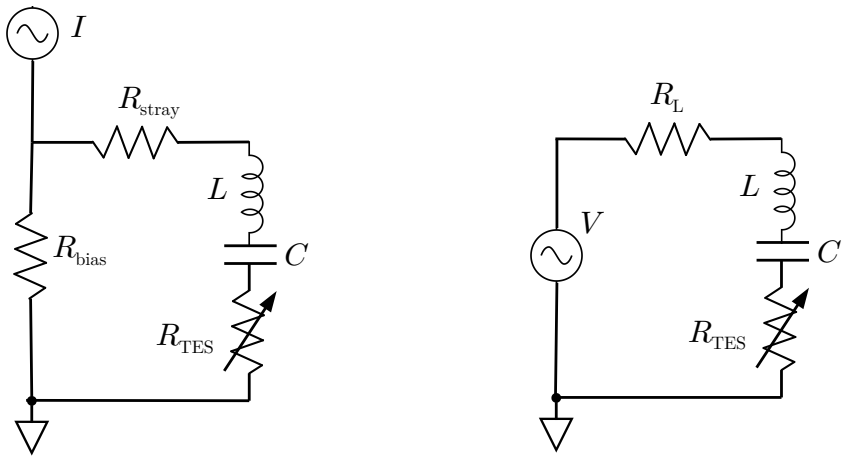

Figure 4.2: TES bias circuit diagrams. *Left:* The single-detector version of the bias circuit. A small bias resistor ($R_{\rm bias} \ll R_{\rm TES}$) is placed parallel to the bolometer $LCR_{\rm TES}$ circuit, which in general will have some additional small stray resistance, and the circuit is supplied with a fixed current. *Right:* The Thevenin-equivalent of the circuit on the left, where the current source is replaced by a voltage source and series resistance $R_L = R_{\rm bias} + R_{\rm stray}$.

The electrical model for the bolometer bias circuit is shown in Figure 4.2. Using Kirchoff's voltage law, the current flowing through the TES can be written as

$$L\frac{dI}{dt} + \frac{1}{C}\int I dt' = V - IR_L - IR_{\rm TES}. \tag{4.4}$$

Equations 4.1 and 4.4 form a pair of coupled electrothermal equations that govern the TES behavior. The general solution of these equations for time-varying signals is given in Irwin & Hilton (2005); here I quote the results that under ETF the bolometer response time is increased to

$$\tau_{\rm th} = \frac{\tau_{\rm th,0}}{\mathcal{L}+1}\ , \tag{4.5}$$

where the ETF loopgain $\mathcal{L}$ is defined as $\mathcal{L} \equiv \frac{P_{el}\alpha}{GT_c}$, and that stable ETF requires the electrical time constant of the bias circuit $\tau_{\rm elec}$ be faster than the thermal response time of

the bolometer, with the precise requirement given by

$$\tau_{\rm elec} \lesssim \tau_{\rm th}/5.8\,. \tag{4.6}$$

The LCR circuit containing the TES has $\tau_{\rm elec} = 2L/R$, which for the device values in SPT-3G restricts $\tau_{\rm th} \gtrsim 0.35$ ms.

While large thermal time constants are desirable for TES stability, short time constants are beneficial on a scanning instrument such as SPT, as detector resolving time is effectively convolved with the instrument beam, and thus has a direct effect on angular resolution. As will be discussed further in Chapter 5, SPT-3G scans at angular speeds between 0.34–0.74 deg/s as measured on the sky, placing signals of cosmological interest generally in the range of 0.02–23 Hz. A detector with $\tau = 7$ ms has an $f_{\rm 3dB}$ (the frequency at which signal response is halved) of 23 Hz. To maintain stability without degrading the telescope response, the detector time constants should fall within the range of 0.35–7 ms. Other properties of the detectors are chosen based on their effects on instrument noise performance, discussed below.

4.1.1 Noise Properties

A common measure of a detector's sensitivity is its noise-equivalent power (NEP), defined as the amount of absorbed power that would be detected with signal-to-noise equal to one over a 1 Hz bandwidth. Uncorrelated sources of noise add in-quadrature to form the total detector NEP: $\mathrm{NEP}^2_{\rm tot} = \mathrm{NEP}^2_{\rm photon} + \mathrm{NEP}^2_{\rm phonon} + \mathrm{NEP}^2_{\rm Johnson} + \mathrm{NEP}^2_{\rm readout} + \ldots$. A detector is background-limited when the photon noise term is the largest contribution to the total NEP. As was the case for their principles of operation, the noise properties of TES bolometer systems are already well-documented, with thorough dicussions in, e.g., Irwin & Hilton (2005) and Richards (1994). I summarize the sources of detector noise in Table 4.2 and briefly explain them below.

Noise Source	NEP Formula
TES Johnson noise	$\sqrt{4k_B T_c P_{el}}/\mathcal{L}$
Phonon noise ($\gamma = 0.5$)	$\sqrt{\gamma 4k_B G T_c^2}$
Photon shot noise	$\sqrt{2h\nu P_{opt}}$
Photon correlated noise ($\xi = 1$)	$\sqrt{2\xi P_{opt}^2/\Delta\nu}$

Table 4.2: Formulas for noise-equivalent power (NEP) contributions arising from detector and instrument properties.

Johnson Noise

Thermal agitation of charge carriers leads to electrical noise within a circuit, with the rms voltage fluctuations per-unit bandwidth given by $dV^2 = 4k_B T R$ for a resistance R at temperature T. The resulting Johnson noise voltage can be referred to an input power using the responsivity of the detector, which for TES operating under ETF leads to

$$\mathrm{NEP}^2_{\mathrm{Johnson}} = 4k_B T_c P_{el}/\mathcal{L}^2 \ , \tag{4.7}$$

where $P_{el} = I^2 R_{TES}$ is the electrical bias power supplied to the TES. On plugging in Eq. 4.3 and the expressions for $\mathcal{L}$ and α, this noise term is seen to be proportional to RT_c^{2n-1}. Reducing the resistance of the TES therefore moderately improves performance, as is typical of Johnson noise, but a far greater reduction is achieved by lowering the operating temperature of the TES. The base temperature of the helium sorption refrigerator used in SPT-3G sets a hard lower limit of $T_c > 250\,\mathrm{mK}$.

Phonon Noise

The passage of quantized thermal carriers over the thermal link connecting the bolometer to the bath will cause fluctuations in the temperature of the TES, introducing noise. This source of noise is alternately referred to as thermal fluctuation noise, G noise, or phonon

noise (though electrons may also be a thermal carrier). This noise term is given by

$$\mathrm{NEP}^2_{\mathrm{phonon}} = \gamma 4 k_B G T_c^2 \,, \tag{4.8}$$

where γ is a unitless parameter typically between 0.5–1 (Irwin & Hilton 2005). Phonon noise is reduced by decreasing the thermal conductance of the bolometer link, as well as the T_c of the TES, though the value of G must also be chosen so as to equilibriate the right hand side of Equation 4.1.

Photon Noise

As photons are discrete carriers of energy, there will be fluctuations in received signal associated with their random arrival times. The variance in number of photons per mode for an equilibrium blackbody is given by $< \Delta n^2 >= n + n^2$ (Kittel & Kroemer 1980), and the associated fluctuation in energy is $h\nu < \Delta n^2 >$. If integrated over a bandwidth $\Delta\nu$ centered at ν_0 over which the spectrum does not vary appreciably, this becomes

$$\mathrm{NEP}^2_{\mathrm{photon}} = 2h\nu_0 P_{\mathrm{opt}} + 2\xi P^2_{\mathrm{opt}}/\Delta\nu \,, \tag{4.9}$$

where P_{opt} is the total received optical power over the bandwidth. The first term describes the Poisson-distributed random arrival times of the photons and is referred to as the Poisson or shot noise, while the second term describes the correlated arrival of photons in bunches, and is known as the "bunching" or Bose term (Richards 1994). The dimensionless parameter ξ depends on the coherence of the light and is usually taken to be between 0–1. The photon noise can only be reduced by decreasing the incident optical power, which depends on the effective temperature of the atmosphere within the detector bandpasses, as well as on the temperature, transmission, and emissivity of all the elements in the optical path. For SPT-3G, the optical loading for the (95, 150, 220) GHz detectors was predicted to be (5.3, 8.0, 10.5) pW. The saturation powers (P_{sat}) of the detectors were chosen to be twice this value,

evenly distributing the total incident power on the bolometer between electrical and optical power and also leaving a (small) margin in case the optical loading exceeded predictions.

Readout Noise

The last significant noise contribution is not inherent to the detector, but instead is produced by a combination of sources in the readout system, including the amplifiers in the warm electronics, the SQUID amplifiers, and Johnson noise in the bias resistor (see Dobbs et al. (2012)). As reported in Bender et al. (2019), the readout noise is measured to be $\sim 13\,\mathrm{pA}/\sqrt{\mathrm{Hz}}$, which is the noise-equivalent current (NEI) through the SQUID input coil. To convert this to an NEP at the detector, one multiplies by the applied voltage bias, which for a fixed P_{el} increases for larger R_{TES}. The resistance of the detectors should therefore be kept small, although stable voltage-biasing of the TES requires that $R_{\mathrm{TES}} \gg R_{\mathrm{stray}}$. With measured $R_{\mathrm{stray}} \approx 0.3\,\Omega$, we have targeted the normal resistance of the TES to be $R_{\mathrm{n}} \sim 2.0\,\Omega$.

4.2 SPT-3G Pixel Design

SPT-3G utilizes a pixel architecture originally developed for the POLARBEAR-2 instrument and shared with the upcoming Simons Observatory and LiteBIRD experiments (Suzuki et al. 2012, 2018; Galitzki et al. 2018). At the center of each pixel (Figure 4.3, left), a dual-polarized sinuous antenna couples incoming radiation to a superconducting microstrip. The broadband signal from the antenna is then transmitted through in-line band-defining filters before being measured by the TES bolometers. Each pixel in SPT-3G has six bolometers, one for each polarization in three frequency bands. Arrays containing 269 pixels are fabricated on monolithic 150 mm-diameter silicon wafers (Figure 4.3, right), with ten such wafers being installed in SPT-3G for a total of just over 16,000 detectors in the focal plane.

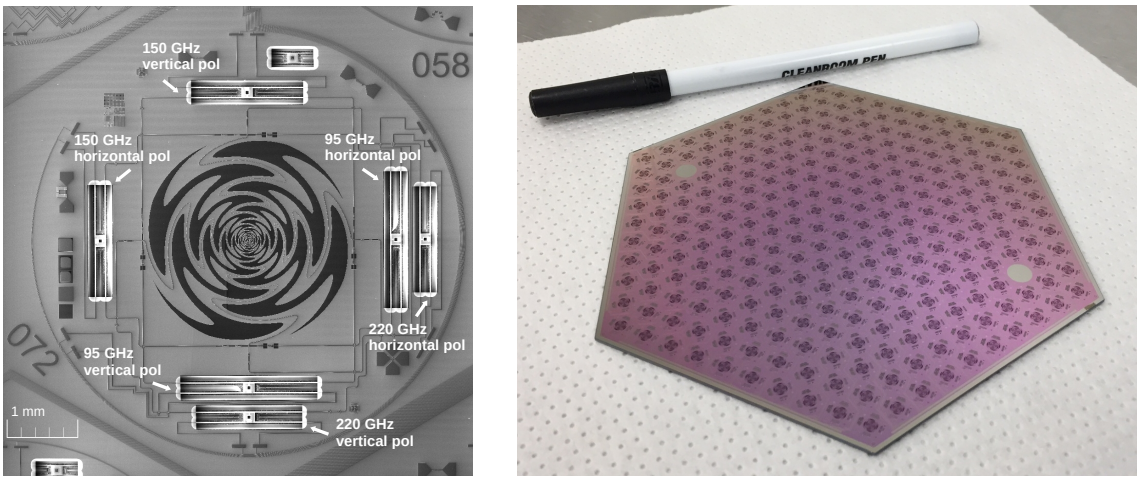

Figure 4.3: *Left:* Photograph of an SPT-3G pixel (Ding et al. 2017). The frequency and polarization of each bolometer have been labeled. *Right:* Photograph of a detector wafer containing 269 pixels. Photo courtesy of Amy Bender.

4.2.1 Optical Coupling

Lenslets

Incoming radiation is quasi-optically coupled to the pixel antennas through 5 mm-diameter alumina hemispheres referred to as lenslets. The lenslets are mounted on a separate 900 μm-thick silicon wafer, where they are set into etched 100 μm recesses. The detector and lenslet wafers contact each other on their bare surfaces such that the antennas are back-illuminated through the bulk silicon of each wafer . The lenslets have a three-layer anti-reflection coating similar to that used on the large optical elements (Nadolski et al. 2020). The layers of the AR coating are clamped and thermally bonded into one sheet, which is then molded to fit the lenslet array and secured with Stycast epoxy. A cross-section of an AR-coated lenslet and a fully populated lenslet array are shown in Figure 4.4.

Sinuous Antenna

The sinuous antenna is a type of log-periodic antenna invented by DuHamel (1987) and studied for application to CMB science by O'Brient (2010). It has several advantageous

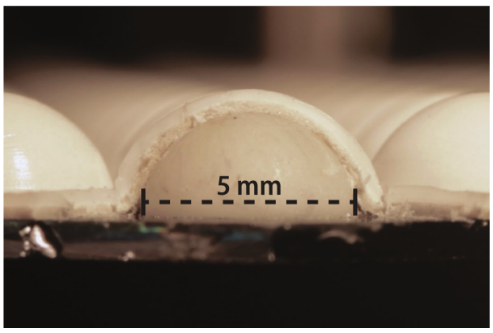

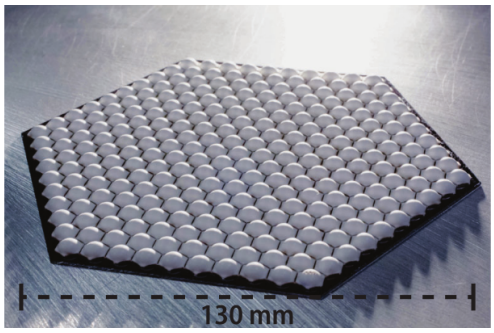

Figure 4.4: *Left:* Cross-sectional photograph of an AR-coated lenslet. *Right:* Photograph of a 271-element lenslet array. Images from Nadolski et al. (2020).

properties, including broadband response, dual linear polarization, and a planar geometry allowing for simplified lithographic fabrication. The antenna consists of radial lobes comprised of a series of self-similar cells, with the edges of each lobe defined by the two curves

$$\phi(r) = (-1)^p \alpha \sin \frac{\pi \ln(r/R_p)}{\ln \tau} \pm \delta \tag{4.10}$$

for $R_p < r < \tau R_p$, where p is an integer labeling each cell of the antenna, R_p is the inner radius of cell p, and τ is a logarithmic scaling factor. Each edge of an antenna lobe traces out angle 2α, while the whole lobe subtends angle $2\alpha + 2\delta$. The bulk of the structure in each antenna lobe is perpendicular to the radial direction, resulting in polarization sensitivity orthogonal to that of a bow tie antenna occupying a similar footprint. The most popular subclass of sinuous antenna, including that used in CMB experiments such as SPT-3G, have $\alpha = 45°$ and $\delta = 22.5°$, creating a self-complementary four-lobed antenna with frequency-independent input impedance and dual linear polarization.

The frequency coverage of the antenna is limited only by its innermost and outermost radii. Radiation of wavelength λ couples to the antenna in an annular region of radius

$$R_{rad} = \frac{\lambda}{4(\alpha + \delta)}. \tag{4.11}$$

The antennas for SPT-3G have inner radius $R_0 = 13\,\mu$m and 17 cells, with an outermost

radius of 1.4 mm. These dimensions are predominantly set by the limits of fabrication tolerances and the restrictions on pixel size, and are sufficient to provide a flat passband over the range of frequencies measured by SPT-3G with additional buffer between the active antenna regions and the inner and outer antenna edges.

A well-known property of the sinuous antenna is the periodic variation of polarization angle with frequency, or "polarization wobble," caused by the oscillating antenna structure. A lower value of the antenna scaling factor τ decreases the polarization wobble by narrowing the structure in each lobe and packing more cells per unit radius (Suzuki 2013); however, it also complicates fabrication, as the antenna feed lines must snake atop the antenna arms in order to couple to the high-frequency region at the center. A value of τ=1.3 was chosen to meet the microstrip fabrication requirements while having adequate performance: HFSS simulations of this design show polarization wobble with an amplitude of $\pm 5^\circ$ (Edwards et al. 2012). To reduce the bias in polarized maps caused by this wobble, each detector wafer contains a roughly equal number of mirror-image antennas, such that the left-handed wobble and right-handed wobble cancel out on average. In addition, half of the antennas on each wafer are rotated by 45° to evenly sample Stokes Q and U on the sky. Figure 4.5 indicates the orientations of the pixel antennas on each wafer, as well as which pixels are blank or not connected to readout. Wafers are installed into the instrument focal plane with random 60° rotations to increase the number of possible polarization angles.

Triplexer

The broadband signal from the sinuous antenna is divided into three observing bands by an in-line triplexer circuit (O'Brient et al. 2013), pictured in Figure 4.6. The triplexer consists of quasi-lumped element filters, in which sections of microstrip have been removed or formed into high-impedance coplanar waveguide to serve as capacitors and inductors, respectively. To model the detector bandpasses and their dependence on the material and geometrical

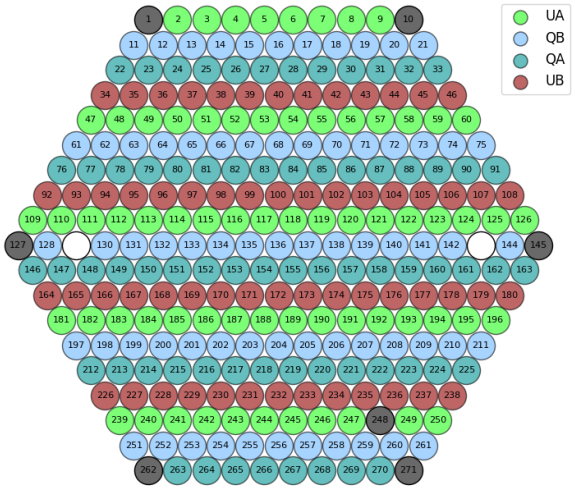

Figure 4.5: Diagram of the antenna type for each pixel on a detector wafer. Q/U refers to the angle of the antenna, while A/B refers to its handedness. Two pixel footprints remain empty and are used for alignment marks required during fabrication, while the seven gray pixels are not connected to the readout wiring.

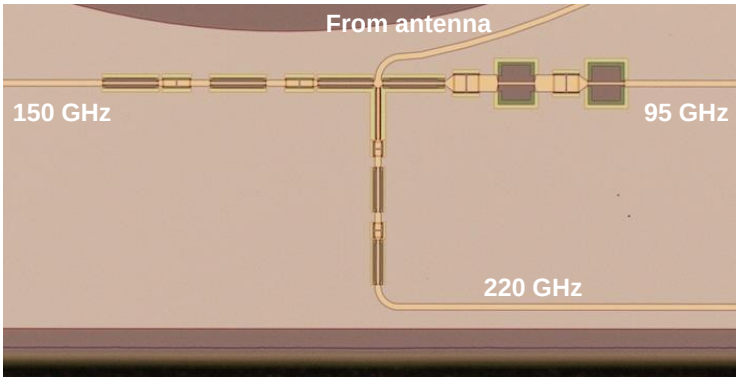

Figure 4.6: Image of the triplexer circuit that divides the antenna signal into three frequency bands. The dark regions are where the wafer ground plane has been removed. Photo courtesy of Adam Anderson.

properties of features on the wafer, the triplexer filter is simulated using Sonnet software[1]. Figure 4.7 shows the simulated triplexer bandpasses for the nominal 500 nm SiO_x dielectric layer, as well as the shifts in bandpasses resulting from different layer thicknesses. After passing through the triplexer, the microstrip transmission line carrying each polarization and frequency band then terminates in an impedance-matched 20 Ω resistor on the respective bolometer island.

1. https://www.sonnetsoftware.com/

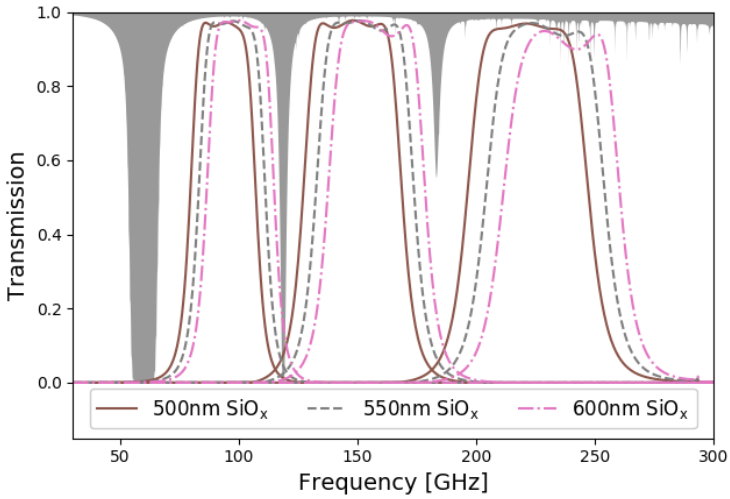

Figure 4.7: Simulated triplexer bandpasses for varying SiO_x dielectric layer thickness, nominally 500 nm. Overplotted is a model of atmospheric transmission for 0.25 mm PWV.

4.2.2 Bolometers

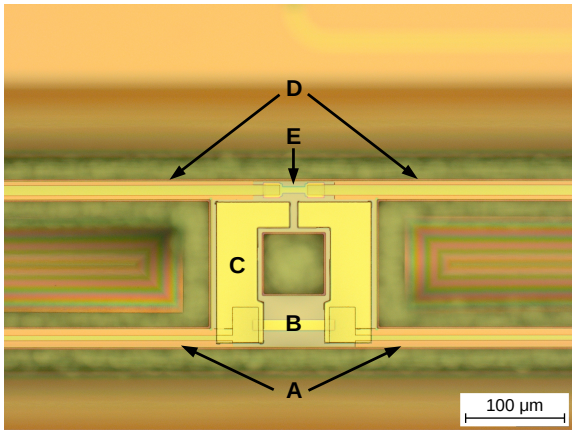

Figure 4.8: Photograph of a bolometer island showing (A) TES bias lines, (B) TES, (C) Pd heat capacity, (D) antenna feed lines, and (E) 20 Ω antenna load resistor. (A) and (D) run along SiN_x legs that support the bolometer island and provide the thermal connection to the bulk of the wafer. Photo from Anderson et al. (2019).

The bolometers in SPT-3G are released structures, having the underlying silicon removed via chemical etch and consisting of a central island suspended by four silicon nitride legs, which provide the mechanical and thermal connection to the bulk of the wafer (see Figure 4.8). $P_{\rm sat}$ is tuned for bolometers according to observing band by varying the lengths of

these legs between approximately 450–900 μm, with longer legs decreasing G and lowering $P_{\rm sat}$. The bolometer island contains the antenna load resistor that thermalizes the sky signal and the TES that measures the change in temperature, with the antenna leads and TES bias lines carried on the SiN_x legs. The TES itself is a thin (100-200 nm) metal film, consisting of either a 4-layer stack of Ti/Au or a single layer of Al-Mn, depending on the detector wafer. The T_c and normal resistance R_n of the TES are tuned by adjusting the material properties and physical dimensions of its component layers. As the TES itself is quite small, it has a low heat capacity and therefore an intrinsically fast thermal time constant. To bring $\tau_{\rm th}$ within the range of stable ETF operation, an additional heat capacity is added to the bolometer island in the form of a 600–850 nm layer of palladium partially overlapping the TES and bias leads.

4.3 Detector Fabrication

The SPT-3G detector wafers were fabricated in the Materials Science Division and Center for Nanoscale Materials at Argonne National Laboratory. A detailed description of the fabrication process can be found in Posada et al. (2015, 2018); a brief overview is given here.

The detector wafers start as 675 μm-thick, 150 mm-diameter silicon (100) wafers coated with low-stress silicon nitride. The 300 nm-thick Nb ground plane layer is deposited and patterned to form the sinuous antennas and basic features of the triplexers and bolometers. The wafer is heated to 250° C for the deposition of the 500 nm-thick SiO_x dielectric layer to ensure a conformal film. For nine of the ten wafers in the focal plane, both the termination resistors and the TESs are then deposited as thin films of Ti/Au (Carter et al. 2018), whereas the TES material for wafer w206 is a single layer of aluminum-manganese (Anderson et al. 2019). A thin bilayer of Ti/Au is added to the TES and resistor edges to prevent interactions between the Nb top layer and Ti, as this was found to degrade the TES transitions. The top layer of Nb is then deposited and patterned using a two-step process: lift-off for the TES and resistor leads and etching for the microstrip and array-level wiring. The additional Pd

heat capacity is then deposited on the bolometer islands partially overlapping the TES to ensure good thermal connection. Lastly, the wafers are diced to their final dimensions, and a XeF_2 etch removes the silicon beneath the bolometer islands. Detector wafers are fabricated in batches of five, with each batch taking approximately three weeks to complete.

4.3.1 Detector Parameter Targets

The fiducial detector parameter targets for SPT-3G are collected in Table 4.3. Based on these numbers and the formulas in Table 4.2, we can expect, e.g., for 150 GHz detectors, that $\mathrm{NEP}_{\mathrm{Johnson}} \sim 0.9\,\mathrm{aW}/\sqrt{\mathrm{Hz}}$, $\mathrm{NEP}_{\mathrm{phonon}} \sim 26\,\mathrm{aW}/\sqrt{\mathrm{Hz}}$, $\mathrm{NEP}_{\mathrm{readout}} \sim 52\,\mathrm{aW}/\sqrt{\mathrm{Hz}}$, and $\mathrm{NEP}_{\mathrm{photon}} \sim 67\,\mathrm{aW}/\sqrt{\mathrm{Hz}}$, indicating the detectors will indeed be photon noise-dominated. Parameter values for detectors in the deployed instrument are discussed in Section 4.6.

Detector Parameter	Symbol	Target Range
		95 / 150 / 220 GHz
Normal Resistance	R_{n}	1.7–2.0 Ω
Operating resistance	R_{frac}	0.7–0.8 * R_{n}
Transition Temperature	T_{c}	410–480 mK
Saturation Power	P_{sat}	10.6 / 16.0 / 21.0 pW
Thermal Conductance	G	90 / 120 / 140 pW/K
ETF Loopgain	$\mathcal{L}$	5–10
Time constant	τ_{th}	1–7 ms
Band center	ν_0	93 / 148 / 222 GHz
Bandwidth	$\Delta\nu$	29 / 44 / 54 GHz

Table 4.3: Fiducial parameter target values for SPT-3G TES bolometers.

4.4 Detector Module Assembly

Once the silicon detector wafers are fabricated, they are packaged in a detector module providing the mechanical and electrical connections to the rest of the instrument. Figure 4.9 shows an exploded view of a detector module, primarily consisting of the detector and lenslet wafers clamped together in an invar frame. An absorber-covered backplate provides protection for the bolometers and wire bonds in addition to providing a mounting point for the multiplexing LC circuit boards.

The rest of this section details the assembly of the detector modules, shown pictorially in Figure 4.10. I was heavily involved in this process from early on, designing the assembly jigs and flex cables and assembling the earliest modules myself. Once procedures were established, module assembly for SPT-3G was performed by Fermilab engineering physicist Donna Kubik.

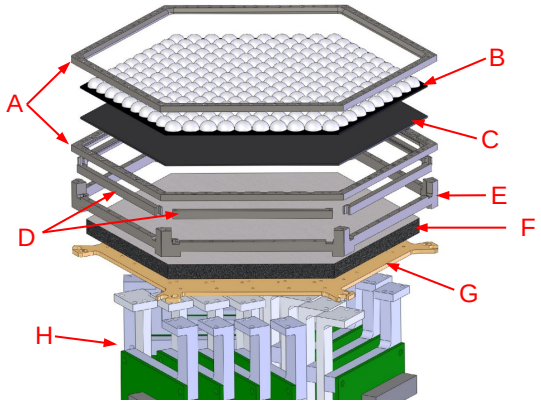

Figure 4.9: Exploded view drawing of a detector module. An invar frame (A) clamps together the lenslet wafer (B) and detector wafer (C). The flex cables (not shown) are mounted on the bottom of the frame and secured in place with clamps (D). The mounting bracket (E) attaches to the frame at the six corners, and provides the connection to the detector cold stage. A backplate (G) covered in foam absorber (F) protects the detectors and wire bonds, in addition to providing a mounting point for the LC readout boards (H).

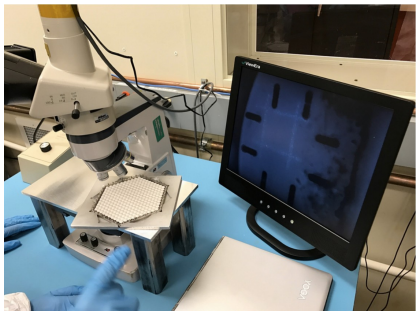

(a)

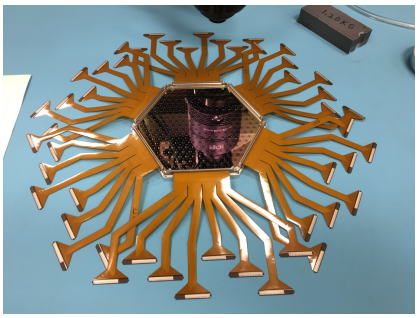

(b)

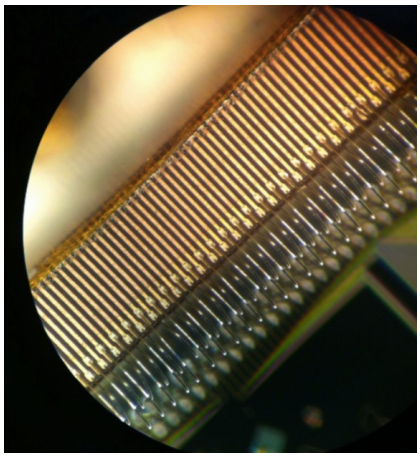

(c)

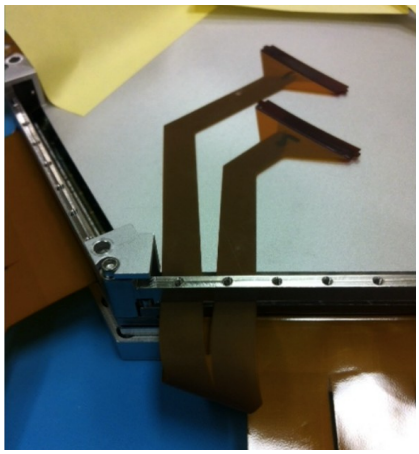

(d)

(e)

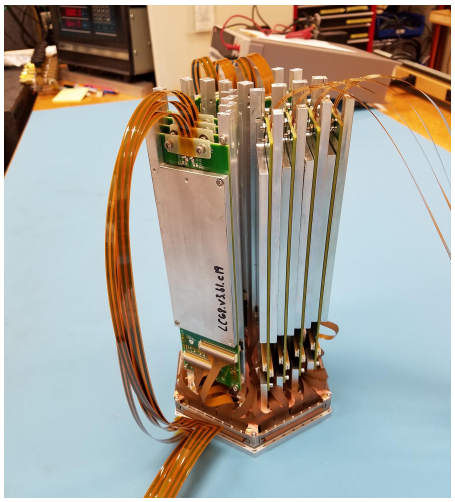

(f)

Figure 4.10: Photos showing assembly of a wafer module. See main text for further details. Photos (a)-(e) courtesy of Donna Kubik.

4.4.1 Lenslet Wafer Alignment

The lenslet seating wafer and detector wafer are aligned in a manual process with the aid of an infrared microscope (Figure 4.10a). A lamp illuminates the stack from below, shining through etched alignment marks in the detector wafer. Infrared light is transmitted through the overlying lenslet wafer and received by an IR-sensitive camera, which also views alignment marks on the lenslet wafer illuminated with optical light. The marks are shown on a display, and the wafers are adjusted manually with tweezers until the marks align. The process is repeated for six alignment marks, one in each corner of the hexagon. Once the wafers are aligned, they are clamped together in an invar frame with 42 0-80 screws. We omit screws at the corners of the hexagon, as it was found clamping the wafers at these locations often led to fractures in the silicon.

4.4.2 Flex Cables and LC Board Mounting

The wiring traces for all detectors are routed to the edges of the wafer, where they terminate in pads that are then wire bonded to a custom flexible printed circuit, or flex cable (Figure 4.10b). The flex cable is aligned with the bond pads on the wafer and fixed in place with GE varnish. Once set, wire bonds are made between the cable and wafer via an automatic wire bonder (Figure 4.10c). After bonding, the flex cables are clamped to the frame to further secure them, and the invar mounting bracket is attached. The flex cable legs are then woven back through the bracket, with a temporary fixture installed to prevent damage to the exposed detectors (Figure 4.10d). After the cables are woven through, the temporary fixture is removed and replaced with the backplate (Figure 4.10e).

The backplate serves both to protect the detectors and to support the LC boards. The detector-facing side of the back plate is covered with microwave absorber (Eccosorb AN-72) to absorb power from the antenna back lobe. A foam absorber was desired, as a solid or castable absorber (e.g., MF-110 or CR-110) could obstruct screw holes in the backplate. Eccosorb HR-10, used in other locations of the receiver and in particular throughout the

optics cryostat, was unacceptable in this proximity to the detectors given the material's high degree of shedding. The center of the AN-72 is adhered to the backplate through a small blob of Stycast epoxy, while the corners are supported with small loops of fishing line. With the backplate installed, the flex cable ends are plugged into the LC boards, and each LC board is secured to the backplate with six 0-80 screws (Figure 4.10f). Once all twelve LC boards are installed, an additional end support is added to connect the LC boards together and add rigidity to the assembled module.

4.5 Pre-Deployment Detector Testing

Detector testing for SPT-3G was a large program, working through many generations of prototype devices over the course of several years to iteratively inform the fab process and arrive at the best set of detectors. Many institutions were involved in testing as their cryostats came online, with the University of Chicago among the first to begin testing devices. My testing of SPT-3G detectors at UChicago primarily utilized the former SPT-SZ receiver cryostat, pictured in Figure 4.11. Similar to the SPT-3G receiver, the SPT-SZ cryostat uses a CryoMech PT-415 pulse tube cooler to reach 4 K and a Simon Chase He-10 sorption refrigerator (model CRC10) to cool the detector cold stage to 250 mK. The sub-Kelvin assembly is the same as utilized for SPT-SZ, with the detector cold stage modified to accommodate one SPT-3G detector module. Detector operation and readout was initially performed with SPTpol-era electronics, before transitioning to SPT-3G electronics to test the new detectors and readout as an integrated system.

Detectors were tested with the cryostat in one of two configurations: "dark" and "optical". In the optical configuration, a window and series of filters are installed (see Figure 4.15) such that the detectors are optically coupled to the room. This configuration is used to test the bandpasses of the detectors, their optical time constants, and their polarization properties. In the dark configuration, the window is removed and the optical stack replaced with blanking plates. An internal thermal source, referred to as a cold load, may be installed in

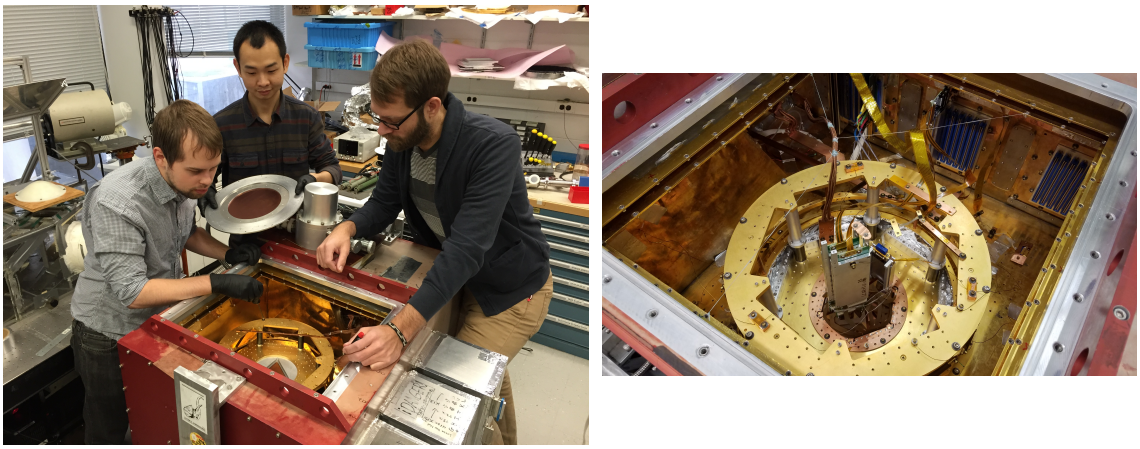

Figure 4.11: Photographs of the former SPT-SZ receiver now used as a lab cryostat. *Left:* From left to right: myself, Zhaodi Pan, and Tyler Natoli work on the cryostat. The FTS, thermal source, and coupling mirror are visible along the left edge of the photo. *Right:* Interior of the cryostat with devices installed for testing.

the cryostat in this configuration to deposit a controlled amount of power on the detectors and thus measure their optical efficiency. Alternatively, the cold load can be omitted and the detectors further blanked off at 250 mK to reduce the amount of optical power as much as possible.

4.5.1 Dark Testing

Perhaps the most basic measurement to make of a TES is to map out its superconducting transition, resulting in an RT curve as shown at the beginning of this chapter in Figure 4.1. To make this measurement, a very small fixed sense voltage is applied to the TES as the detector cold stage is slowly swept through a range of temperature. Usually there is some thermal impedance between the silicon of the detector wafer and the position of the cold stage thermometer, such that slow changes in temperature (on the order of 3 mK/minute) are required to not skew the result. An upwards sweep and a downward sweep are performed, and the average of the two is used to determine T_c. The RT curve also yields the TES R_n and R_{stray}, though as with many of the measurements made with the DfMux system, frequency-dependent transfer functions must be understood to correctly interpret the results.

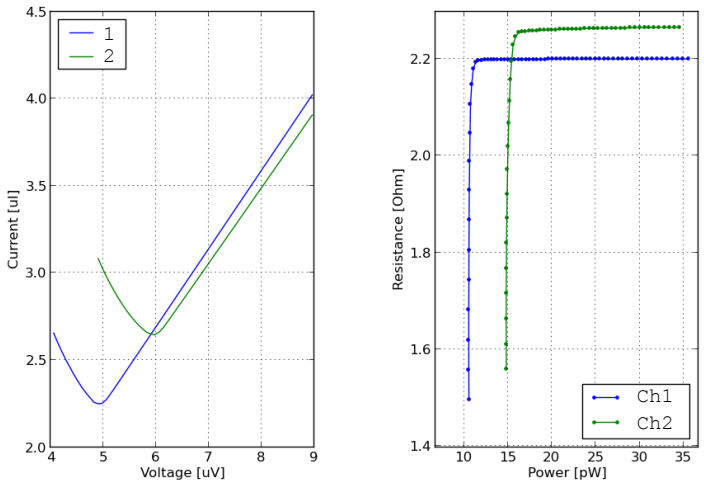

Figure 4.12: Sample current vs. voltage (IV) and resistance vs. bias power (RP) curves for two TES devices.

The other basic measurement for TES bolometers is output current as a function of applied voltage bias, or an IV curve, examples of which are shown in the left panel of Figure 4.12. On the right side of the graph, the applied bias voltage is sufficient to keep the TES in its normal phase, but as the voltage is lowered, the TES begins to enter the superconducting transition, at which point the sudden drop in resistance causes the current to increase rapidly, resulting in the "turn-around" in the IV curve. The same I and V information can be used to construct the RP curves shown in the right panel of Figure 4.12, which map the TES transition as a function of applied bias power rather than stage temperature, yielding a measurement of bolometer saturation power P_{sat}. IV curves can also be taken with the detector cold stage at various temperatures, and the resulting data fit to Eq. 4.2 to measure the thermal conductance G of the bolometer, in addition to providing another means of measuring T_{c}. I show an example of such a fit in Figure 4.13.

The optical efficiency of the detectors can be measured by installing a temperature-controlled blackbody, or cold load, in the cryostat. The construction of the cold load used in the test cryostat is discussed in Pan et al. (2018); the emitting material is a polypropylene-based radar absorbing material purchased from TK Instruments[2] mounted on a sheet of

2. http://www.terahertz.co.uk/

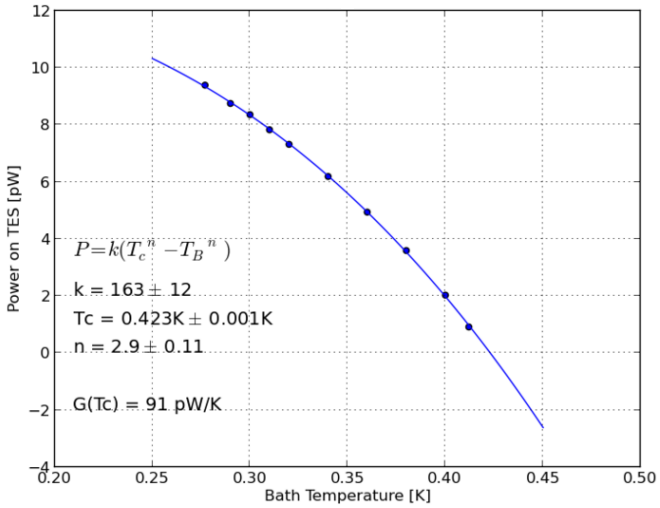

Figure 4.13: Sample P_{el} vs. T_{bath} data. The points are fit to the formula shown within the plot to yield a measurement of bolometer thermal conductance G.

OFHC copper, which is stood off from the cold load box by thermally-isolating G10 legs. Heater resistors and thermometers adjust the temperature of the cold load via a PID control loop. Metal-mesh low-pass filters are installed on the front of the cold load to limit excess power on the cold stage from radiation outside the detector bandpasses. As the cold load increases in temperature, more optical power will be deposited on the detectors, requiring less electrical power to reach the same R_{frac}. The absorbed optical power can be compared to the theoretical power emitted from a blackbody at temperature T, and the detector optical efficiency calculated. In Figure 4.14, I show such a measurement that I carried out for two prototype devices, exhibiting optical efficiencies of 0.7–0.8.

Optical efficiency proved to be one of the trickier measurements to carry out and prone to systematic error. Excess loading from the cold load can raise the temperature of the detector cold stage, decreasing the required P_{el} and artificially increasing optical efficiency. A PID control loop adjusting the temperature of the cold stage can help combat this; however, an increasing thermal gradient may still form between the cold stage and the detector wafer as the cold load emits more power: for a 15 K cold load, I measured this gradient to be ∼25 mK. To account for changing temperature of the detector wafer, we monitor the change in P_{el}

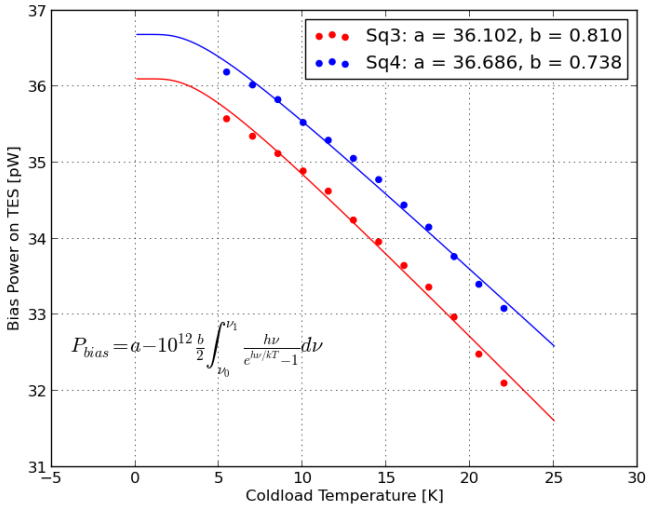

Figure 4.14: Sample optical efficiency data for two prototype high-P_{sat} devices. *IV* curves are taken with the cold load at different temperatures, and the data fit to $P_{\mathrm{el}} = P_{\mathrm{tot}} - P_{\mathrm{opt}}$. The optical power is calculated from the blackbody formula, where the integral over frequency includes the simulated or measured (if available) detector bandpasses and the transmission of any intervening filters. The parameter a is the P_{sat} of the detector, while b is optical efficiency.

for bolometers that have purposely been disconnected from their antennas, and then correct for this change in the optical bolometers. This correction usually reduces optical efficiencies from > 1 to within the expected range of 0.7–0.8.

4.5.2 Optical Testing

Additional measurements of the detectors' optical properties are made by coupling them to sources of optical power external to the cryostat. To prevent 300 K blackbody radiation from overloading the cryostat cold stages or saturating the detectors, we use a series of optical filters as pictured in Figure 4.15. Infrared radiation is reduced through stacks of alternating Zotefoam and expanded PTFE mounted at both 50 K and 4 K; the PTFE serves to thermally insulate the Zotefoam sheets, allowing successive layers to radiatively cool. Low-pass metal mesh filters block out-of-band loading, while an absorptive filter of Eccosorb MF-110 reduces the in-band power from $\mathcal{O}(100\,\mathrm{pW})$ to just a few pW.

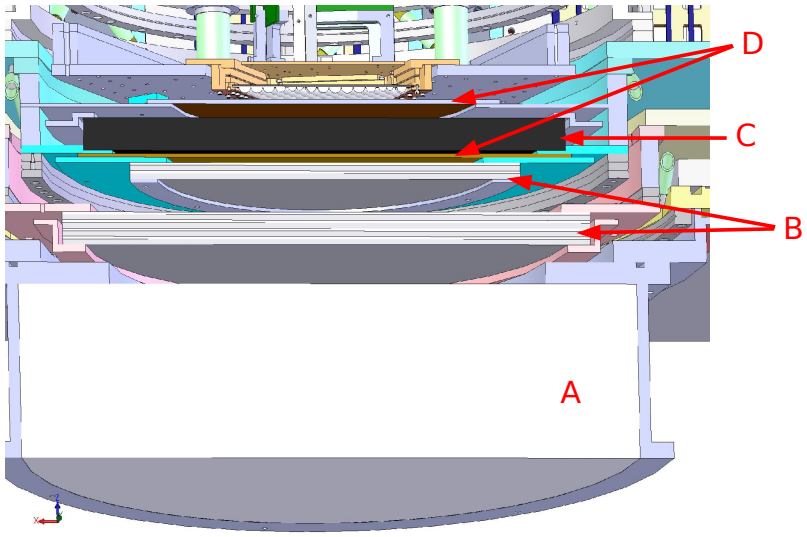

Figure 4.15: Cutaway drawing of the optical stack for the test cryostat showing (A) Zotefoam vacuum window (B) Infrared filters consisting of alternating layers of Zotefoam and expanded PTFE (C) In-band absorptive filter consisting of 0.75 in of Eccosorb MF-110 (D) Low-pass metal-mesh filters.

A primary optical measurement is that of the detector bandpasses, typically made through the use of a Fourier Transform Spectrometer (FTS). The FTS is a polarizing Michelson interferometer, in which an input optical signal is split between two paths with a continuously changing optical delay. The recombined signal is then transmitted to a detector, where the set of constructively and deconstructively interfering frequencies produce an interferogram, the Fourier transform of which is the detector bandpass. The particular FTS I used in conjunction with the test cryostat was constructed by Shoemaker (1980), while the new compact FTS commissioned for SPT-3G and used at the South Pole is detailed in Pan et al. (2019). Figure 4.16 shows an example of the bandpasses I measured in the lab; further discussion of the bandpasses measured on the full instrument is in Section 4.6.

Additional optical measurements performed in the lab include measuring the detectors' polarization response and their optical time constants. To measure polarization response, a chopped thermal source is placed in front of the cryostat window behind a rotating polarizer grid, and the detector signal as a function of polarizer angle is recorded. Figure 4.17 shows an example measurement, though it should be noted that because of internal reflections

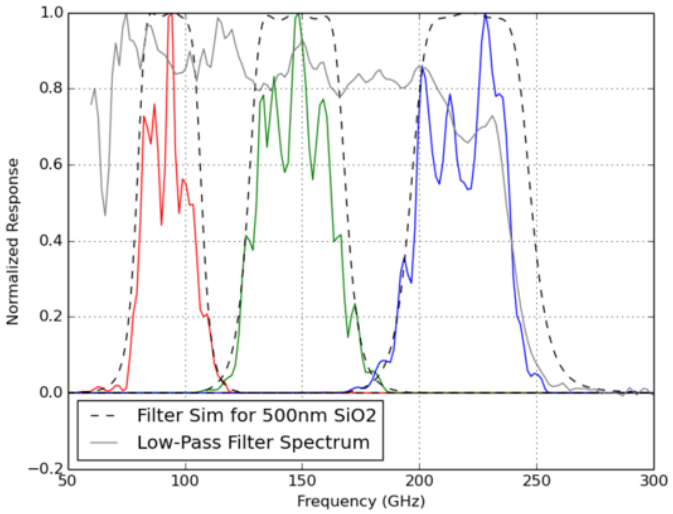

Figure 4.16: Detector bandpasses for a potential deployment wafer measured with a Fourier transform spectrometer (FTS). The dashed lines indicate the nominal simulated bandpasses, while the overlaid faint gray line shows the combined transmission for the low-pass filters installed in the test cryostat, which truncate the upper edge of the 220 GHz band. The structure in the bandpasses is likely caused by channel spectra—interference between multiply reflected beams—within the test cryostat optical path.

in the test cryostat, the level of cross-polarization should be taken as an upper bound. The same chopped thermal source is used for measuring optical time constants, with the detectors' response recorded as a function of chopping frequency. Figure 4.18 shows such a measurement for a single detector operated at different values of R_{frac} to demonstrate the increase in $\mathcal{L}$ and corresponding decrease in τ_{th}. The same technique is used for measuring the full instrument detector time constants *in situ*, with the chopped thermal source installed on the telescope as described in Section 5.1.1.

4.6 Deployed Array Characterization

SPT-3G was deployed on the telescope during austral summer 2016-2017, and since that time has operated with three different set of detectors. The first set of ten detector wafers had higher P_{sat} values than the nominal targets, which in part was a conservative choice

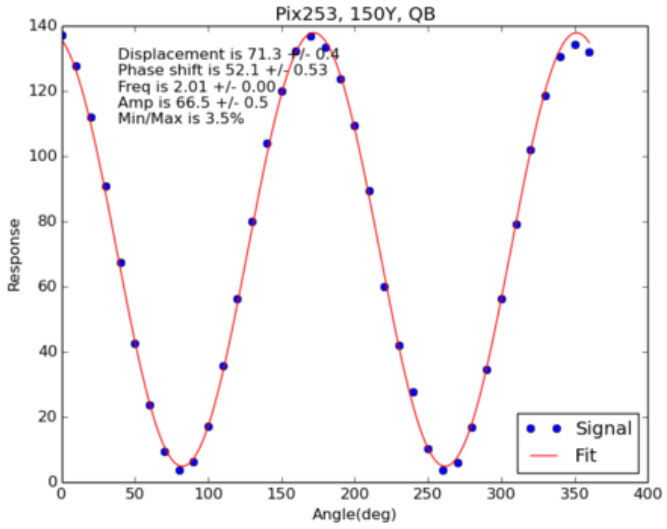

Figure 4.17: Polarization response of a single detector installed in the test cryostat. A chopped light source is placed in front cryostat window behind a 45° rotating polarizer. The detector's response is then measured as a function of polarizer angle and fit to a sinusoid. The cross-polarization response should be taken as an upper bound, as there may be polarized reflections within the test cryostat optics.

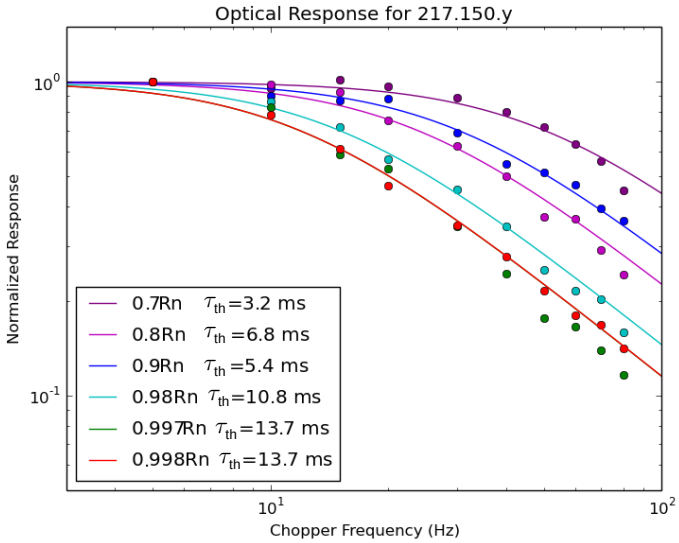

Figure 4.18: Optical time constant as a function of R_{frac} for a single detector measured in the test cryostat. The detector's response to a chopped thermal source is measured as a function of chopping frequency, and the results fit to a single-pole roll-off to yield τ_{th}. Deeper in the transition, $\mathcal{L}$ increases and speeds up the detector response.

to mitigate the risk of higher-than-expected optical loading on the brand-new instrument; however, $P_{\rm opt}$ on the telescope proved to be in line with predictions, and ten new detector wafers with lower values of $P_{\rm sat}$ were installed for the 2018 observing season (Dutcher et al. 2018). In the spring of 2018, an issue with the telescope drive system caused damage to readout electronics within the cryostat, requiring the cryostat to be opened and two of the detector wafers to be replaced. Since 2019, SPT-3G has been operating smoothly, and there are no plans for further modifications.

Selected parameter values for the deployed wafers are summarized in Table 4.4. For completeness, I include detectors deployed in either 2018 or 2019+, indicating which years a given wafer was on the telescope. Detector wafers were fabricated in batches of five, with occasional changes to target parameters and layer geometries based on feedback from laboratory testing, so some variation across batches is expected. The horizontal lines in the table group wafers into these fabrication batches. The dark properties of $T_{\rm c}$, $P_{\rm sat}$, and G are collected from the results of laboratory testing, while $R_{\rm n}$ and $\tau_{\rm th}$ are measured on the telescope. Not all wafers were tested in dark cryostats before deployment, resulting in gaps in the table; however, at least one wafer from each fabrication batch was tested dark, allowing us to extrapolate the properties to the untested wafers. There is general agreement with the parameter targets, and we expect no degradation to instrument performance due to the detectors. To better indicate the uniformity of parameters within a wafer, in Figure 4.19 I show the spread in $R_{\rm n}$ across all currently fielded wafers and in $T_{\rm c}$ for selected wafers tested in the lab.

4.6.1 Bandpasses

I measured the bandpasses of the instrument at the South Pole prior to installation on the telescope using the cryostat configuration pictured in Figure 4.20. The compact FTS is mounted on a pair of linear stages, allowing the FTS to scan across the image of the focal plane formed just exterior to the cryostat window by the cold optics. A mylar beam splitter

Wafer	'18	'19+	R_n (Ω)	T_c (mK)	P_{sat} (pW) 95 / 150 / 220	G (pW K^{-1}) 95 / 150 / 220	τ_{th} (ms) 95 / 150 / 220
w172	✓	✓	2.1	423	11 / 12 / 12	99 / 112 / 112	8 / 10 / 6
w174	✓	✓	2.2	414	11 / 14 / 14	108 / 151 / 139	10 / 10 / 8
w176	✓	✓	2.2	493	15 / 17 / 18	102 / 120 / 120	5 / 5 /4
w177	✓	✓	2.1	487	13 / 15 / 15	100 / 116 / 115	4 / 4 / 3
w180	✓	✓	2.0	460	–	–	7 / 7 / 5
w181	✓	✓	2.0	469	12 / 14 / 14	111 / 124 / 122	5 / 6 / 3
w187	✓		2.0	458	–	–	5 / 5 / 3
w188	✓	✓	2.0	459	11 / 13 / 12	90 / 109 / 104	9 / 8 / 7
w201	✓		2.7	–	–	–	6 / 5 / 2
w203	✓	✓	2.6	–	–	–	4 / 5 / 2
w204		✓	2.7	432	11 / 16 / 18	103 / 136 / 157	4 / 4 / 2
w206		✓	1.8	444	10 / 13 / 15	85 / 113 / 128	5 / 4 / 2

Table 4.4: Median values of detector parameters for deployed SPT-3G wafers, with deployment years indicated. Horizontal lines group wafers into fabrication batches, and parameters are split by observing band where relevant. Some testing data were not available for all wafers.

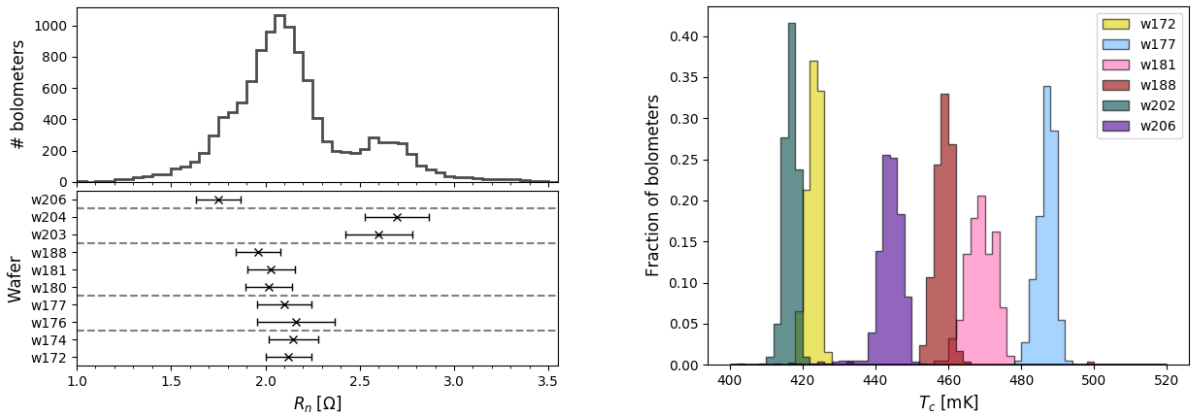

Figure 4.19: *Left:* Histogram of R_n values across all deployed devices, along with the median value and standard deviation on each wafer. Dashed lines in the bottom panel indicate changes in the TES layer stack or material. *Right:* Histogram of T_c values for wafers tested in lab cryostats. One wafer from each fabrication batch represented in the focal plane is included.

and beam scoop redirect most of the detectors' power to the sky, coupling only a small fraction to the output of the FTS in order to prevent saturation. The FTS operation can be entirely automated, with the FTS programmed to move to the position of the targeted

Figure 4.20: Photograph of the SPT-3G cryostat at the South Pole configured for automated FTS measurements. The input thermal source to the FTS, the FTS itself, and a coupling mirror+beam scoop are attached to a pair of computer-controlled linear stages mounted to the cryostat.

detectors, the detectors tuned into their transitions, the FTS ran, and the detectors re-overbiased before the FTS moves to the next set of detectors. This automated routine enabled the collection and analysis of thousands of bandpass measurements in just a few days.

The raw measured spectra need to be corrected for the spectral dependence of the input thermal source of the FTS as well as the reflection off the 1–2 mil-thick mylar beam splitter. Each of these terms goes as ν^2, requiring a ν^{-4} correction to yield accurate bandpasses. To obtain the bandpasses of the on-wafer triplexer filters, one must further correct for the internal etendue and spillover on the Lyot stop; here I do not perform these corrections so as to present the effective instrument bandpasses. Figure 4.21 shows the measured bandpasses for detectors currently on the telescope with per-band summary statistics in Table 4.5. Overall, they show excellent agreement with the fiducial targets presented earlier, though with a slightly reduced 150 GHz bandwidth. The bandpasses for the 2018 instrument, the data of which I analyze later in this thesis, are consistent with the bands shown here to within uncertainties.

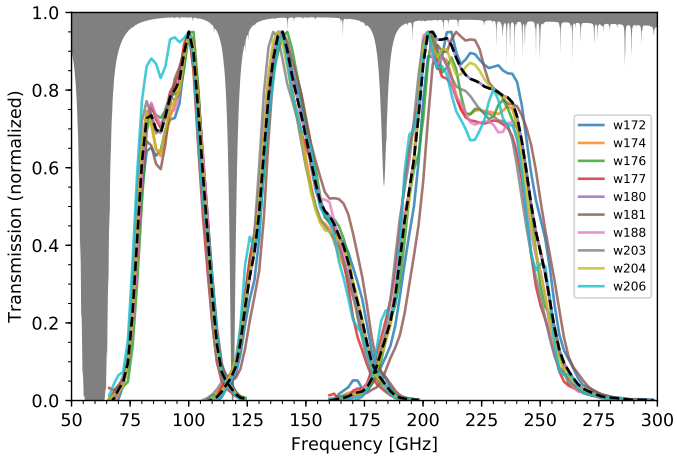

Figure 4.21: Measured bandpasses for SPT-3G detectors. The solid lines are the average bandpass measured for each wafer, and the dashed line is the average of all wafers. The shaded region indicates atmospheric transmission for 0.25 mm PWV. Bandpasses have been arbitrarily normalized.

	95 GHz	150 GHz	220 GHz
Band center (GHz)	93.8 ± 0.7	147.0 ± 1.2	219.9 ± 2.0
Bandwidth (GHz)	26.4 ± 1.2	32.5 ± 0.7	53.6 ± 1.9

Table 4.5: Measured band centers and bandwidths for SPT-3G instrument. Band center is defined as $\int \nu f(\nu) d\nu / \int f(\nu) d\nu$, and bandwidth is $\int f(\nu) d\nu$. The uncertainties reflect the spread across detector wafers.

4.6.2 Yield

Wired Bolometers	Passed Warm Connectivity	Identified Resonances	Attempt to Operate
15,720	93%	91%	74%

Table 4.6: Bolometer yield breakdown for 2019+ focal plane.

Table 4.6 breaks down the number of operable detectors in the instrument as installed in 2019. There are 16,140 bolometers in the focal plane, though the readout electronics permit us to connect to only 15,720. Of these wired bolometers, slightly over 90% pass a warm connectivity test, in which we probe each wafer on the benchtop for shorts to ground, shorts between neighboring detectors, shorts bypassing the TES, or open connections. Almost

all of the detectors that pass this test are later identified with resonant peaks in network analyses, indicating very few losses due to the multiplexing circuit or handling of the modules during installation. Once in the cryostat, detectors are excluded from operation for a variety of reasons, including no observed superconducting transition, no optical response, ragged-looking network analyses, or a resonant frequency too close to that of another detector. Each wafer also houses a number of dark detectors, purposely left unconnected to the pixel antenna to test for non-optical signals, that we also choose not to operate. Together, these cuts reduce the number of detectors used during data collection to slightly under 11,700. Prior to 2019, the detector count was reduced further by the damaged readout mentioned previously, leaving approximately 8400 bolometers operable during the latter half of 2018.

CHAPTER 5

MAKING MAPS OF THE CMB

5.1 Survey Field and Observation Strategy

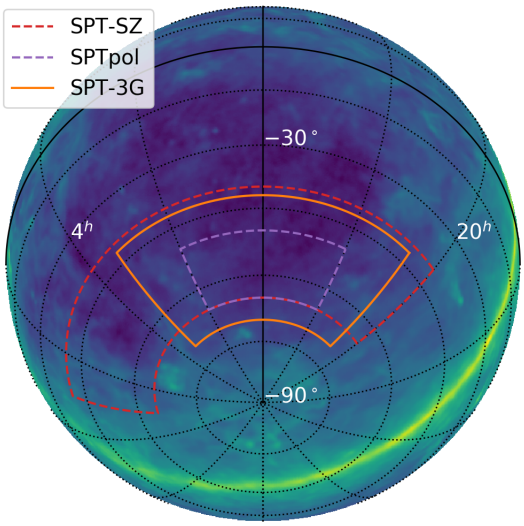

Figure 5.1: Boundaries of the main survey regions observed by instruments on SPT overlaid on a thermal dust map from Planck Collaboration et al. (2020a): the SPT-3G 1500 deg^2 field *(orange, solid)*, the SPTpol 500 deg^2 field *(purple, dashed)*, and the SPT-SZ 2500 deg^2 field *(red, dashed)*.

The main SPT-3G survey field is a ∼1500 deg^2 patch of sky extending from −42° to −70° declination and from $20^{\rm h}40^{\rm m}0^{\rm s}$ to $3^{\rm h}20^{\rm m}0^{\rm s}$ right ascension, covering 3.76% of the full sky. The survey footprint is shown in Figure 5.1 along with those of previous instruments on SPT. This region of sky is also observed by the BICEP/Keck family of CMB instruments, enabling joint analysis of SPT and BICEP/Keck data products. We observe the full survey region via four 7.5°-tall subfields each covering the full RA range and centered at −44.75°, −52.25°, −59.75°, and −67.25° declination, respectively (Figure 5.2). The telescope observes each subfield in a raster pattern, performing constant-elevation scans across the full azimuth range and back again before making a small step in elevation and repeating (at the South Pole the local coordinate system of azimuth and elevation correspond directly to right ascension

and negative declination, respectively, greatly simplifying the mental conversion between telescope movement and celestial coordinates). The main scan direction is along azimuth, as scanning in elevation causes the detectors to stare through an air column of varying thickness, altering the effective brightness of the atmosphere and shifting the operation point of the TESs. Short, elongated subfields as shown in Figure 5.2 minimize potential responsivity variation and also lead to higher-efficiency observing.

The efficiency of a telescope schedule is the ratio of time spent collecting data to the time spent on other telescope movement. For this rastering scan strategy, only the constant-velocity portion of a scan is kept, while the data taken during telescope turn-arounds and elevation steps are discarded. Observing elongated subfields is more efficient, as proportionally less time is spent changing direction. The speed at which the telescope scans is also an important factor, as acceleration limits require the telescope to take more time to reach higher velocities, necessitating longer turn-arounds. The scan speed of the telescope had two settings during 2018, briefly maintaining a constant 0.74 deg/s as measured on the sky before changing to a constant 1.0 deg/s rotation on the azimuth bearing for the rest of the season. For a scan at declination δ, these two measures of angular speed are related by

$$\omega_{\text{sky}} = \omega_{\text{bearing}} \cos(\delta) \ . \tag{5.1}$$

While a constant speed on-sky simplifies analysis, as a given signal frequency always maps to the same angular scale, the high velocity required in the highest elevation field led to low-efficiency schedules, as the telescope acceleration had been restricted to 0.38 deg/s^2 to reduce vibrational heating of the sub-Kelvin assembly (for contrast, after replacing the sub-Kelvin assembly in 2019 the telescope acceleration was increased to 0.60 deg/s^2). All but the earliest observations in 2018 use the 1.0 deg/s on-bearing scans, taking 104 s to cover the azimuthal range and an additional 12 s to reverse direction, resulting in 90% scan efficiency. With scan speed set, the total time for each observation depends on the number of scans

required to cover the subfield, and therefore on the size of the elevation steps. The precise value has varied in order to fit the desired number of observations within the hold time of the helium sorption fridge, but is typically in the range $7.5'$–$12.5'$, with the starting position of subsequent observations of the same subfield adjusted by $0.5'$ to ensure even coverage. Each subfield observation takes approximately 2.5 hours to complete, with two subfields each being observed three times in one day.

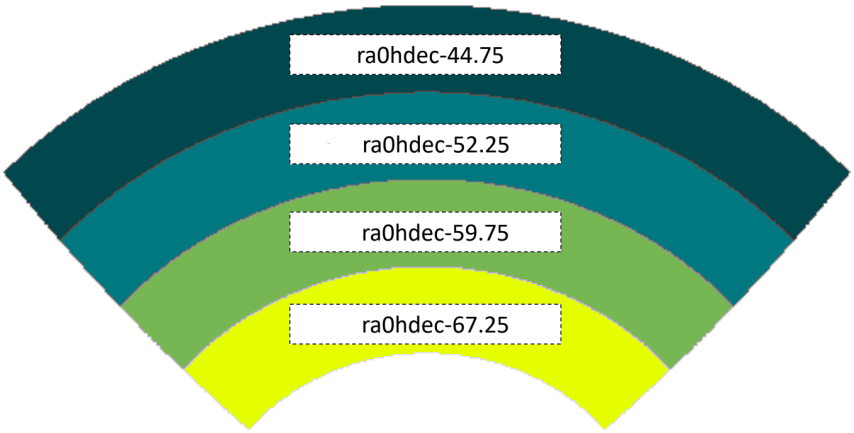

Figure 5.2: Diagram of the four subfields comprising the 1500 deg^2 field.

5.1.1 Calibration Observations

Before each subfield observation, we conduct a series of calibration observations used to relate the power on each detector to CMB fluctuation temperature. This conversion is derived from observations of two Galactic HII regions that serve as relatively compact sources of mm-wave flux, RCW38 and MAT5a (NGC 3576). RCW38 is located at RA: $8^{\mathrm{h}}59^{\mathrm{m}}5^{\mathrm{s}}$ Dec: $-47°30'36''$ and is used for the two lower-elevation fields, while MAT5a is located at RA: $11^{\mathrm{h}}11^{\mathrm{m}}53^{\mathrm{s}}$ Dec: $-61°18'47''$ and is used for the two higher-elevation fields. Dense scans are taken such that each pixel in the focal plane can form a complete map of the source; these per-detector maps are then compared to flux-calibrated maps from the SPT-SZ experiment, which in turn are calibrated against *Planck* (Planck Collaboration et al. 2016a), yielding a flux calibration for every detector. These measurements take roughly 1.5 hours to complete,

a not insignificant fraction of an observing day, and so are not performed immediately before every subfield observation; during 2018 a dense observation of either RCW38 or MAT5a was taken once per day (according to the pair of subfields to be observed that day), while in 2019 the frequency was reduced to approximately once per week per source. Instead, before each subfield observation the telescope performs sparse scans of the HII regions that take less than 10 minutes to complete, and by comparing these results to the most recent dense observation, a per-band scaling factor can be computed. This is the chief manner by which we account for changes in sky opacity caused by fluctuating weather.

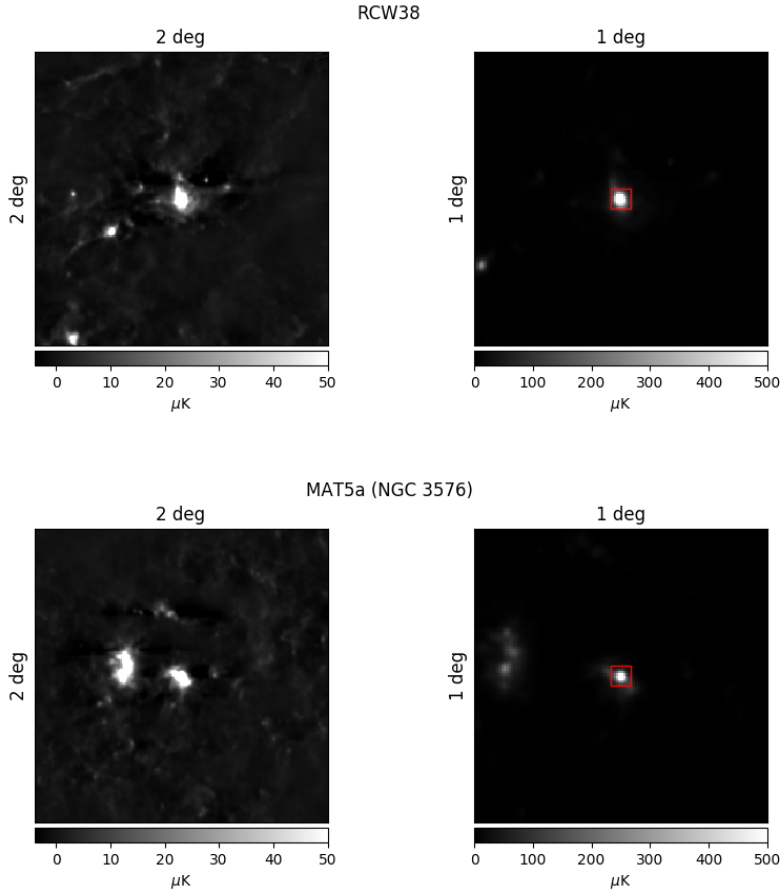

Figure 5.3: Maps of the HII regions RCW38 and MAT5a used for calibration, produced with SPT-3G 220 GHz data. The images on the left show the diffuse structure in the surrounding region, while the images on the right show the bright cores with the $4' \times 4'$ region used for calibration indicated.

Neither HII region used for calibration is within the main 1500 $\deg^2$ field, which could

cause a bias if there were more atmospheric loading in that part of the sky due to weather, or if the detectors' temperature or operation points shifted during the telescope slew from the HII region to the observing field. To make a quantity measured in one part of the sky transferable to any other part of the sky, we utilize an internal calibration source ("the calibrator"). Pictured in Figure 5.4, the calibrator is a small box mounted behind a shuttered aperture in the secondary mirror that contains a thermal IR source and a chopping wheel. During a calibrator stare, the calibrator signal is modulated at 4 Hz, and the peak response of each detector to this signal is recorded. The response of a detector to RCW38 or MAT5a is recorded in units of its calibrator response, and another calibrator stare conducted immediately before a subfield observation is used to scale the power-to-CMB-temperature relation accordingly. We expect this per-observation calibration to be accurate to ∼several percent, and we perform a final calibration on our full-season coadded data via cross-correlation with *Planck* (Planck Collaboration et al. 2020c), as described in Section 6.5.1.

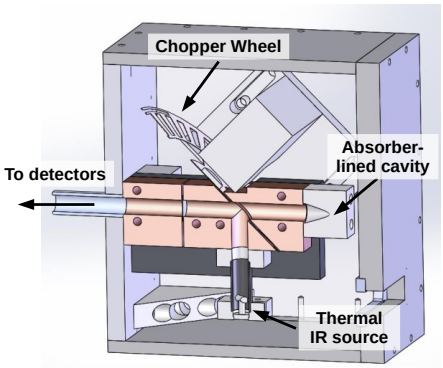

Figure 5.4: Cutaway rendering of the calibrator box. The calibrator is mounted behind a 0.5 inch aperture in the secondary mirror and contains a reflective chopper wheel mounted at 45° to alternately illuminate the detectors with an ambient-temperature cavity or a thermal IR emitter. Figure from Pan et al. (2018).

The final type of calibration observation undertaken by the telescope consists of a roughly 2° nod in elevation ("elnod") and is used within the IQ demodulation scheme to ensure the demodulated signal is in-phase with the detector response (refer to Section 3.1.1). The change in atmospheric loading during an elnod induces a large signal in the bolometers; we

adjust the phase angle of the demodulator to ensure that all of this signal is in I and none in Q.

5.1.2 Data Transfer, Format and Processing

To get data back from the South Pole in close to real time, we rely on data transfer via satellite. SPT-3G can produce well over 1 TB of raw data in 24 hours, but we are restricted to a transfer allocation of 125 GB per day on account of limited bandwidth. To reduce the volume of data coming off the telescope, the detector time-ordered data (TOD) is encoded in FLAC, achieving compression factors of 3–4 and reducing the data saved to disk daily to around 300 GB. To fit in the satellite queue, data volume is reduced further by downsampling the TOD from their native sample rate of 152.6 Hz to 76.3 Hz, and any TOD not expected to contain meaningful information (e.g., unbiased detectors, quadrature phase TOD) are omitted. Fullrate data is added to the transfer queue if there is any space remaining, but otherwise waits until the end of an observing season to be transported out of the South Pole on hard disk. Maps of the sky take up much less disk space than the per-detector TOD used to create them; however, during the 2018 observing season the processing steps required for reliable mapmaking (see Section 5.2) at the South Pole had not yet been finalized, so all data monitoring and analysis relied on transmitted TOD. After 2018, real-time mapmaking at the South Pole has been implemented, allowing for automated checks of data quality and the transfer of high-resolution maps made from fullrate data.

In addition to transfer limits, RAM requirements are also a significant consideration for data processing, as a single fullrate observation would occupy 20–30 GB of memory if loaded in all at once. To avoid this, SPT-3G data is stored in a custom streaming file format[1] that enables only portions of a file to be loaded into memory at one time. For subfield observations, the data is broken up into segments ("frames") corresponding to a single left-going or right-going scan of the telescope, plus the segments taken while the telescope is

1. https://github.com/CMB-S4/spt3g_software

changing direction. All processing steps required to turn TOD into a map operate on one scan frame at a time.

The majority of SPT-3G data processing, including the analysis in this thesis, is conducted on the Open Science Grid (OSG) (Pordes et al. 2007; Sfiligoi et al. 2009), a distributed network of high-throughput computing facilities available for opportunistic usage. The requirements of SPT-3G data have been targeted to match the largest number of resources on OSG, typically single-core CPUs with 2 GB of RAM. For the 2018 data, making a map for one subfield observation with the steps detailed below takes approximately 5 CPU hours, with the majority of processing time spent high-pass filtering the detector TOD.

5.2 Data Reduction

In this section, I include particular filtering steps used for the SPT-3G 2018 *EE*/*TE* power spectrum analysis, though the general framework described will be similar for separate analyses. As in prior SPT analyses, we bin detector TOD into maps using the Lambert azimuthal equal-area projection, here employing $2'$ square pixels.

5.2.1 Data Cuts

To prevent poor quality data from degrading a map, pathological detectors are flagged and dropped during processing. Some of the reasons to flag a detector include:

- Missing calibration or a calibrator response with signal-to-noise < 20
- Missing detector identifying information
- NaNs in the time-ordered data from readout errors
- TES is outside of desired transition range, with resistance $> 0.98 R_{\rm n}$ or $< 0.5 R_{\rm n}$.
- Detector bias or readout circuit is railed.

On average, 448 detectors are flagged in each scan for such reasons. I also flag detectors for anomalous TOD behavior, removing an average of 348 detectors per scan as a result of the following:

- Abrupt, large deviations from a rolling average, AKA "glitches". A detector is flagged if it's TOD contains one glitch over 20 sigma or more than 7 glitches over 5 sigma. The 20-sigma threshold avoided misidentifying bright point sources as glitches, though now these sources are masked while glitch-finding.
- Unphysically low variance, due to a detector becoming unresponsive after the most recent calibrator observation.
- Excess high-frequency power. Unstable SQUIDs or bolometers can have underdamped feedback loops, leading to oscillations that manifest as a forest of lines in the TOD around 8–10 Hz and harmonics thereof.

After filtering the TOD (see Section 5.2.2), a weight w_i is computed for each detector based on its noise, with the final map consisting of the weighted average of all unflagged detectors (see Section 5.2 for a more detailed discussion). The distribution of weights is examined for outliers, and detectors with weights 3σ above or below the mean after sigma clipping are flagged, on average removing another 33 detectors from each scan. In addition to removing individual detectors, I drop whole scans if there are anomalies in the telescope pointing information or if fewer than $\sim 50\%$ of bolometers pass cuts. I also have omitted all detectors on wafer w201 from this analysis, as its PSD shows very strong line response at multiples of 1.0 Hz and 1.4 Hz, the latter of which corresponds to the frequency of the pulse-tube cooler used in the cryostat. While it would be possible to notch out these lines in frequency space, the low frequency resolution in a single 100 s scan would result in a substantial loss of bandwidth, and I therefore chose to drop w201 entirely. I also cut entire observations if there was an error with data acquisition, if all detectors were flagged (e.g., as a result of a failed calibration observation), or if the fridge cycle ran out during the observation. After cuts

there are 562 subfield observations remaining, with an approximate average of 2200 active detectors in each frequency band.

5.2.2 TOD Filtering

For any specific analysis, we are usually interested in signals within a certain frequency range in the detector TOD, dictated by the angular scale of the cosmological signal and the scanning speed of the telescope. We apply a series of filters to the TOD to decrease and flatten the noise within this range. Figure 5.5 shows an example detector signal before and after such filtering. Typically the filters are specified in terms of multipole ℓ rather than Hz: we can relate a temporal frequency f in the detector's TOD to angular multipole ℓ via

$$\ell = \frac{2\pi}{\omega_{\text{sky}}} f = \frac{2\pi}{\omega_{\text{bearing}} \cos(\delta)} f \ , \tag{5.2}$$

where we have made use of Eq. 5.1, and δ is the average declination of a scan. For reference, Table 5.1 lists the TOD frequencies corresponding to selected values of ℓ at the center of each subfield. To ensure the same angular scales have the same level of filtering throughout subfields, the effective angular sample rate is recomputed for each scan.

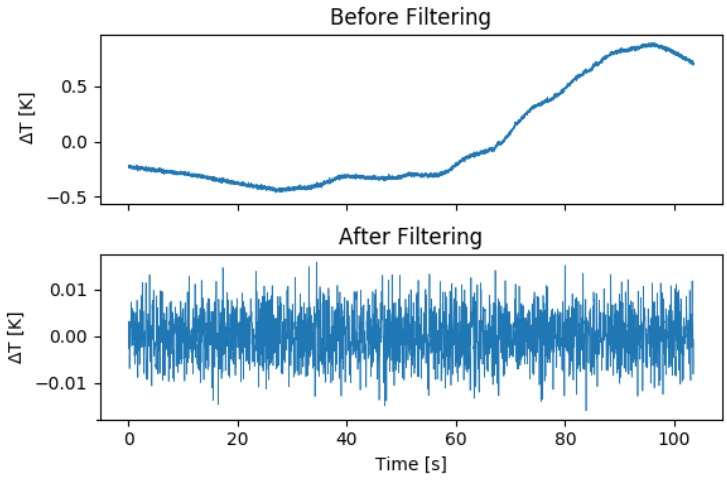

Figure 5.5: Sample detector TOD for one scan of the telescope before filtering (top) and after filtering (bottom).

	Multipole ℓ			
Field	300	1000	2000	6600
ra0hdec-44.75	0.6	2.0	4.0	13.0
ra0hdec-52.25	0.5	1.7	3.4	11.2
ra0hdec-59.75	0.4	1.4	2.8	9.2
ra0hdec-67.25	0.3	1.1	2.2	7.1

Table 5.1: TOD frequencies in Hz corresponding to selected ℓ values at the center of each subfield, assuming $\omega_{\text{bearing}} = 1.0\,\text{deg/s}$.

The chosen pixel size sets a maximum frequency that can be meaningfully represented in the output map; however, frequencies beyond this can still affect the map through aliased noise. I apply an FFT-based low-pass filter of functional form

$$e^{(-\ell/\ell_{\text{high}})^6}\ , \tag{5.3}$$

which provides many orders of out-of-band rejection with an acceptable amount of ringing around bright point sources. For $2'$ pixels I chose cutoff $\ell_{\text{high}} = 6600$.

We also typically high-pass filter the data to remove slow signals, such as those caused by a drifting cold stage temperature, that result in higher noise at low frequencies—so-called "1/f" noise. The 2018 observing season was particularly beset with 1/f noise, which was mostly attributed to an insufficiently-rigid sub-Kelvin assembly, and so I use a fairly restrictive cutoff of $\ell_{\text{low}} = 300$. Whereas the the low-pass filter is done in the frequency domain, the high-pass filter is done in the time domain through Fourier decomposition, where each mode with a frequency below the cutoff is fit to the TOD and removed. Because sines and cosines are a poor fit to e.g., a linear slope, we also project out small orders of Legendre polynomials from the TOD. I experimented with the order of polynomial and saw noticeable improvements to the noise when increasing the poly order from 4 to 19, but noted no further changes at poly order 60. I therefore fit and subtract up to a 19^{th} order Legendre polynomial from each detector's TOD in addition to the $\ell > 300$ high-pass filter. In both these steps the TOD samples corresponding to bright point sources on the sky are masked to

avoid negative filtering wings in the map, an example of which is shown in Figure 5.6. Lists of point source coordinates and fluxes previously compiled by SPT-SZ and used in SPTpol for masking did not cover the full 1500 $\deg^2$ field, so I used an initial unmasked set of SPT-3G maps to construct a new point source list, which was then used for further map-making. I detect 174 sources above 50 mJy at 150 GHz that are then masked for all three frequency bands.

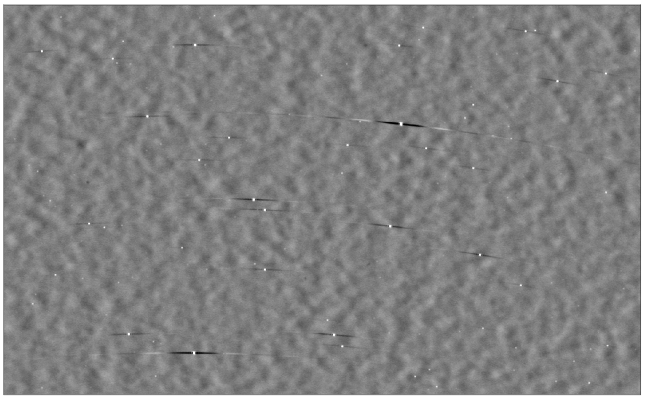

Figure 5.6: Cutout of a filtered SPT-3G map made with unmasked point sources. Large wings are present on either side of point sources along the scan direction. These features are not present in maps used for the power spectrum analysis.

I apply one additional filtering step, referred to as the common mode filter, in which the signals from all unflagged detectors within a specified group are averaged together and the result subtracted from each of those detectors' TOD, removing any common signal. Here I use all detectors in the same frequency band on the same wafer to form the common mode, effectively acting as a high-pass filter that removes temperature power on scales larger than approximately 0.4° ($\ell \sim 500$) while largely leaving polarization unaffected, as the difference in signal between detectors of orthogonal polarizations within a pixel remains unchanged. Point sources are also masked during common mode filtering, as not doing so leads to decrements in the map as demonstrated in Figure 5.7. In this implementation of the common mode filter, I use a straight average across detectors, though using a weighted average could potentially have better performance.

I compute the detector weights mentioned in the previous section using the fully-filtered

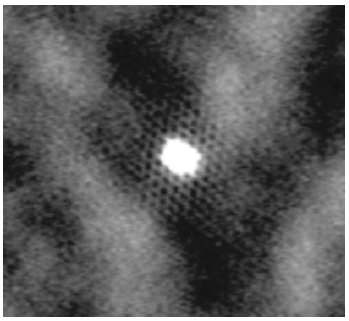

Figure 5.7: Cutout of a high-resolution SPT-3G map made with an unmasked common mode filter. The subtracted signal around a bright point source leaves decrements in the map at the locations of other pixels in the detector wafer. These features are not present in maps used for the power spectrum analysis.

TOD; detectors with higher remaining noise receive lower weights and vice-versa. As is typical of ground-based CMB experiments, the TOD are noise-dominated, permitting estimates of the noise spectrum to be taken directly from the TOD power spectral density (PSD). While the full RMS of the TOD could be used for the detector weights, this would include excess variance from frequencies outside of the main science band; therefore we usually restrict the weight to use a specified range of the detector PSD. This poses a dilemma, as the scan strategy of SPT-3G results in the mapping between timestream frequency and angular multipole ℓ varying across the field. To optimize the noise over the $1000 < \ell < 2000$ range of greatest interest here, either the range of frequencies used for computing the weights could be computed on a per-scan basis like the rest of the filters, or the range could simply be large enough to always include the multipoles of interest. For sheer simplicity I chose the latter option, with the weights being computed as inversely proportional to the PSD integrated over 1–4 Hz.

5.3 Mapmaking Formalism

We are interested in measuring both the intensity of the CMB, i.e. its effective temperature, as well as its polarization. In this section I discuss the formalism underlying our polarized mapmaking.

Light of any polarization state can be described via the Stokes vector

$$\vec{S} = \begin{pmatrix} I \\ Q \\ U \\ V \end{pmatrix} , \tag{5.4}$$

with I corresponding to intensity (hereafter denoted as T), Q to horizontal or vertical polarization, U to $+45^\circ$ or -45° polarization, and V to right-handed or left-handed circular polarization, as shown in Figure 5.8. The Stokes parameters are particularly useful, as they are easily measured by sets of total-power detectors with orthogonal polarizations, which are the types of detectors utilized in SPT-3G and most other modern CMB experiments. V is commonly ignored since the processes affecting the CMB result in linear polarization, and linearly polarizing bolometers are simpler to build and operate. Assuming detectors insensitive to V, we can write the total intensity measured by a detector with polarization angle ψ_i as

$$d_i = T + \frac{\eta_i}{2 - \eta_i}(Q \cos 2\psi_i + U \sin 2\psi_i) \tag{5.5}$$

where the polarization efficiency η is the fraction of signal not leaked into the orthogonal polarization, and we have used an overall normalization such that a detector's response to an unpolarized source is equal to T.

As Q and U depend on the orientation of the coordinate system, a convention must be followed when defining these quantities on the celestial sphere. SPT-3G makes polarized maps following the IAU convention, in which $+Q$ points towards the celestial poles and $+U$ is rotated 45° with the polarization angle ψ measured from North to East. The other prevalent convention within CMB (e.g., as used in HEALPix[2] software (Górski et al. 2005)) differs only in that ψ is effectively measured from North to West, and therefore the sign of U is

2. https://healpix.sourceforge.io/

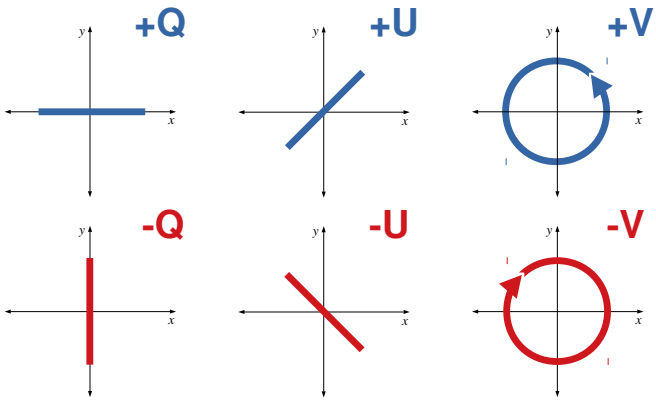

Figure 5.8: Polarization directions corresponding to the Stokes Q, U, and V parameters for 100% polarized light.

inverted. For comparison to cosmological theories, which do not care about local coordinate conventions, linear combinations of Q and U are used to construct the rotationally-invariant E- and B-modes mentioned in Chapter 1.

In this analysis, I use the same mapmaking methodology implemented for SPTpol analyses (Crites et al. 2015; Keisler et al. 2015; Henning et al. 2018) and described in Jones et al. (2007). In general, the mapmaking process consists of using telescope pointing information to bin detector TOD into pixels within a map. If $\mathbf{m}$ is a pixelized version of the true sky, we can represent a detector's data $\mathbf{d}$ as

$$\mathbf{d} = \mathbf{A}\mathbf{m} + \mathbf{n} \ , \tag{5.6}$$

where $\mathbf{A}$ is a matrix that discretely samples the sky into the TOD (with $\mathbf{A}^\intercal$ being the inverse operation binning TOD into map pixels), and $\mathbf{n}$ is a vector of random noise. I briefly note that in the absence of an explicit noise term—but still allowing for inconsistencies in the system of linear equations—this is a well-known problem in linear algebra, with the least-squares solution for $\mathbf{m}$ given by $\hat{\mathbf{m}} = (\mathbf{A}^\intercal\mathbf{A})^{-1}\mathbf{A}^\intercal\mathbf{d}$. In the presence of noise with known

covariance $\mathbf{N} = \langle \mathbf{n}\mathbf{n}^\intercal \rangle$, the optimal solution takes a similar form:

$$\hat{\mathbf{m}} = (\mathbf{A}^\intercal \mathbf{N}^{-1} \mathbf{A})^{-1} \mathbf{A}^\intercal \mathbf{N}^{-1} \mathbf{d} \ , \tag{5.7}$$

subject to conditions on $\mathbf{N}$ which are satisfied by Gaussian noise (Tegmark 1997; Jones et al. 2007).

A complete representation of the matrix $\mathbf{A}$ in this formulation is somewhat convoluted, as it encodes both which map pixel each detector is pointing to at every point in time, as well as the response of each detector to the sky. A clearer understanding can be reached by considering the contribution to $\mathbf{A}$ from a single detector time sample. If we write $\mathbf{m}$ as $\begin{pmatrix} T \\ Q \\ U \end{pmatrix}$, then by relating Eqs. 5.5 and 5.6 we immediately see

$$\mathbf{A}_{ti\alpha} = \begin{pmatrix} 1 & \frac{\eta_i}{2-\eta_i} \cos 2\psi_i & \frac{\eta_i}{2-\eta_i} \sin 2\psi_i \end{pmatrix} \ . \tag{5.8}$$

By plugging Eq. 5.8 into the right hand side of Eq. 5.7, we can identify

$$(\mathbf{A}^\intercal \mathbf{N}^{-1} \mathbf{A}) \rightarrow \frac{1}{n_i^2} \begin{pmatrix} 1 & \gamma_i c_i & \gamma_i s_i \\ \gamma_i c_i & \gamma_i^2 c_i^2 & \gamma_i^2 c_i s_i \\ \gamma_i s_i & \gamma_i^2 c_i s_i & \gamma_i^2 s_i^2 \end{pmatrix} \ , \tag{5.9}$$

$$\mathbf{A}^\intercal \mathbf{N}^{-1} \mathbf{d} \rightarrow \frac{1}{n_i^2} \begin{pmatrix} 1 \\ \gamma_i c_i \\ \gamma_i s_i \end{pmatrix} d_i \ , \tag{5.10}$$

where I have adopted the notation of Jones et al. (2007) in abbreviating the trigonometric functions and using $\gamma \equiv \frac{\eta}{2-\eta}$. These are the single-sample versions of what within the SPT collaboration are referred to as the weight matrix (Eq. 5.9) and the weighted map (Eq. 5.10), with the values of $1/n_i^2 = w_i$ being the detector weights discussed previously in Section 5.2.2.

Extending this solution to many detectors each with multiple time samples depends on

the structure of the noise covariance $\mathbf{N}$. In the case of white noise, as is produced by the TOD filtering steps detailed above, $\mathbf{N}$ is diagonal with entries equal to w_i, and therefore pixels in the full weighted map and their corresponding weight matrices are simply the sum of the contributions resulting from each sample falling within that pixel. If we use $P_{ti\alpha}$ to denote when detector i is pointing at pixel α at time t, we can write each pixel of the weighted maps as

$$\begin{aligned} \hat{T}^W_\alpha &= \sum_i \sum_t P_{ti\alpha} w_{ti} d_{ti} \\ \hat{Q}^W_\alpha &= \sum_i \sum_t P_{ti\alpha} w_{ti} \gamma_i c_i d_{ti} \\ \hat{U}^W_\alpha &= \sum_i \sum_t P_{ti\alpha} w_{ti} \gamma_i s_i d_{ti} \end{aligned} , \tag{5.11}$$

and the weight matrix corresponding to each pixel as

$$\mathbf{W}_\alpha = \sum_i \sum_t P_{ti\alpha} w_{ti} \begin{pmatrix} 1 & \gamma_i c_i & \gamma_i s_i \\ - & \gamma_i^2 c_i^2 & \gamma_i^2 c_i s_i \\ - & - & \gamma_i^2 s_i^2 \end{pmatrix} . \tag{5.12}$$

I have included the subscript t on the detector weights to indicate that in general a detector will have a different weight during separate scans of the telescope, even if those scans cover the same pixels. In principle the polarization angle ψ_i could also be a function of time, but given our scan strategy it is effectively fixed for each detector. The unweighted estimate of $\hat{\mathbf{m}} = \begin{pmatrix} \hat{T} \\ \hat{Q} \\ \hat{U} \end{pmatrix}$ can now be recovered by inverting the 3×3 weight matrix at each pixel and applying it to the weighted map:

$$\begin{pmatrix} \hat{T}_\alpha \\ \hat{Q}_\alpha \\ \hat{U}_\alpha \end{pmatrix} = {\mathbf{W}_\alpha}^{-1} \begin{pmatrix} \hat{T}^W_\alpha \\ \hat{Q}^W_\alpha \\ \hat{U}^W_\alpha \end{pmatrix} . \tag{5.13}$$

As a practical aside, we do not store the weight matrix $\mathbf{W}$ as $N_{\rm pix}$ 3×3 matrices, but instead collect the six unique entries from each 3×3 matrix into six $N_{\rm pix}$-long vectors organized as in Eq. 5.14. Likewise, when interacting with a weighted map of $N_{\rm pix}$ pixels we do not handle one $3N_{\rm pix}$-long vector, but rather three separate $N_{\rm pix}$-long vectors corresponding to $\hat{T}^W$, $\hat{Q}^W$, and $\hat{U}^W$. This independence may be misleading, however, as all three weighted maps must be used along with $\mathbf{W}$ to produce an unweighted map.

$$\mathbf{W} = \begin{pmatrix} W_{TT} & W_{TQ} & W_{TU} \\ - & W_{QQ} & W_{QU} \\ - & - & W_{UU} \end{pmatrix} . \tag{5.14}$$

5.4 Final Maps

A total of 562 observations are used in this analysis, distributed among subfields as shown in Table 5.2. The number of observations per subfield varies to equalize the noise across the field, with the highest-elevation subfield, ra0hdec-67.25, covering the smallest area of sky and having the fewest observations, and the lowest-elevation subfield, ra0hdec-44.75, covering the largest area of sky and having the most observations. The full-season coadded

Field	# Obs.
ra0hdec-44.75	169
ra0hdec-52.25	150
ra0hdec-59.75	141
ra0hdec-67.25	102

Table 5.2: Number of observations of each subfield used in this analysis.

maps of T, Q, and U for 150 GHz are shown in Figure 5.9. The cross-hatched patterns in Q and U are indicative of measuring E-modes at high signal-to-noise. The real-space E-mode polarization map itself is shown in Figure 5.10. The noise level (or depth) of the coadded map is measured by differencing two half-depth coadded maps and calculating the power spectrum of the result, correcting for the transfer function effects of the filtering described

above. The map depths as a function of multipole ℓ for both temperature and polarization data are shown in Figure 5.11; averaged over the range $1000 < \ell < 2000$, the polarized map depths at 95, 150, 220 GHz are 29.6, 21.2, and 75 μK-arcmin, respectively.

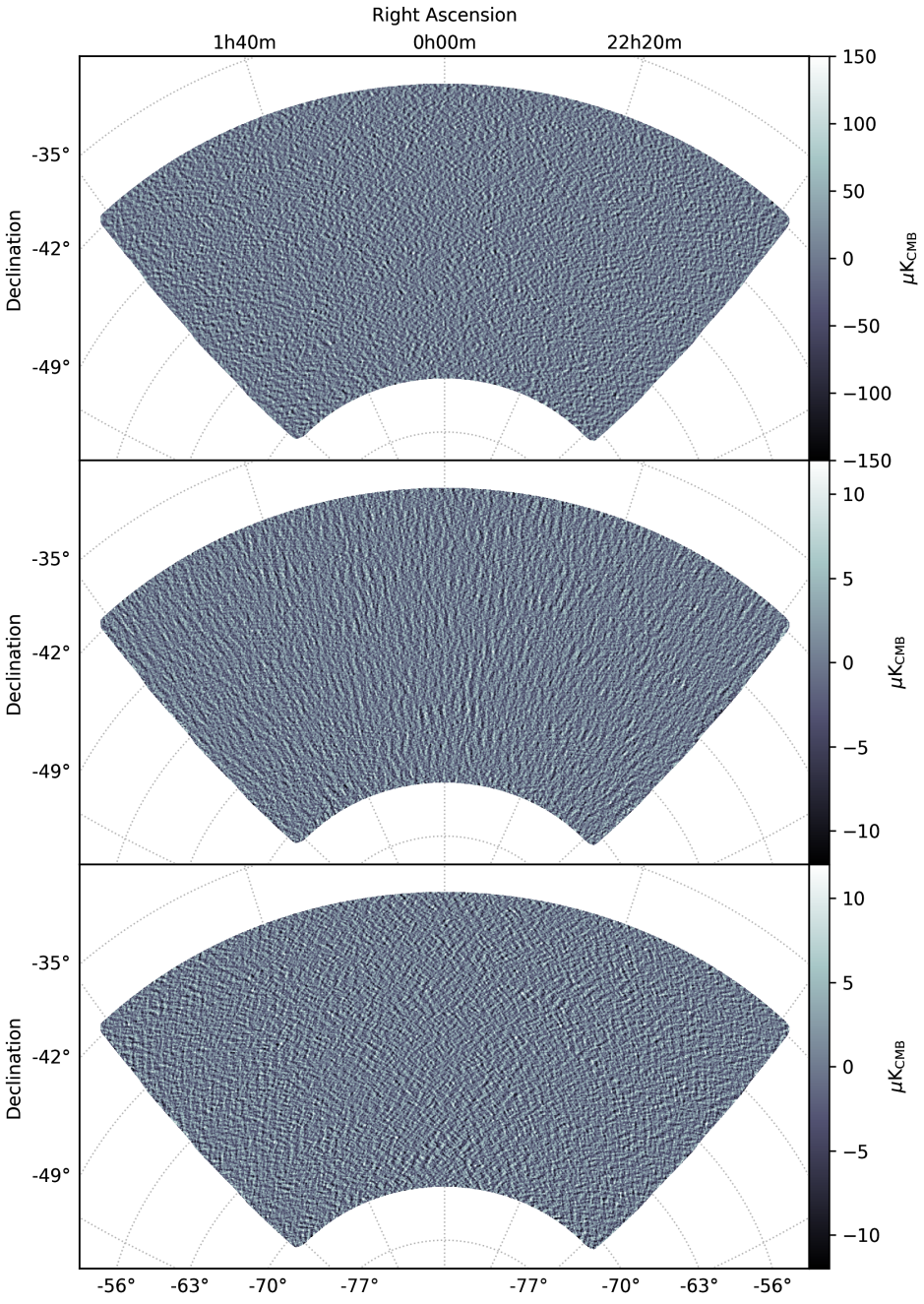

Figure 5.9: SPT-3G 2018 150 GHz temperature *(top)*, Stokes Q *(middle)*, and Stokes U *(bottom)* maps. Note the factor of ten difference in color scale between temperature and polarization maps. The data have been filtered to remove features larger than $\sim 0.5°$, and the polarization maps have been smoothed by a $6'$ FWHM Gaussian.

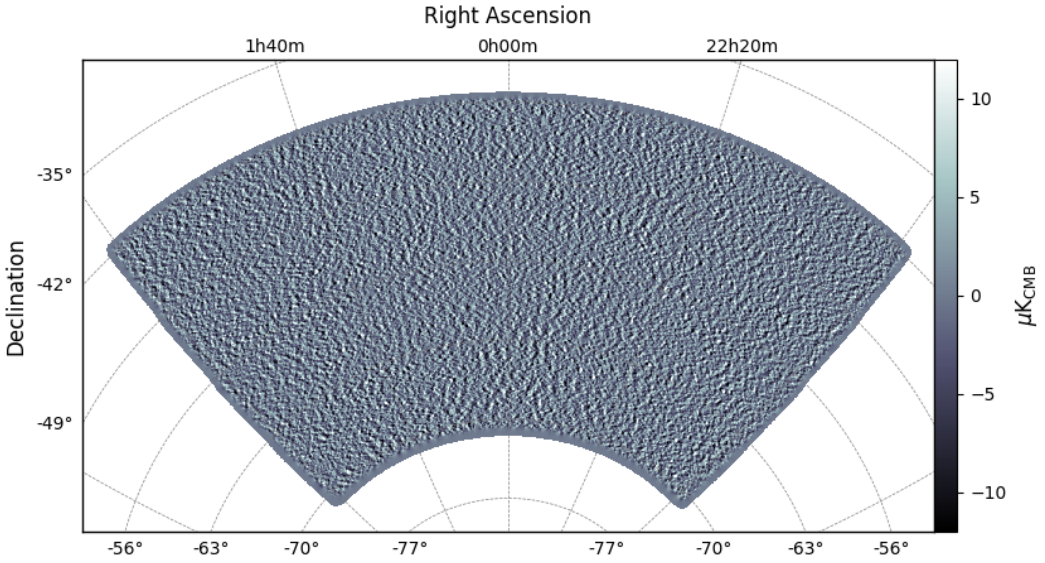

Figure 5.10: SPT-3G 2018 150 GHz E-mode polarization map. The data have been filtered to remove features larger than $\sim 0.5°$, and map has been smoothed by a $6'$ FWHM Gaussian.

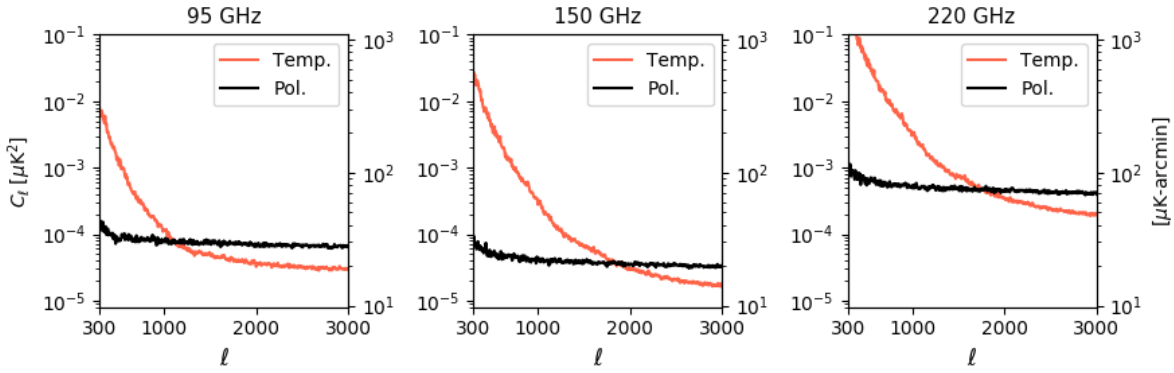

Figure 5.11: Temperature and polarization noise power spectra for the SPT-3G 1500 deg^2 field from the 2018 observing season. In each subplot, the left-hand vertical axis displays the noise in units of μK^2, while the right-hand vertical axis displays the equivalent map depth in units of μK-arcmin.

CHAPTER 6

POWER SPECTRUM ANALYSIS

In this chapter, I discuss the method to utilize the data collected as detailed in Chapter 5 to produce a measurement of the CMB *EE* and *TE* power spectra. Final results are presented in the Chapter 7. Following prior SPT analyses, I employ the pseudo-C_ℓ method to compute binned power spectrum estimates ("bandpowers") and use the cross-spectrum based approach of Tristram et al. (2005) and Polenta et al. (2005) to eliminate noise bias, computing all power spectra in the flat-sky approximation.

6.1 Flat-Sky Approximation

As the CMB is a function defined on the sphere, it can be accurately described in terms of spherical harmonics; however, over a small patch of sky the effects of curvature are negligible, and we can approximate the area using a flat tangent plane. This flat-sky approximation permits us to avoid computationally expensive spherical harmonic transforms in favor of simpler and faster discrete Fourier transforms. We relate the Fourier wave numbers (k_x, k_y) to angular multipole via $|\mathbf{k}| = \ell$ and denote the Fourier transform of quantities with the subscript ℓ.

The flat-sky approximation and corresponding map projection introduce a complication for the computation of polarization power spectra, as polarization angles on the sky are defined with respect to North, while the two-dimensional Fourier transform is performed along a Cartesian grid. In the chosen Lambert azimuthal equal-area projection, North is aligned with the vertical at the center of the map, but deflects away toward the map edges. To account for this, we apply the following polarization angle rotation in order to obtain the

flat-sky maps Q', U':

$$\begin{aligned} Q' &= Q\cos(2\psi_\alpha) + U\sin(2\psi_\alpha) \\ U' &= -Q\sin(2\psi_\alpha) + U\cos(2\psi_\alpha) \ , \end{aligned} \tag{6.1}$$

where Q, U are defined on the curved sky, and ψ_α is the angle measured from the vertical axis to North for pixel α defined by the map projection. This rotation may also be written in the more compact notation $(Q' + iU') = e^{-2i\psi_\alpha}(Q + iU)$. The Fourier transforms of the rotated Q' and U' maps are then used to construct the Fourier-space E-mode map via (Zaldarriaga 2001)

$$E_{\boldsymbol{\ell}} = Q'_{\boldsymbol{\ell}}\cos 2\phi_{\boldsymbol{\ell}} + U'_{\boldsymbol{\ell}}\sin 2\phi_{\boldsymbol{\ell}} \ , \tag{6.2}$$

where $\boldsymbol{\ell} = (\ell_x, \ell_y)$ and $\phi_{\boldsymbol{\ell}} = \arctan(-\ell_x/\ell_y)$.

6.2 Cross-Spectra

The full-depth maps shown at the end of the previous chapter contain both signal and noise, so the autospectrum of one map, $\mathrm{Re}\left[|m_\ell|^2\right]$, will be biased by the noise within that map. This noise bias can be avoided by using the cross-spectra of independent subsets of the data; over many cross-spectra, the uncorrelated noise averages out, while the recovered signal approaches the sensitivity of the full-depth autospectrum.

From the 562 subfield observations used in this analysis, I construct such subsets of partial-depth coadded maps, or "bundles", as follows. For each subfield, observations are coadded chronologically until the combined weight approaches $1/(N_{\mathrm{bundles}})^{\mathrm{th}}$ of the subfield weight in the full-season coadd. These subfield coadds are then combined to create one full-field bundle. This approach assures each bundle has approximately equal weight and even coverage of the field, to the extent allowed by the relatively small number of observations. In principle, the bundles can be defined separately for each frequency band, though for this analysis I chose to define all bundles based on 150 GHz data to simplify bookkeeping. I

chose $N_{\rm bundles} = 30$ bundles as the best compromise between total number of bundles and uniformity across the bundles, typically requiring 3–5 observations from each subfield. These map bundles are then used as the basic inputs to the rest of the analysis.

I compute the bundle cross-spectra by first multiplying each map $\mathbf{m}_A^{X,\nu_i}$ by an apodization mask, where $X \in \{T, E\}$, A indexes bundle number, and i indexes the frequency band. I then compute pairs of cross-spectra via

$$\tilde{D}_b^{XY,\ \nu_i\times\nu_j} = \frac{1}{N_b}\sum_{\ell\in b}\frac{\ell(\ell+1)}{2\pi}\mathrm{Re}\left[m_{\ell,A}^{(X,\nu_i)}m_{\ell,B}^{(Y,\nu_j)*}\right] \ , \tag{6.3}$$

for all bundles $A \neq B$, where N_b is the number of modes within each ℓ-bin b. The average of all cross-spectra for each spectrum and frequency band is then used for obtaining the final bandpowers. As is customary, here I report power spectra using the flattened spectrum, defined as

$$D_\ell \equiv \frac{\ell(\ell+1)}{2\pi}C_\ell. \tag{6.4}$$

6.3 Pseudo-C_ℓs

When estimating power spectra, I follow the MASTER algorithm (Hivon et al. 2002, hereafter H02), summarized here. The power spectra of maps constructed as described in the previous chapter yield estimates of the true C_ℓ that have been biased by various TOD- and map-level processing. The ensemble averages of these biased or pseudo-C_ℓ, denoted $\tilde{C}_\ell$, and the on-sky C_ℓ are related via

$$\langle\tilde{C}_\ell\rangle = \sum_{\ell'} M_{\ell\ell'}F_{\ell'}B_{\ell'}^2\langle C_{\ell'}\rangle \ , \tag{6.5}$$

in which B_ℓ includes the effects of the instrument beam and map pixelization, F_ℓ is a transfer function reflecting the effects of TOD filtering, and $M_{\ell\ell'}$ is a matrix describing the mixing of power that results from incomplete sky coverage. Rather than reporting individual ℓ-modes, we typically bin the data within ℓ-bins b of $\Delta\ell \geq 50$ and report the resulting bandpowers

C_b. Following H02, I introduce the binning operator $P_{b\ell}$ and its inverse operation $Q_{\ell b}$: if we write the binned equivalent of Eq. 6.5 utilizing the shorthand $K_{\ell\ell'} \equiv M_{\ell\ell'} F_{\ell'} B^2_{\ell'}$ and $K_{bb'} \equiv P_{b\ell} K_{\ell\ell'} Q_{\ell' b'}$, then an unbiased estimator of the true power spectrum can be calculated from the pseudo spectra via

$$\widehat{C_b} = K^{-1}_{bb'} P_{b'\ell'} \tilde{C}_\ell \ . \tag{6.6}$$

To compare the unbinned theory $C^{\rm th}_\ell$ to our bandpowers, we compute the binned theory spectra as $C^{\rm th}_b = W_{b\ell} C^{\rm th}_\ell$, where $W_{b\ell}$ are the bandpower window functions defined as

$$W_{b\ell} = K^{-1}_{bb'} P_{b'\ell'} K_{\ell'\ell} \ . \tag{6.7}$$

In the remainder of this section, I discuss the determination of the other terms in the right-hand side of Eq. 6.5.

6.3.1 Beam

The instrument beam (or point spread function) is the instrument's response to a point source on the sky. Maps produced from telescope data are a convolution of this beam and the real underlying sky, or equivalently a multiplication in Fourier space by the beam window function B_ℓ.

We measure the instrument beam with a combination of planet observations and the brightest point sources in subfield observations. Five dedicated observations of Mars during 2018 provide measurements of the beam at scales larger than $2'$–$5'$, while coadded point sources maps probe the beam's inner structure. The point source-derived beam also includes pointing jitter—the small fluctuations in telescope pointing due to limited accuracy of the telescope pointing model—which for 2018 data is approximately 12" rms. The Mars observations and point source maps are stitched together by convolving the Mars maps with the pointing jitter, convolving the point source maps by the planet disk, and fitting for a relative offset and scaling. The Fourier transform of the resulting beam map is then azimuthally av-

eraged and corrected for the planet disk and pixel window functions, yielding the B_ℓ shown in Figure 6.1. Uncertainties and correlations between B_ℓ at different ℓ values are established by utilizing different combinations of point sources and Mars observations while varying the parameters used to stitch the two types of map together. The beam covariance is then added to the bandpower covariance matrix, discussed in Section 6.7.

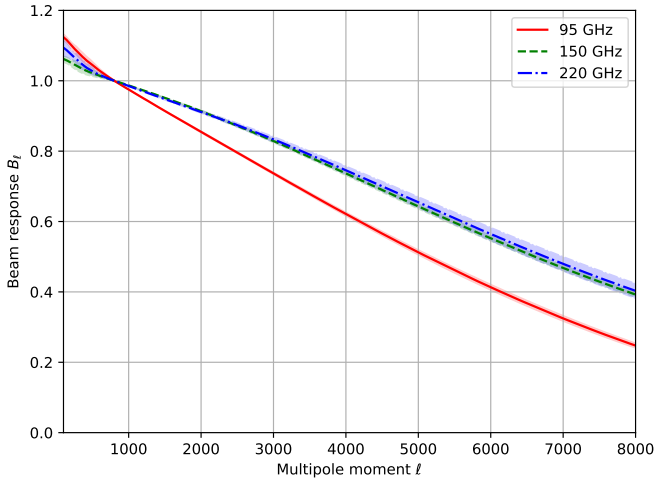

Figure 6.1: One-dimensional frequency-space representation of the measured instrument beam, B_ℓ, with uncertainties indicated by the shaded regions. The data are normalized to unity at $\ell = 800$.

6.3.2 Apodization Mask and Mode-Coupling

Prior to computing their Fourier transforms, I multiply the maps by a window function to smoothly roll-off the map edges to zero and remove excess power from bright point sources. I refer to this combined window function and point source mask as the apodization mask.

I generate the apodization mask in much the same manner as in Henning et al. (2018) (hereafter H18), using the same mask for all map bundles across all frequency bands. First, a binary mask is created for each bundle by smoothing the coadded bundle weights with a $5'$ Gaussian, then setting to zero any pixels with a weight below 30% of the median map weight. The intersection of all of these bundle masks is then edge-smoothed with a $30'$ cosine taper. Point sources detected above 50 mJy at 150 GHz are masked with a $5'$ radius disk (the

same size mask used during TOD processing), and the cutouts are edge-smoothed with a $10'$ cosine taper. The final mask is shown in Figure 6.2 and has an effective area of $1614\,\mathrm{deg}^2$, or 3.9% of the full sky.

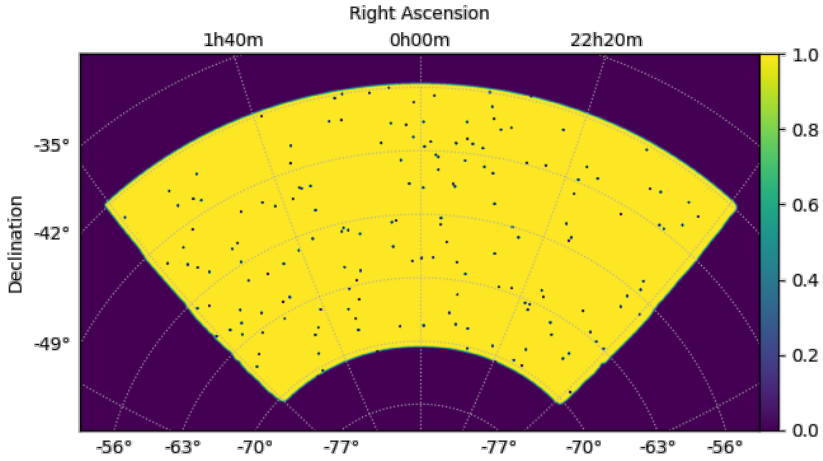

Figure 6.2: Apodization mask used in this analysis for the SPT-3G survey field.

Multiplications in real space correspond to convolutions in Fourier space, so applying this apodization mask to maps convolves their power spectrum with the power spectrum of the mask, coupling power between formerly independent ℓ-modes. This effect is encapsulated in the mode-coupling matrix $M_{\ell\ell'}$. Previous SPT analyses have used an analytic calculation of the mode-coupling matrix in the flat-sky regime, as derived in H02 for temperature and in the Appendix of Crites et al. (2015) (hereafter C15) for polarization. In H18 this calculation was further verified for input $0 < \ell < 500$ with the use of curved-sky HEALPix simulations. As the SPT-3G field is the largest field to-date that we have analyzed using the flat-sky approximation, it is important to test the validity of these calculations. While I found good agreement between the analytic flat-sky calculation and curved-sky simulations for my apodization mask, the resulting mode-coupling matrix did not properly account for mixed power in my measured power spectra.

As an alternate means of simulating the mode-coupling matrix, I first generate a set of HEALPix simulations with power in $\Delta\ell = 5$ bins in a manner similar to H18; however,

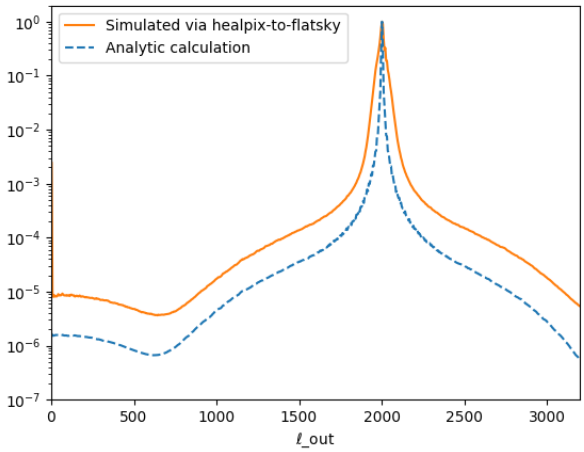

Figure 6.3: Slice of $M_{\ell\ell'}$ along ℓ'=2000 according to the analytic formula *(blue, dashed)* and curved-to-flat sky simulations *(orange, solid)*. The simulated result shows significantly more power coupled between multipoles.

instead of then using spherical harmonic transforms to compute the power spectrum, I reproject the HEALPix skies to our flat map projection before applying the apodization mask. I then calculate the power spectrum in the flat-sky approximation and measure how the input power has spread. This simulation method therefore includes not only the mode-mixing the effects of the mask, but also those caused by distortions from the the map projection. I build one full realization of the mode-coupling matrix using 640 individual simulations covering the range $0 < \ell < 3200$ in increments of $\Delta\ell = 5$, and I average 150 such realizations to obtain the final mode-coupling matrices $M_{\ell\ell'}^{XY}$. I find the matrices to be virtually identical between the power spectra, so I will omit the superscripts on $M_{\ell\ell'}$ from here on, though when computing bandpowers I do use the appropriate dedicated matrix. Figure 6.3 shows a slice of $M_{\ell\ell'}$ along input $\ell' = 2000$ computed with the analytic formula as well as this new simulation method. The simulated result captures significantly more mode-coupling that increases with ℓ, demonstrating the importance of projection effects on a patch of this size. I am nevertheless able to reconstruct the input power spectrum to simulations when using the $M_{\ell\ell'}$ constructed in this manner, so I proceed in the flat-sky limit with caution. The structure of the full $M_{\ell\ell'}$ is shown in Figure 6.4.

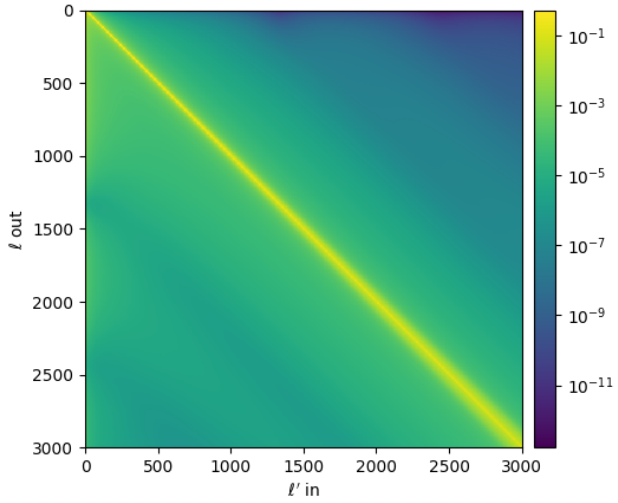

Figure 6.4: The simulated mode-coupling matrix.

6.3.3 Filter Transfer Function

The filter transfer function F_ℓ captures the effects of the filtering steps discussed in Section 5.2.2. As the majority of TOD filtering is anisotropic, being applied only along the telescope scan direction, the effects of filtering are more accurately dealt with a 2D transfer function, though we may approximate it as a 1D function by azimuthally averaging the ℓ_x, ℓ_y values. F_ℓ is obtained through simulations, the generation of which are discussed further in Section 6.4. In brief, a known input spectrum $C_\ell^{\rm th}$ is used to generate $\mathcal{O}(100\text{s})$ of sky realizations and simulated TOD, to which the same filtering steps as used on the real data are then applied. The output spectra are then compared to the input spectra to obtain the effects of TOD filtering.

Solving Eq. 6.5 for F_ℓ directly would necessitate inverting $M_{\ell\ell'}$, which may be ill-conditioned. Instead, I solve for F_ℓ using the iterative method prescribed in H02:

$$\begin{aligned} F_\ell^{(0)} &= \frac{\langle \tilde{C}_\ell^{\rm sim} \rangle}{w_2 B_\ell^2 C_\ell^{\rm th}} \ , \\ F_\ell^{(i+1)} &= F_\ell^{(i)} + \frac{\langle \tilde{C}_\ell^{\rm sim} \rangle - M_{\ell\ell'} F_\ell^{(i)} B_\ell^2 C_\ell^{\rm th}}{w_2 B_\ell^2 C_\ell^{\rm th}} \ , \end{aligned} \tag{6.8}$$

I find three iterations sufficient to achieve a stable result. The transfer functions for TT and EE for 150 GHz are shown in Figure 6.5, with similar results found for 95 GHz and 220 GHz. The difference between the EE and TT transfer functions arises from the common-mode filter, which removes large-scale power from temperature but not polarization. The iterative approach is unstable for the TE power spectrum on account of zero crossings, so I instead use the geometric mean of the TT and EE transfer functions, in the same manner as C15 and H18. Whereas a similar analysis for SPT-SZ (Lueker et al. 2010) further used the geometric mean of transfer functions for all cross-frequency power spectra, $F_\ell^{\nu_i \times \nu_j} = \sqrt{F_\ell^{\nu_i} F_\ell^{\nu_j}}$, here I instead calculate a dedicated transfer function for each $\nu_i \times \nu_j$ spectrum.

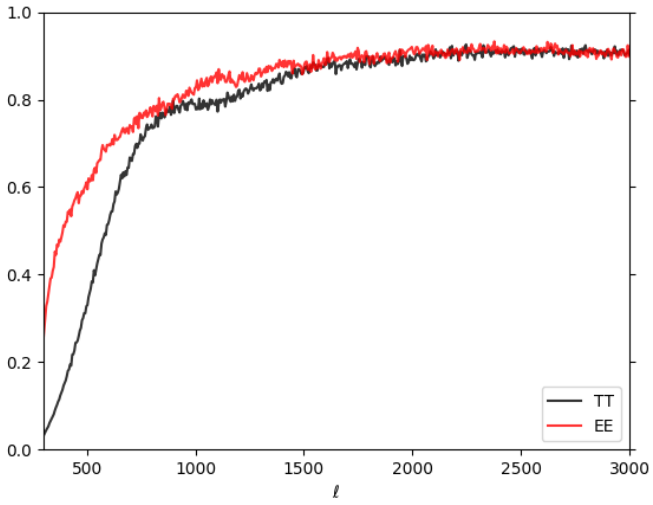

Figure 6.5: Filter transfer functions for TT and EE power spectra, computed using 250 simulations of the full SPT-3G 2018 dataset. The transfer functions differ as a result of the wafer-based common-mode filter, which removes large-scale power from temperature but not polarization.

6.4 Simulations and Mock-Observing

We rely on simulations to recover the effect of TOD filtering and map-level processing on the data. Sky realizations of the same underlying power spectrum are generated and convolved with the instrument beam; these noiseless mock skies are then used along with recorded

telescope pointing information from real observations to generate simulated detector TOD, which are then processed using the same detector cuts and filtering as in the actual observations. The resulting "mock observations" are then bundled and analyzed in exactly the same manner as the real data. I generate 250 such sky realizations, and mock-observe them using every subfield observation from 2018. As SPT-3G collects more data over the following years, this approach will quickly become untenable, and a smarter selection of mock observations will need to be done.

I generate the mock skies in the following manner. The CMB power spectra are generated with CAMB using parameters from the best-fit ΛCDM model to the BASE_PLIKHM_TTTEEE_LOWL_LOWE_LENSING *Planck* data set (Planck Collaboration et al. 2020b). Gaussian realizations of the output lensed C_ℓ are then generated in the HEALPix pixelization scheme. I include realizations of Gaussian foregrounds with power spectra as reported in George et al. (2015), with correlations between frequencies induced by utilizing the same random seed. I generate Poisson foregrounds with fluxes between 6.4 mJy and 50 mJy at 150 GHz using source population models from De Zotti et al. (2005) for radio galaxies and Béthermin et al. (2012) for dusty star-forming galaxies, with polarization fractions from Gupta et al. (2019) and flux-frequency scaling relations from Everett et al. (2020). Figure 6.6 shows the power spectrum of each of these components, as well as that of the CMB and the combined total. The foregrounds have negligible polarization power over the multipole range considered here, and the *TE* power for all foregrounds has been set to zero. These simulated components are added in frequency-space and multiplied by a Gaussian approximation of the SPT-3G beam with FWHMs of $1.7', 1.4', 1.2'$ at 95, 150, 220 GHz, respectively. The resulting mock skies are then masked down to the SPT-3G survey field and supplied to the mock-observing pipeline.

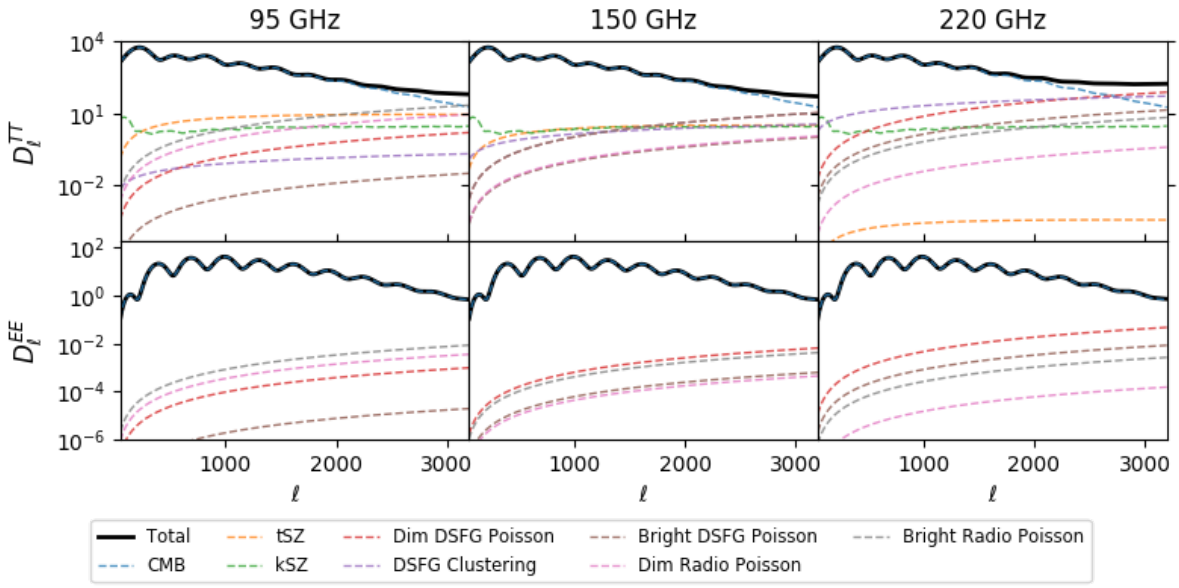

Figure 6.6: Power spectrum of each TT and EE component used in the simulated skies, in $\mu\mathrm{K}^2$. The polarized foregrounds are negligible over the range of multipoles considered in this analysis. The TE simulated skies, not shown, use only the CMB as input.

6.5 Map and Spectra Corrections

6.5.1 Absolute Calibration

The calibration process for detector TOD described in Section 5.1.1 is expected to be accurate within ∼several percent, requiring a final absolute temperature calibration for accurate bandpower values. Similarly, an overall polarization calibration is required, as SPT-3G maps are currently made with every detector assumed to have unity polarization efficiency, while in reality the polarization efficiency of the instrument can be degraded by a variety of factors, including crosstalk between polarization pairs and misidentification of detector resonances. We calculate the calibration factors via comparison to *Planck*, employing both map-based and power-spectrum-based approaches.

As SPT-3G uses two separate Galactic HII regions for TOD temperature calibration—RCW38 for the low-elevation subfields and MAT5a for the high-elevation subfields—we calculate and apply a separate calibration factor for each subfield before coadding maps from dif-

ferent subfields. The per-subfield temperature calibration is calculated via cross-correlation with *Planck* maps of the nearest frequency channel, using 100 GHz, 143 GHz, and 217 GHz for comparison to the SPT-3G maps at 95 GHz, 150 GHz, and 220 GHz, respectively. The *Planck* maps are mock-observed in the same manner as the SPT-3G simulations discussed in Section 6.4 with identical filtering steps. We then take the ratio of SPT-3G cross-spectra formed from half-depth maps to the cross-spectrum between a full-depth SPT-3G map and a full-depth Planck map, simplifying to

$$\frac{\tilde{D}_\ell^{SPT_1\times SPT_2}}{\tilde{D}_\ell^{SPT\times Planck}} = \frac{(\epsilon^T B_\ell^{SPT})^2}{\epsilon^T B_\ell^{SPT} B_\ell^{Planck}} \ , \tag{6.9}$$

where the filter transfer functions and mode-coupling have dropped out as a result of identical processing, and ϵ^T is the beam calibration factor required to make the ratio equal to unity after plugging in the published *Planck* beam and the SPT-3G beam as measured in Section 6.3.1. The uncertainty on this calibration is obtained by repeating the above procedure on simulated maps that have been convolved with the *Planck* beam and the Gaussian approximation of the SPT-3G beam, respectively, before being combined with noise realizations from the respective instruments and mock-observed. The resulting multiplicative map correction factors, corresponding to $1/\epsilon^T$, are shown in Table 6.1. We see that the required corrections are the same within uncertainties within each half of the field but generally differ from the other half of the field, consistent with the two Galactic HII calibration regions. All values are within the $\sim 10\%$ range of unity expected from the TOD calibration procedure.

	95 GHz	150 GHz	220 GHz
ra0hdec-44.75	1.04	1.01	0.97
ra0hdec-52.25	1.04	1.01	0.97
ra0hdec-59.75	0.99	0.93	0.96
ra0hdec-67.25	0.98	0.93	0.97

Table 6.1: Temperature map calibration factors for each subfield and frequency band. The uncertainty on each factor is within ± 0.01.

While the above calibration is expected to be accurate at the 1% level, it does not take into account covariances between the frequency bands. We therefore apply an additional spectrum-derived correction, $T_{\rm cal}$, calculated from a per-bandpower comparison to the full-sky *Planck* CMB-only temperature power spectrum (Planck Collaboration et al. 2020c) over the angular multipole range $300 \leq \ell \leq 1500$, with added foreground power from the best-fit model from Reichardt et al. (2020) and the population of radio galaxies according to the model of De Zotti et al. (2005). We compute the scaling factor necessary to minimize the chi-square between each set of auto-frequency TT spectra. Including the calibration uncertainty in *Planck* data, the uncertainty in this correction is expected to be $< 1\%$.

Unlike the temperature calibration, the polarization calibration is not expected to vary between subfields, and we compute the corresponding $E_{\rm cal}$ factor in the same manner as $T_{\rm cal}$ by directly comparing the *EE* bandpowers from full-field temperature-calibrated SPT-3G maps to the *Planck EE* power spectrum. We obtain the $E_{\rm cal}$ values and uncertainties shown in Table 6.2. We note that $E_{\rm cal}$ may be interpreted as the inverse of the effective polarization efficiency of the instrument, and the values here are of approximately the same magnitude as the polarization calibration factors found for SPTpol in C15 and H18.

95 GHz	150 GHz	220GHz
1.028 ± 0.009	1.057 ± 0.008	1.136 ± 0.016

Table 6.2: Polarization map calibration factors ($E_{\rm cal}$) for each frequency band.

6.5.2 T-to-P Leakage

Polarization data can be contaminated by leaked temperature signal, which can be caused by a variety of factors including mismatched gain between detectors in a polarization pair and differential beam shapes. As in C15 and H18, I perform a monopole deprojection, in which I subtract a scaled copy of the T map from the Q and U maps, though I differ in the manner in which I obtain the leakage coefficients. In both C15 and H18, the leakage

coefficients ϵ^P, where $P \in \{Q, U\}$, were calculated as

$$\epsilon^P = \sum_\ell \frac{C_\ell^{TP}}{C_\ell^{TT}} \tag{6.10}$$

for some range of ℓ, and the deprojected maps obtained via $P' = P - \epsilon^P T$. In this analysis, the $\ell_x > 300$ high-pass TOD filter removes modes in the 2D Fourier plane such that TQ is mostly a scaled, inverted copy of TE, which biases the fit defined above. Instead, I fit each of TQ and TU to a linear combination of TE and TT:

$$C_\ell^{TP} = \epsilon^{P,TT} C_\ell^{TT} + \epsilon^{P,TE} C_\ell^{TE} \tag{6.11}$$

where $P \in \{Q, U\}$. I then solve for the respective coefficients, with the $\epsilon^{P,TT}$ used for monopole deprojection in the usual fashion, while the $\epsilon^{P,TE}$ values are discarded.

I perform two tests of this method before applying it to data. First I ensure that the $\epsilon^{P,TT}$ coefficients are consistent with zero in noiseless mock observations. I then inject T-to-P leakage in the simulations to verify I can recover the injected signal. After passing both of these checks, I calculate the leakage coefficients from real data and obtain the values in Table 6.3. I neglect the error on the monopole leakage terms, as the shift in bandpowers due to the deprojection is negligible within the reported uncertainties.

	95 GHz	150 GHz	220GHz
$\epsilon^{Q,TT}$	0.006 ± 0.002	0.005 ± 0.002	0.008 ± 0.010
$\epsilon^{U,TT}$	0.008 ± 0.002	0.013 ± 0.002	0.015 ± 0.010

Table 6.3: T-to-P monopole leakage coefficients

Another form of T-to-P leakage results from the CM filter. Here I have not enforced explicit pair-differencing when making maps, resulting in unpaired detectors entering the polarization maps. Empirically the CM filter reduces polarization noise, which could only occur through such unpaired detectors; however, these same detectors also cause the CM

filter to directly inject some fraction of the $\ell \sim 500$ temperature power into the polarization maps. To quantify this leakage, I mock-observe a set of T-only simulations and record the power leaked into EE and TE, with the results shown in Figure 6.7. The leakage depends on the particular configuration of detectors used to form the CM, and evidently differs in sign and magnitude across the three frequency bands.

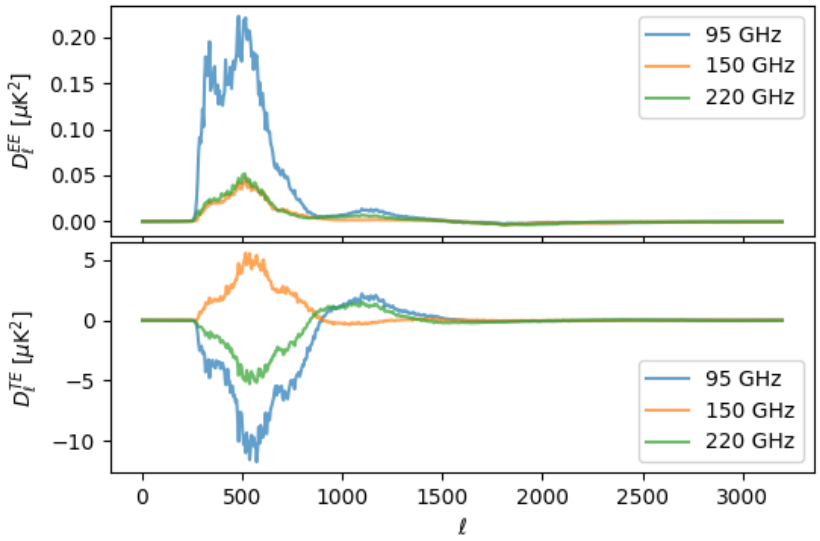

Figure 6.7: Power leaked into *EE (top)* and *TE (bottom)* from processing T-only input maps. This leakage is due to detectors without a polarization partner entering the common-mode filter, and the shape of the leakage depends on the particular configuration of detectors used to form the common-mode for each frequency band.

This CM filter-induced T-to-P leakage is also present in the simulations used to obtain the filter transfer function. Although F_ℓ is a multiplicative correction, and this T-to-P is an additive bias, to first order F_ℓ already removes this leakage: when reconstructing the input $D_{\ell,\mathrm{th}}^{EE}$ from simulated $\tilde{D}_\ell^{EE}$ using Eq. 6.5, no residual bias is seen. As will be discussed in Section 6.6, realistic changes to the input spectra used for the sims do not significantly affect F_ℓ, so this bias will already be reduced to a negligible level for EE data.

The leakage in TE is not handled so easily, however, as F_ℓ^{TE} is not constructed specifically from TE spectra, but rather as the geometric mean of F_ℓ^{TT} and F_ℓ^{EE}. When reconstructing the input $D_{\ell,\mathrm{th}}^{TE}$ from simulated $\tilde{D}_\ell^{TE}$ using Eq. 6.5, a residual bias remains. I use the same set

of sims for obtaining F_ℓ to calculate the following residual TE bias, which is then subtracted from the data:

$$TE_{\rm bias} = \tilde{D}^{TE}_{\ell,sim} - \sum_{\ell'} M_{\ell\ell'} F^{TE}_{\ell'} B^2_{\ell'} D^{TE}_{\ell,{\rm th}} \ . \tag{6.12}$$

In addition to the check against varying input sim spectra discussed below, I also mock-observe T-only *Planck* maps over the SPT-3G patch to verify the leakage bias in TE I expect from the real sky. I find excellent agreement with the result from my standard set of sims, and so am confident the TE bias removal works as intended.

6.6 Tests for Systematic Error

I perform two primary tests on the data and analysis pipeline, the first using null tests to probe for systematic effects in the data, and the second verifying the robustness of the pseudo-spectrum debiasing pipeline against changes to the input power spectrum.

6.6.1 Null Tests

To check that the data are free of systematics (or at least affected by systematics at a level below the current noise level), I perform a series of null tests, in which the data is divided based on a possible systematic, and the groups of data are then differenced to form a collection of null maps. The cross spectra of the null maps are then compared to the expected null spectrum if that systematic were absent. The expected null spectra are typically consistent with zero, although factors such as differing live detector counts can cause non-zero expectation spectra. The same noiseless mock observations used for calculating F_ℓ and detailed in Section 6.4 are used to calculate the expectation spectra. I perform the following null tests, most of which have also been used by prior SPT analyses:

1. Azimuth : this orders the data based on the average azimuth of the observation, and is designed to detect ground-pickup.

2. First-Second : this orders the data chronologically, and is designed to test for long time-scale drifts. For 2018, this test is degenerate with splitting the data based on if the Sun was below or above the horizon, another possible source of contamination.

3. Left-Right : this divides each observation into left-going scans and right-going scans and is intended to test for differences based on telescope movement.

4. Moon up - Moon down : this divides the data based on whether the Moon was above or below the horizon, and is intended to test for contamination from the beam side lobes.

5. Saturation : this orders the data based on the average number of detectors flagged as Saturated during an observation, as this could indicate decreased responsivity in the array as a whole.

6. Wafer : this divides the data based on detector wafer. As wafers with a variety of properties are installed in the focal plane, there may be differences in their measured signal. I divide the wafers in to two groups based on their optical response to the calibrator, a split that is largely degenerate with many detector properties, notably $P_{\rm sat}$.

With the exception of the Azimuth test, the null tests use the same chronological bundles as the power spectrum estimation. For the Left-Right test, each bundle is separated into left-going and right-going scans, and these are differenced to create the null maps. An analogous procedure is used for the Wafer null test. For the First-Second, Moon Up-Moon Down, and Saturation tests, each observation is assigned a value based on the susceptibility of that observation to the potential systematic, and the bundles are then rank-ordered by the average of this value across their constituent observations. The null maps are then formed by subtracting the halves of the rank-ordered list so as to maximize the effect of the systematic in the cross-spectra between null maps. For the Azimuth test, the normal

chronological bundles include too wide a range of azimuth, such that any potential effect would be washed out. I therefore re-bundle based on azimuth, ordering observations by the separation between their mean azimuth and the azimuth corresponding to the Dark Sector Laboratory, the building connected to the telescope that we expect to be the dominant source of any ground-based pickup.

For each null test, I use the average and distribution of all null cross-spectra to compute the χ^2 compared to the null expectation spectrum, and I then compute the probability to exceed (PTE) this χ^2 value. An exceedingly low PTE or a preponderance of low PTEs indicate the data are in larger disagreement with expectation than random chance would allow. I perform three tests on the collection of PTEs: (1) the entire table of PTE values is consistent with a uniform distribution between 0 and 1 with a Kolmogorov-Smirnov (KS) test p-value > 0.05 (2) Individual PTE values are larger than $0.05/N_{\rm tests}$ (3) The combination of PTEs within each row using Fisher's method has a PTE above $0.05/N_{\rm rows}$. These tests and significance thresholds were agreed upon before looking at the collection of final PTEs to avoid confirmation bias.

	95 GHz		150 GHz		220 GHz		Row Fisher
	TE	*EE*	*TE*	*EE*	*TE*	*EE*	PTE
Azimuth	0.5974	0.4939	0.1969	0.0054	0.9023	0.8598	0.1636
$1^{\rm st} - 2^{\rm nd}$	0.3131	0.6800	0.2594	0.9825	0.6745	0.4779	0.7779
Left-Right	0.3207	0.2285	0.6895	0.6761	0.3906	0.5617	0.6346
Moon Up-Down	0.8127	0.9954	0.7333	0.4974	0.9175	0.7619	0.9943
Saturation	0.0962	0.8606	0.1186	0.4727	0.6097	0.4083	0.3320
Wafer	0.1091	0.0038	0.4806	0.0432	0.6597	0.5993	0.0140

Table 6.4: PTEs for individual null tests and the PTE for each test combined across frequencies and spectra using Fisher's method.

The null test PTEs are collected in Table 6.4. The distribution of PTEs is consistent with a uniform distribution with a KS test p-value of 0.76, and with 36 tests and six rows, the individual PTE threshold is 0.0014, and the row threshold is 0.0083; while the Azimuth test for 150 GHz *EE* and Wafer test for 95 GHz *EE* are marginal, all of the tests pass the agreed-upon criteria. As data from SPT-3G becomes more sensitive, such tests will bear

closer inspection, but for the purposes of this analysis I conclude the listed systematics do not affect the data in a statistically significant way.

6.6.2 Dependence on Input Cosmology

Any corrections to the data based on simulations, such as F_ℓ, or additive bias corrections, should be robust against the chosen input cosmology to the sims. At the same time, the CMB has been measured with extraordinary precision, and our pipeline does not necessarily need to be able to accurately recover a cosmology that is 100σ discrepant from our universe. The chosen input to the sims in Section 6.4 was selected to match the true sky as closely as possible, so we can be fairly confident that the resulting sims will yield valid results.

To test that the pipeline is stable against small variations to the input power spectra, I make an additional set of sims with a contrived cosmology chosen to be $\sim 5\sigma$ discrepant with the results found in H18, with the specific parameter values $\Omega_b h^2 = 0.02$, $\Omega_c h^2 = 0.14$, $H_0 = 61\,\mathrm{km\ s^{-1}Mpc^{-1}}$, $\ln(10^{10}A_s) = 3.12$, $n_s = 0.9$, and $\tau = 0.06$. Additionally, the foreground power is doubled in comparison to the standard set of simulations. I mock-observe 50 realizations of this cosmology and debias the resulting $\tilde{C}_\ell$ using the transfer function and *TE* bias corrections as derived from the standard set of sims. The input spectra are recovered to well within the stated bandpower uncertainties, and I therefore find no measurable bias due to F_ℓ or the TE_{bias} correction.

6.7 Bandpower Covariance Matrix

The bandpower covariance matrix $\mathbf{C}_{bb'}$ captures the uncertainty in individual bandpowers and their correlations as well as the correlations between different spectra and different frequency bands. $\mathbf{C}_{bb'}$ includes contributions from noise and sample variance: we estimate the noise variance from the set of measured cross-spectra, and the sample variance from the set of 250 signal-only simulations.

The calculation of the covariance matrix follows the general procedure outlined in the Appendix of Lueker et al. (2010), including conditioning of the covariance matrix to reduce noise in the off-diagonal elements. The estimate of the covariance is noisy, given the finite number of simulations and observations; however, we expect elements far away from the diagonal to be zero on average, given the shape of the mode-coupling due to the apodization mask. We replace elements in the estimated covariance matrix $\widehat{\mathbf{C}}_{bb'}$ the same distance away from the diagonal with their mean:

$$\mathbf{C}_{bb'} = \frac{\sum_{b_1-b_2=b-b'} \frac{\widehat{\mathbf{C}}_{b_1 b_2}}{\sqrt{\widehat{\mathbf{C}}_{b_1 b_1}\widehat{\mathbf{C}}_{b_2 b_2}}}}{\sum_{b_1-b_2=b-b'} 1} \,. \tag{6.13}$$

The same conditioning procedure was also applied in C15 and H18. For the diagonal elements, we expect a fractional uncertainty of $\sqrt{2/n_{\rm obs}}$; for the 30 data bundles in this analysis, this is 26%. We therefore apply an additional conditioning step on the diagonal, in which we preserve the sample variance from signal-only sims while smoothing the noise spectrum derived from the measured cross-spectra. We then assemble the diagonal of the covariance analytically given the expectation values in Zaldarriaga & Seljak (1997), extracting the prefactor (effective number of modes) from the signal-only sims. The three frequency bands are used to form three auto-frequency spectra and three cross-frequency spectra for both *EE* and *TE*, giving the covariance matrix a 12×12 block structure. The full conditioned bandpower covariance matrix is shown in Figure 6.8.

The uncertainty in the beam calculation discussed in Section 6.3.1 is included as an additional covariance using the procedure laid out in Keisler et al. (2011) and C15. We first construct a "beam correlation matrix"

$$\rho^{\rm beam}_{bb'} = \left(\frac{\delta D_i}{D_i}\right)\left(\frac{\delta D_j}{D_j}\right), \tag{6.14}$$

where

$$\frac{\delta D_i}{D_i} = 1 - \left(1 + \frac{\delta B_i}{B_i}\right)^{-2} \tag{6.15}$$

is the effect of the beam uncertainty δB_i on the power spectrum. We convert the beam correlation matrix to a covariance matrix using the *TE* or *EE* bandpowers D_i via

$$\mathbf{C}^{\text{beam}}_{bb'} = \rho^{\text{beam}}_{bb'} D_i D_j. \tag{6.16}$$

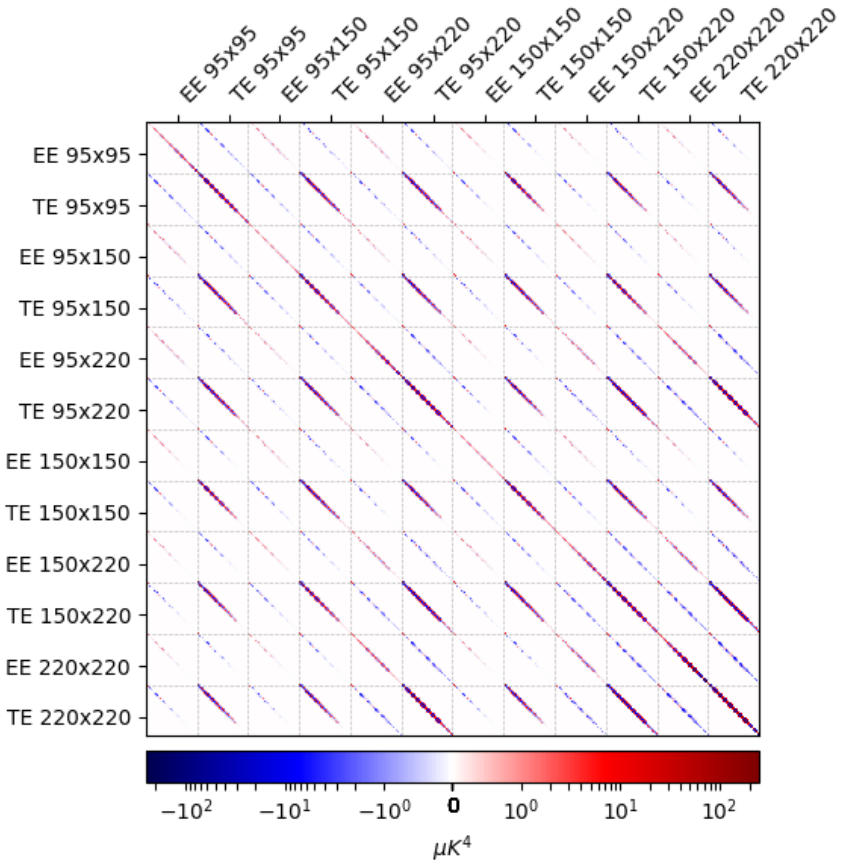

Figure 6.8: Bandpower covariance matrix showing the uncertainties and correlations for auto- and cross-frequency *EE* and *TE* bandpowers. A grid has been overlaid to highlight the 12×12 block structure of the matrix.

CHAPTER 7

RESULTS

7.1 EE and TE Bandpowers

I present bandpowers and uncertainties for the *EE* and *TE* power spectra measured using each frequency combination of 95, 150, and 220 GHz data in Table 7.1 and Table 7.2, respectively. The full set of bandpowers is plotted in Figure 7.1. The bandpowers span the multipole range $300 \leq \ell < 3000$, with bin widths of $\Delta\ell = 50$ for $\ell < 2000$ and $\Delta\ell = 100$ for $\ell > 2000$. With 150×150 GHz alone, I measure the first seven acoustic peaks of the *EE* spectrum with signal-to-noise ≥ 6.4 on each bandpower and 3–4 bandpowers per peak. The uncertainties in the bandpowers are dominated by sample variance at $\ell < 1275$ for *EE* and $\ell < 1425$ for *TE*.

The uncertainties can be reduced further by combining the six measurements for each power spectrum into one set of minimum-variance (MV) bandpower measurements with a generalized least-squares fit, in the same manner as used for SPT-SZ (Mocanu et al. 2019) with the simplifying assumption that the polarized foreground power is negligible within the bandpower uncertainties, and therefore no foreground modeling or removal is required. This assumption will be tested by a consistency check between the MV bandpowers and the multifrequency data.

To construct the MV bandpowers $\bar{D}$, the complete set of multifrequency bandpowers are first concatenated into one 528-element vector D in the ordering prescribed by the covariance matrix $\mathbf{C}$ as constructed in Section 6.7. I then construct a 528×88 design matrix $\mathbf{X}$ in which each column is equal to one in the six elements corresponding to a power spectrum measurement in that ℓ-space bin and zero elsewhere. The MV bandpowers are then given by

$$\bar{D} = (\mathbf{X}^\intercal \mathbf{C}^{-1} \mathbf{X})^{-1} \mathbf{X}^\intercal \mathbf{C}^{-1} D \ . \tag{7.1}$$

ℓ Range	$\ell_{\rm eff}$	90×90 GHz		90×150 GHz		90×220 GHz		150×150 GHz		150×220 GHz		220×220 GHz	
		D_ℓ	σ	D_ℓ	σ	D_ℓ	σ	D_ℓ	σ	D_ℓ	σ	D_ℓ	σ
300 – 349	325	13.1	1.1	12.8	1.1	12.1	1.3	13.2	1.1	12.7	1.3	12.1	2.0
350 – 399	375	19.7	1.3	20.5	1.3	19.0	1.5	21.1	1.3	19.9	1.5	18.0	2.3
400 – 449	425	19.0	1.2	18.8	1.1	17.9	1.3	19.1	1.1	18.4	1.3	17.7	2.1
450 – 499	475	11.2	0.7	12.0	0.7	11.1	0.9	12.5	0.7	11.1	0.9	9.4	1.7
500 – 549	524	7.1	0.5	7.3	0.4	7.6	0.7	7.0	0.4	8.3	0.6	9.4	1.6
550 – 599	575	11.1	0.7	11.3	0.6	12.2	0.9	11.8	0.7	11.8	0.9	11.5	1.9
600 – 649	624	29.0	1.3	29.4	1.2	29.1	1.5	30.1	1.2	29.8	1.4	34.3	2.6
650 – 699	674	39.0	1.5	39.1	1.3	39.5	1.7	38.9	1.4	39.7	1.7	40.9	2.9
700 – 749	725	33.6	1.4	34.4	1.3	33.1	1.7	35.0	1.3	34.1	1.6	32.4	3.0
750 – 799	774	21.2	1.1	20.8	0.9	22.0	1.3	20.4	0.9	21.3	1.2	22.8	2.7
800 – 849	824	13.2	0.8	13.3	0.6	13.2	1.0	13.7	0.6	13.4	0.9	13.6	2.6
850 – 899	874	16.9	0.9	17.2	0.7	17.8	1.2	17.0	0.8	17.7	1.1	19.1	2.9
900 – 949	924	31.8	1.3	31.4	1.1	30.8	1.7	31.6	1.1	32.3	1.6	29.6	3.5
950 – 999	974	41.2	1.6	40.4	1.4	40.7	2.0	40.7	1.4	39.9	1.9	36.9	4.0
1000 – 1049	1024	39.4	1.6	38.4	1.3	39.3	2.0	38.5	1.4	37.3	1.9	40.7	4.2
1050 – 1099	1075	26.1	1.3	26.3	1.0	24.9	1.7	26.4	1.1	25.3	1.6	20.4	4.0
1100 – 1149	1124	15.5	1.0	15.2	0.7	14.6	1.4	15.0	0.7	13.9	1.2	10.7	3.9
1150 – 1199	1174	13.1	1.0	12.3	0.7	10.8	1.5	12.6	0.7	12.1	1.2	12.6	4.1
1200 – 1249	1224	20.6	1.3	21.8	0.9	23.9	1.8	22.1	1.0	22.3	1.6	18.0	4.6
1250 – 1299	1275	29.9	1.5	29.2	1.1	28.5	2.1	29.6	1.2	26.9	1.9	26.9	5.2
1300 – 1349	1325	31.2	1.6	30.9	1.1	28.5	2.2	32.1	1.2	28.5	1.9	24.4	5.5
1350 – 1399	1374	24.1	1.4	22.4	1.0	22.2	2.1	22.2	1.0	25.0	1.8	40.0	5.7
1400 – 1449	1424	14.1	1.3	13.0	0.8	11.9	1.9	12.6	0.8	11.3	1.6	5.5	5.9
1450 – 1499	1474	10.9	1.3	10.2	0.7	11.4	2.0	10.4	0.8	13.4	1.6	19.2	6.2
1500 – 1549	1524	15.0	1.4	15.4	0.8	12.6	2.2	14.1	0.9	11.1	1.8	8.0	6.7
1550 – 1599	1574	22.1	1.6	20.9	1.0	22.1	2.4	21.1	1.0	24.1	2.0	23.8	7.2
1600 – 1649	1624	17.6	1.7	20.0	1.1	20.4	2.6	20.7	1.1	21.7	2.1	24.0	7.6
1650 – 1699	1674	19.2	1.7	18.4	1.0	14.7	2.6	18.1	1.0	18.9	2.0	12.9	8.0
1700 – 1749	1724	7.4	1.7	10.2	0.9	10.8	2.6	10.6	0.9	14.2	2.0	0.3	8.3
1750 – 1799	1775	10.1	1.7	8.7	0.9	11.3	2.7	8.5	0.9	8.0	2.0	14.9	8.8
1800 – 1849	1825	8.3	1.8	9.0	0.9	5.8	2.9	9.6	0.9	5.4	2.1	-0.4	9.4
1850 – 1899	1874	9.7	2.0	9.8	1.0	9.6	3.2	9.8	1.0	13.1	2.3	14.2	10.0
1900 – 1949	1924	12.7	2.1	12.9	1.1	18.2	3.3	12.0	1.1	7.8	2.4	0.6	10.6
1950 – 1999	1975	12.4	2.2	10.2	1.1	8.9	3.5	11.4	1.1	13.9	2.5	6.2	11.2
2000 – 2099	2049	6.7	1.2	6.3	0.6	7.9	2.0	6.3	0.6	6.2	1.4	4.9	6.7
2100 – 2199	2148	5.3	1.4	5.6	0.7	1.1	2.3	5.4	0.7	5.4	1.6	9.0	7.6
2200 – 2299	2248	7.3	1.6	7.6	0.8	6.8	2.6	6.0	0.7	7.2	1.8	8.7	8.6
2300 – 2399	2348	1.2	1.8	2.6	0.8	4.2	2.9	4.9	0.8	1.0	1.9	13.3	9.4
2400 – 2499	2448	6.8	2.0	4.0	0.9	5.2	3.2	2.6	0.8	5.2	2.1	-0.8	10.4
2500 – 2599	2548	2.9	2.2	2.5	1.0	0.2	3.5	2.6	0.9	3.0	2.3	-2.5	11.5
2600 – 2699	2648	5.9	2.5	0.5	1.1	-0.1	4.0	2.3	1.0	2.1	2.5	10.5	12.6
2700 – 2799	2748	-0.9	2.8	0.8	1.3	9.5	4.5	2.0	1.1	3.4	2.8	-6.4	14.1
2800 – 2899	2848	0.6	3.2	3.0	1.4	4.5	5.0	0.5	1.3	-3.2	3.2	-5.8	15.7
2900 – 2999	2948	-1.2	3.6	-2.4	1.6	-7.2	5.6	1.0	1.4	7.4	3.5	-3.6	17.1

Table 7.1: *EE* cross-frequency bandpowers, D_b, and their associated uncertainties, σ, , quoted in units of μK^2. The bandpower window function-weighted multipole multipole $\ell_{\rm eff}$ for each ℓ-range is also shown. The reported uncertainties are the square root of the diagonal elements of the covariance matrix and do not include beam or calibration uncertainties.

ℓ Range	$\ell_{\rm eff}$	90×90 GHz		90×150 GHz		90×220 GHz		150×150 GHz		150×220 GHz		220×220 GHz	
		D_ℓ	σ	D_ℓ	σ	D_ℓ	σ	D_ℓ	σ	D_ℓ	σ	D_ℓ	σ
300 – 349	326	88.4	12.0	93.2	12.1	99.8	13.7	101.1	12.7	110.5	14.0	113.7	20.3
350 – 399	376	43.6	8.8	42.4	8.7	36.6	10.5	42.7	9.2	40.8	10.7	40.1	17.2
400 – 449	426	-44.7	7.6	-45.6	7.3	-43.0	9.0	-47.8	7.5	-47.1	9.0	-43.4	15.0
450 – 499	475	-68.8	6.7	-68.9	6.2	-65.0	7.8	-70.0	6.4	-64.5	7.7	-53.2	13.2
500 – 549	523	-34.0	5.5	-34.6	5.0	-48.2	6.7	-34.8	5.2	-46.7	6.7	-58.2	12.2
550 – 599	574	11.8	6.2	11.2	5.8	15.2	7.4	10.5	6.1	15.6	7.3	20.8	12.4
600 – 649	625	24.1	7.0	23.8	6.7	21.5	8.1	24.5	7.0	23.1	8.1	21.4	12.8
650 – 699	675	-63.3	7.7	-63.3	7.4	-58.0	8.7	-63.1	7.5	-59.2	8.6	-60.0	13.0
700 – 749	725	-119.5	7.3	-120.9	6.9	-114.0	8.2	-122.8	7.0	-116.0	8.1	-105.2	12.7
750 – 799	774	-121.2	7.2	-120.4	6.7	-124.1	8.3	-121.3	6.8	-126.2	8.1	-124.6	12.9
800 – 849	824	-52.6	5.6	-50.5	4.8	-43.2	6.8	-48.6	5.0	-40.0	6.7	-25.6	12.1
850 – 899	874	41.0	5.8	38.5	5.1	38.5	6.9	36.6	5.3	37.2	6.8	36.7	11.9
900 – 949	924	54.5	5.5	56.0	4.9	58.9	6.6	56.9	5.1	61.5	6.5	70.4	11.3
950 – 999	974	12.4	5.3	13.1	4.8	14.4	6.3	13.9	5.0	13.8	6.2	18.0	10.6
1000 – 1049	1024	-52.0	5.6	-51.8	5.2	-55.5	6.5	-51.7	5.4	-55.8	6.4	-56.7	10.6
1050 – 1099	1075	-75.6	5.3	-74.6	4.7	-71.9	6.2	-73.7	4.9	-72.1	6.1	-70.1	10.4
1100 – 1149	1124	-48.3	4.6	-52.7	3.9	-58.4	5.6	-55.9	4.1	-60.3	5.5	-66.0	10.2
1150 – 1199	1174	-9.7	4.2	-10.1	3.4	-6.9	5.3	-10.8	3.6	-7.1	5.1	-1.9	10.0
1200 – 1249	1224	4.9	4.1	4.3	3.4	4.2	5.1	4.3	3.6	4.3	5.0	8.3	9.8
1250 – 1299	1274	-15.4	4.1	-15.7	3.4	-17.2	5.0	-16.0	3.6	-16.7	4.9	-16.4	9.6
1300 – 1349	1324	-47.1	4.2	-48.1	3.5	-43.6	5.1	-49.1	3.7	-42.9	4.9	-39.7	9.6
1350 – 1399	1374	-61.8	4.3	-61.8	3.5	-55.3	5.3	-63.0	3.7	-56.8	5.1	-47.5	10.0
1400 – 1449	1424	-41.0	4.1	-41.8	3.1	-41.2	5.2	-42.8	3.3	-41.1	5.0	-30.8	10.2
1450 – 1499	1474	-10.9	3.8	-11.8	2.8	-8.6	5.0	-13.0	3.0	-9.9	4.8	-4.2	10.1
1500 – 1549	1524	8.4	3.6	9.0	2.6	4.8	4.7	10.2	2.8	5.9	4.5	-7.4	9.8
1550 – 1599	1574	-3.8	3.5	-0.8	2.6	-4.2	4.5	1.1	2.8	0.3	4.3	-5.1	9.5
1600 – 1649	1624	-13.9	3.4	-15.4	2.5	-15.8	4.3	-14.5	2.7	-13.3	4.1	-8.0	9.4
1650 – 1699	1674	-31.0	3.3	-32.0	2.4	-32.4	4.3	-33.1	2.5	-31.7	4.0	-33.1	9.5
1700 – 1749	1724	-21.9	3.3	-24.0	2.3	-25.9	4.4	-25.9	2.5	-26.7	4.1	-25.1	9.8
1750 – 1799	1775	-15.7	3.3	-15.1	2.2	-17.6	4.4	-14.7	2.4	-17.4	4.1	-21.5	10.0
1800 – 1849	1824	-14.1	3.2	-10.0	2.1	-7.1	4.3	-8.4	2.2	-7.3	3.9	3.4	9.9
1850 – 1899	1874	-3.8	3.0	-3.3	2.0	-5.1	4.1	-3.4	2.2	-3.3	3.8	-12.6	9.8
1900 – 1949	1924	-11.8	3.0	-11.2	2.0	-10.8	4.1	-11.3	2.2	-11.0	3.7	-14.0	9.8
1950 – 1999	1975	-15.0	3.0	-16.4	2.0	-17.8	4.1	-16.3	2.1	-17.3	3.7	-18.7	10.1
2000 – 2099	2050	-16.0	1.7	-14.2	1.0	-14.6	2.3	-13.8	1.1	-14.0	2.1	-17.6	5.8
2100 – 2199	2151	-5.4	1.6	-4.7	1.0	-9.1	2.3	-4.3	1.1	-5.8	2.1	3.7	6.1
2200 – 2299	2250	-7.6	1.6	-6.3	1.0	-3.9	2.3	-5.0	1.0	-3.6	2.0	-9.2	6.4
2300 – 2399	2349	-8.9	1.6	-8.8	1.0	-10.6	2.4	-9.3	1.0	-10.5	2.0	-19.6	6.7
2400 – 2499	2450	-7.4	1.7	-4.7	0.9	-5.8	2.4	-2.3	1.0	-0.4	2.0	0.1	7.0
2500 – 2599	2549	-0.9	1.7	-4.2	0.9	-4.0	2.5	-3.6	1.0	-5.1	2.0	-14.3	7.4
2600 – 2699	2649	-5.0	1.8	-3.3	1.0	-6.5	2.7	-3.2	1.0	-3.5	2.1	-2.0	7.9
2700 – 2799	2749	1.5	1.9	-2.1	1.0	5.5	2.9	-3.8	1.0	1.9	2.2	16.3	8.5
2800 – 2899	2849	2.4	2.1	0.2	1.1	-0.3	3.1	-0.7	1.0	-5.5	2.3	-3.6	9.2
2900 – 2999	2949	-6.9	2.3	-1.8	1.1	-5.3	3.3	-2.1	1.1	0.2	2.4	15.6	9.7

Table 7.2: *TE* cross-frequency bandpowers, D_b, and their associated uncertainties, σ, , quoted in units of μK^2. The bandpower window function-weighted multipole $\ell_{\rm eff}$ for each ℓ-range is also shown. The reported uncertainties are the square root of the diagonal elements of the covariance matrix and do not include beam or calibration uncertainties.

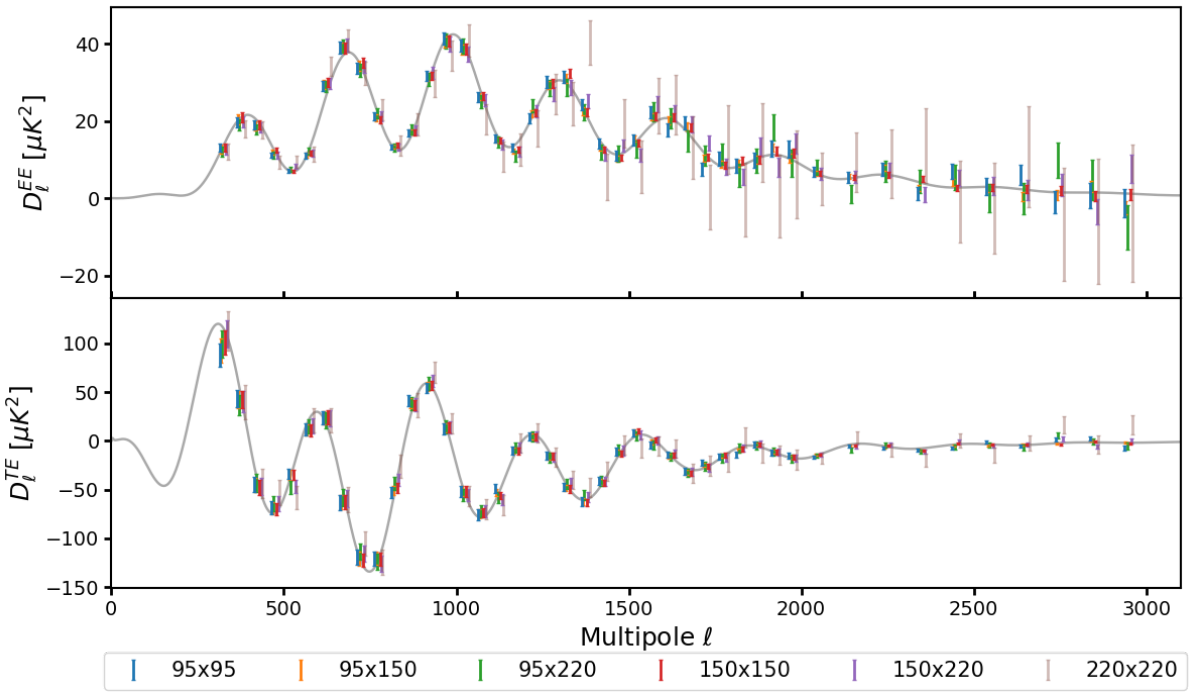

Figure 7.1: *EE (top)* and *TE (bottom)* bandpower measurements from the six auto- and cross-frequency power spectra overlaid on the *Planck* best-fit ΛCDM model. The plotted uncertainties are from the diagonal elements of the covariance matrix and do not include beam or calibration uncertainties. A small ℓ offset has been applied to each point for plotting purposes.

The resulting MV *EE* and *TE* bandpowers and associated errors are summarized in Table 7.3 and plotted in Figure 7.2 along with measurements from several recent experiments. Relative to the most sensitive single-frequency bandpowers, 150×150 GHz, the MV bandpowers reduce the errors by 5%-10% at $\ell < 1000$ and by 20%–30% at $\ell > 2000$. Representing just four months of data collection with approximately half of the full detector count, these 2018 SPT-3G bandpower constraints are already the most sensitive measurements made to date by an instrument on SPT over the multipole range $300 \leq \ell \leq 1400$ for *EE* and $300 \leq \ell \leq 1700$ for *TE*, and they are competitive with other current leading measurements.

We can check if the multifrequency data are consistent with the same underlying signal by examining the chi-square

$$\chi^2 = (D - M)^\intercal \mathbf{C}^{-1} (D - M) \ , \tag{7.2}$$

where $M = \mathbf{X}\bar{D}$. This evaluates to a χ^2 of 438.1, which for 528 individual bandpower measurements and 88 bandpowers, hence 440 remaining degrees of freedom, has a PTE of 0.52. If the *EE* and *TE* bandpowers are evaluated separately, the corresponding PTEs are 0.18 and 0.71, respectively. This indicates that the measurements from different frequency bands and their cross-correlations are all consistent with a common signal, with no significant contamination due to foregrounds or unmodeled systematics.

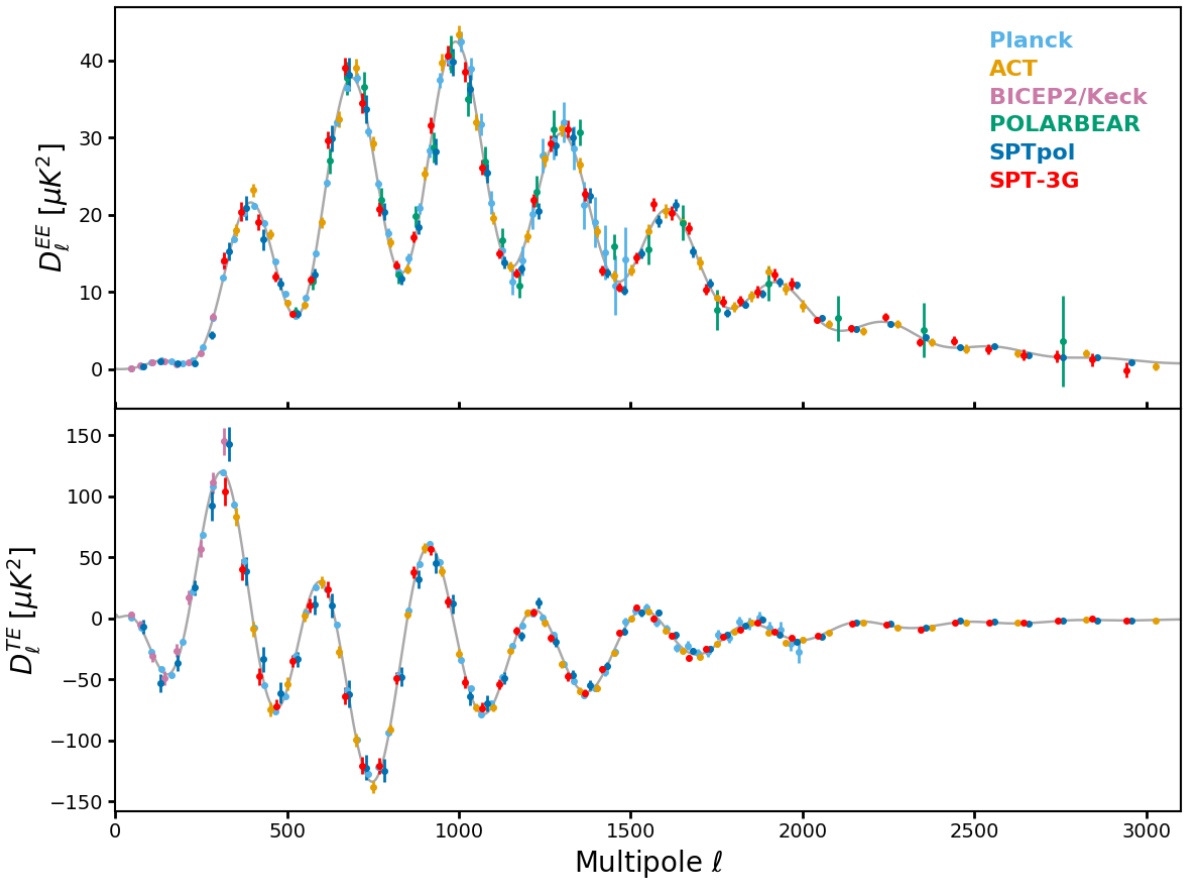

Figure 7.2: SPT-3G *EE* and *TE* minimum-variance bandpowers along with with measurements by other recent experiments, including *Planck* results from Planck Collaboration et al. (2020c) with the *EE* points restricted to $\ell < 1500$, ACT results from Choi et al. (2020), BICEP2/*Keck* results from BICEP2 and Keck Array Collaborations et al. (2015), POLARBEAR results from Adachi et al. (2020), and SPTpol results from Henning et al. (2018). The plotted uncertainties on the SPT-3G points are from the diagonal elements of the covariance matrix and do not include beam or calibration uncertainties. The solid curve is the *Planck* best-fit ΛCDM model.

ℓ Range	$\ell_{\rm eff}^{TE}$	D_ℓ^{TE}	σ^{TE}	$\ell_{\rm eff}^{EE}$	D_ℓ^{EE}	σ^{EE}
300 – 349	326	103.7	11.3	325	14.1	1.0
350 – 399	376	39.8	8.4	375	20.4	1.2
400 – 449	426	-47.8	7.0	425	19.0	1.1
450 – 499	475	-72.1	6.0	475	12.0	0.6
500 – 549	523	-35.1	4.7	524	7.2	0.4
550 – 599	574	10.2	5.6	575	11.6	0.6
600 – 649	625	23.6	6.6	624	29.7	1.1
650 – 699	675	-63.7	7.3	674	39.0	1.3
700 – 749	725	-120.8	6.8	725	34.5	1.2
750 – 799	774	-121.2	6.6	774	20.7	0.9
800 – 849	824	-49.2	4.7	824	13.5	0.6
850 – 899	874	38.0	5.0	874	17.1	0.7
900 – 949	924	56.6	4.9	924	31.6	1.0
950 – 999	974	13.3	4.8	974	40.6	1.3
1000 – 1049	1024	-52.3	5.2	1024	38.5	1.3
1050 – 1099	1075	-74.0	4.7	1075	26.2	1.0
1100 – 1149	1124	-54.2	3.8	1124	15.0	0.6
1150 – 1199	1174	-10.0	3.3	1174	12.4	0.6
1200 – 1249	1224	4.4	3.3	1224	21.9	0.9
1250 – 1299	1274	-15.9	3.3	1275	29.2	1.1
1300 – 1349	1324	-47.8	3.4	1325	31.1	1.1
1350 – 1399	1374	-61.7	3.4	1374	22.7	0.9
1400 – 1449	1424	-42.0	3.0	1424	12.8	0.7
1450 – 1499	1474	-11.9	2.7	1474	10.6	0.6
1500 – 1549	1524	9.1	2.5	1524	14.4	0.7
1550 – 1599	1574	-0.4	2.5	1574	21.4	0.9
1600 – 1649	1624	-14.7	2.4	1624	20.2	0.9
1650 – 1699	1674	-32.4	2.2	1674	18.2	0.8
1700 – 1749	1724	-24.9	2.2	1724	10.3	0.7
1750 – 1799	1775	-15.2	2.0	1775	8.8	0.7
1800 – 1849	1824	-9.4	1.9	1825	8.9	0.7
1850 – 1899	1874	-3.5	1.9	1874	10.0	0.8
1900 – 1949	1924	-11.3	1.8	1924	12.3	0.8
1950 – 1999	1975	-16.3	1.8	1975	11.1	0.8
2000 – 2099	2050	-14.2	0.9	2049	6.4	0.4
2100 – 2199	2151	-4.8	0.9	2148	5.3	0.5
2200 – 2299	2250	-5.6	0.8	2248	6.8	0.5
2300 – 2399	2349	-9.2	0.8	2348	3.5	0.5
2400 – 2499	2450	-3.6	0.8	2448	3.7	0.6
2500 – 2599	2549	-3.7	0.8	2548	2.6	0.6
2600 – 2699	2649	-3.5	0.8	2648	1.9	0.7
2700 – 2799	2749	-2.1	0.8	2748	1.7	0.8
2800 – 2899	2849	-0.5	0.8	2848	1.2	0.9
2900 – 2999	2949	-2.3	0.8	2948	-0.1	1.0

Table 7.3: The minimum-variance bandpowers D_b and their associated uncertainties σ for *TE* and *EE* spectra, quoted in units of $\mu\mathrm{K}^2$. The bandpower window function-weighted multipole $\ell_{\rm eff}$ for each ℓ-range is also shown. The reported uncertainties are the square root of the diagonal elements of the covariance matrix and do not include beam or calibration uncertainties.

7.2 Parameter Fitting Methodology

We use the set of auto- and cross-frequency bandpowers to obtain cosmological parameter constraints utilizing the Markov chain Monte Carlo (MCMC) package CosmoMC (Lewis & Bridle 2002).[1] In the MCMC method, an initial sample is drawn from multi-dimensional parameter space, the likelihood of those parameter values given the observed data calculated, and a new sample generated. Based on the likelihood of the new set of parameters, this step in parameter space is either added to the chain or discarded. After a sufficient number of samples, the posterior distribution of values for each parameter across the chain will converge to the probability distribution of that parameter. CosmoMC generates sample sets of cosmological parameters and interfaces with CAMB to propagate the parameters to CMB power spectra using either the standard ΛCDM model or a specified model extension; the spectra are then binned and compared against the SPT-3G bandpowers using a custom likelihood module, with the covariance matrix used as the proposal density for the size and direction of the step in parameter space to make for the next sample.

For each set of bandpowers, the SPT-3G likelihood modifies the theory spectra from CAMB to account for a number of instrumental and physical effects, including aberration due to relative motion with respect to the CMB rest frame (Jeong et al. 2014), super-sample lensing (Manzotti et al. 2014), and the emission spectra of galactic and extragalactic foregrounds. The nuisance parameters associated with these modifications are discussed below, with priors summarized Table 7.4.

We account for aberration in a manner similar to H18 and Louis et al. (2017), modifying the theory spectrum as

$$C_\ell \to C_\ell - C_\ell \frac{d \ln C_\ell}{d \ln \ell} \beta \langle \cos\theta \rangle, \tag{7.3}$$

with speed w.r.t. the CMB $\beta = 1.23 \times 10^{-3}$ and angular separation between the CMB dipole and the SPT-3G survey field $\langle \cos\theta \rangle = -0.39$. This modification to the spectrum requires

1. https://cosmologist.info/cosmomc/

no additional nuisance parameters.

For super-sample lensing, we follow the procedure laid out in C15 and H18, modifying the spectrum at each MCMC sample $\mathbf{p}$ as

$$\hat{C}_\ell^{XY}(\mathbf{p};\kappa) = C_\ell^{XY}(\mathbf{p}) - \frac{\partial \ell^2 C_\ell^{XY}(\mathbf{p})}{\partial \ln \ell}\frac{\kappa}{\ell^2}, \tag{7.4}$$

where the nuisance parameter κ quantifies the mean lensing convergence across the survey field. We apply a Gaussian prior on κ centered on 0 with standard deviation calculated as prescribed in Manzotti et al. (2014) to be $\sigma_\kappa = 4.5 \times 10^{-4}$, with the smaller uncertainty relative to H18 stemming from the increased survey size.

We model two sources of foreground power in the same manner as in H18: Poisson-distributed point sources with angular power that scales as $D_\ell^{\rm ps} \sim \ell^2$ and polarized galactic dust with emission described by a power law. For the Poisson-distributed sources, we set a Gaussian prior on $D_{3000}^{\rm ps}$ with central value given by the temperature values from Reichardt et al. (2020) scaled by the polarization fractions reported in Gupta et al. (2019). As the uncertainty in polarization fraction dominates the relative uncertainty in this calculation, we increase it by a factor of two to 30% and adopt this as the width of the prior. We assume any Poisson *TE* component to be negligible.

We model the power from polarized Galactic dust assuming a modified blackbody spectrum with $T_{\rm dust} = 19.6$ K, $\beta_{\rm dust} = 1.59$ and using the relation from Planck Collaboration et al. (2016b):

$$D_{\ell,{\rm dust}}^{XY} = A_{80}^{XY}\left(\frac{\ell}{80}\right)^{\alpha_{XY}+2}, \tag{7.5}$$

where A_{80}^{XY} is the amplitude of the spectrum at $\ell = 80$ at 150 GHz, and α_{XY} is the angular power dust spectral index. We apply a Gaussian prior to α_{XY} with *Planck*-determined central value -2.42 and uncertainty 0.02, and we apply flat priors on A_{80}^{XY} over the range 0–2 μK.

For the range of angular multipoles considered here, the optical depth to reionization

τ is degenerate with the amplitude of scalar fluctuations $A_{\rm s}$; we therefore use large-scale polarization information from Planck Collaboration et al. (2020b) to inform a Gaussian prior of $\tau = 0.0543 \pm 0.0073$ and report constraints on the combined quantity $10^9 A_{\rm s} e^{-2\tau}$.

Parameter	Prior
τ	0.0543 ± 0.0073
100κ	0 ± 0.045
A_{80}^{EE}	0–2
α_{EE}	-2.42 ± 0.02
A_{80}^{TE}	0–2
α_{TE}	-2.42 ± 0.02
$D_{3000}^{\rm ps,\ 95\times95}$	0.0405 ± 0.0121
$D_{3000}^{\rm ps,\ 150\times150}$	0.0115 ± 0.0034
$D_{3000}^{\rm ps,\ 220\times220}$	0.0476 ± 0.0143
$D_{3000}^{\rm ps,\ 95\times150}$	0.0180 ± 0.0054
$D_{3000}^{\rm ps,\ 95\times220}$	0.0157 ± 0.0047
$D_{3000}^{\rm ps,\ 150\times220}$	0.0190 ± 0.0057

Table 7.4: Priors used for the MCMC fit, including the optical depth to reionization τ, mean-field lensing convergence κ, the amplitude A_{80}^{XY} (in μK^2) and spectral index α_{80}^{XY} of polarized Galactic dust, the *EE* power of Poisson-distributed point sources $D_{3000}^{\rm ps,\ \nu_{\rm i}\times\nu_{\rm j}}$ (in μK^2).

7.3 Cosmological Parameter Constraints

The SPT-3G ΛCDM parameter constraints are summarized in Table 7.5, and the 1D and 2D marginalized constraints are shown in comparison to results from SPTpol and *Planck* in Figure 7.3.

SPT-3G finds the value of the Hubble constant to be

$$H_0 = 68.6 \pm 1.5\,{\rm km/s/Mpc}, \tag{7.6}$$

	SPT-3G	SPT-3G+*Planck*	*Planck*	SPTpol
Free				
$100\Omega_b h^2$	2.229 ± 0.034	2.238 ± 0.013	2.236 ± 0.015	2.296 ± 0.048
$\Omega_c h^2$	0.1152 ± 0.0037	0.1197 ± 0.0013	0.1202 ± 0.0014	0.1098 ± 0.0048
$100\theta_{MC}$	1.03965 ± 0.00072	1.04072 ± 0.00028	1.04090 ± 0.00031	1.0398 ± 0.0013
$10^9 A_s e^{-2\tau}$	1.818 ± 0.038	1.881 ± 0.011	1.884 ± 0.012	1.7791 ± 0.0528
n_s	1.003 ± 0.019	0.9663 ± 0.0041	0.9649 ± 0.0044	0.9967 ± 0.0238
Derived				
Ω_Λ	0.706 ± 0.021	0.6857 ± 0.0077	0.6834 ± 0.0084	0.736 ± 0.025
σ_8	0.791 ± 0.016	0.8086 ± 0.0070	0.8120 ± 0.0073	0.771 ± 0.024
S_8	0.783 ± 0.041	0.828 ± 0.015	0.834 ± 0.016	0.723 ± 0.052
H_0 [km/s/Mpc]	68.6 ± 1.5	67.41 ± 0.55	67.27 ± 0.60	71.3 ± 2.1
Age/Gyr	13.819 ± 0.051	13.801 ± 0.022	13.800 ± 0.024	13.718 ± 0.074

Table 7.5: Marginalized ΛCDM parameter constraints and 68% errors from SPT-3G, along with constraints SPTpol (H18) and *Planck* (Planck Collaboration et al. 2020b). Note that SPT-3G and SPTpol do not constrain τ, but use *Planck*-based Gaussian priors of 0.0543 ± 0.0073 and 0.078 ± 0.019, respectively.

in good agreement with the other CMB experiments as well as with local distance ladder measurements that have been calibrated using the tip of the red giant branch method (Freedman et al. 2019). However, this value is 2.6σ lower than the value of $H_0 = 74.03 \pm 1.42$ km/s/Mpc found by Riess et al. (2019) using Cepheid-calibrated distance ladder measurements, and 2.0σ lower than the value of $H_0 = 73.3^{+1.7}_{-1.8}$ km/s/Mpc found by Wong et al. (2020) using the time delays of gravitationally lensed quasars. The growing discrepancy between distance ladder measurements and those derived from the CMB using ΛCDM has been a hot topic in cosmology the last few years (see e.g., Di Valentino et al. (2020) and references therein), and while the results presented here do not show as large as disagreement as that between Riess et al. (2019) and Planck Collaboration et al. (2020b), they do add another (mostly) independent CMB measurement that demonstrates the tension between H_0 values.

The largest disagreement between SPT-3G and *Planck* is in the value of the scalar spectral index, n_s, with a 2.0σ discrepancy. In H18 it was found that the $\ell > 1000$ modes were driving the inconsistency, and a value of n_s in line with *Planck* was obtained when only considering modes with $\ell < 1000$. A similar reduction was achieved when combining SPTpol data with

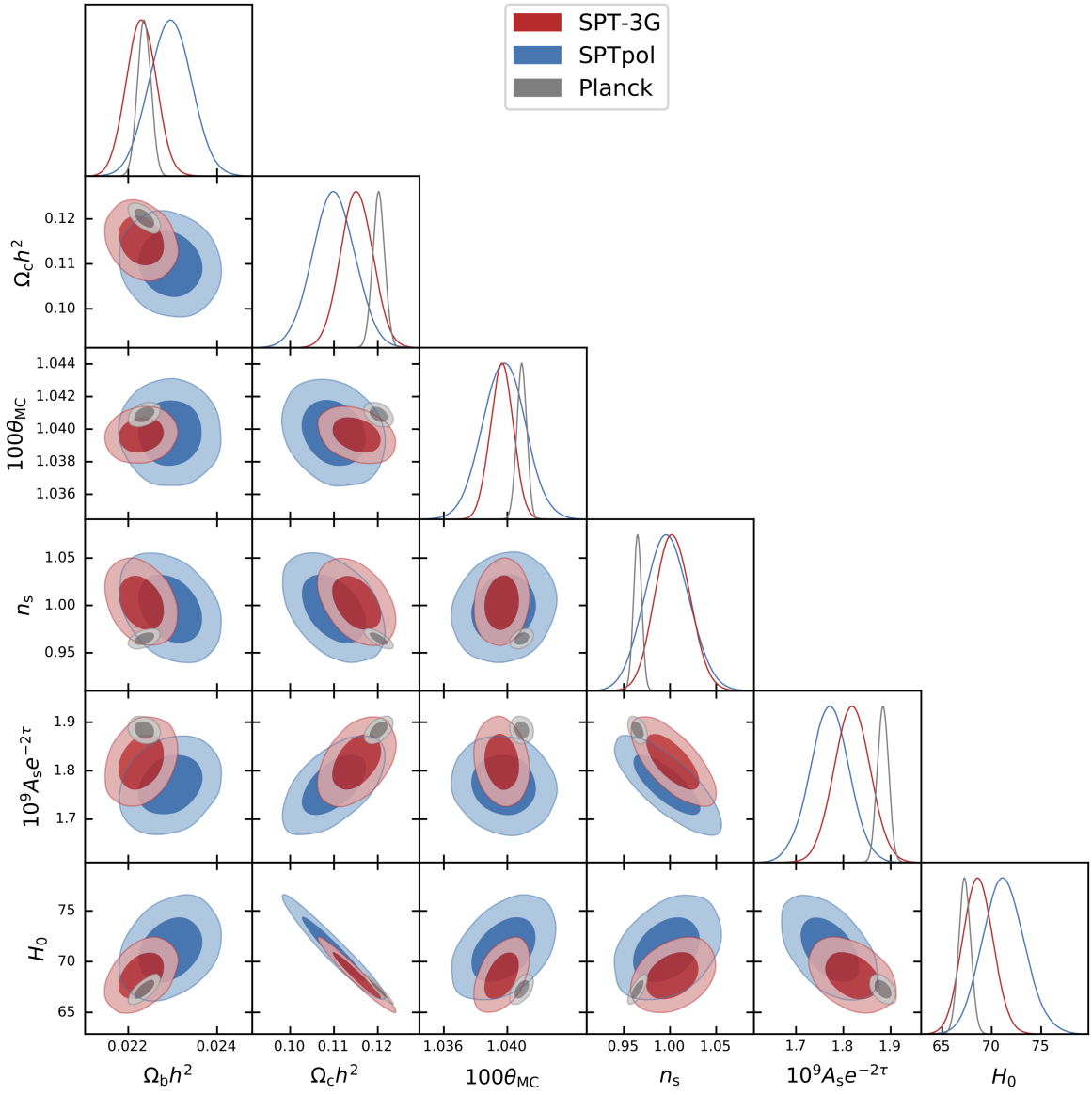

Figure 7.3: Marginalized ΛCDM parameter constraints from SPT-3G, showing the one-dimensional posterior distributions and two-dimensional contours indicating the 68% and 95% confidence regions. The TT,TE,EE+lowℓ+lowE results from Planck Collaboration et al. (2020b) and the SPTpol results from H18 are shown for comparison. Figure generated by Lennart Balkenhol.

temperature information from *Planck*. A high value of n_s was also reported in Aiola et al. (2020), with lower values produced when using a *WMAP* prior on the amplitude of the first peak of the *TT* spectrum. To investigate where the preference for high n_s is coming from, we can divide the full SPT-3G 2018 dataset into seven subsets: the 95, 150, and 220 GHz auto-frequency spectra, the $\ell \leq 1000$ and $\ell > 1000$ bandpowers, and the *EE* spectra and *TE* spectra individually. The parameter constraints from these subsets along with those from the full dataset are shown in Figure 7.4. We see that the high-ℓ data has a preference for high n_s, a similar finding to H18 and Choi et al. (2020). We also note that the *EE* (*TE*) subset has a preference for a low (high) value of $\Omega_c h^2$, another trend also observed in both H18 and Choi et al. (2020). Despite these trends, the χ^2 values for these subsets evaluated against the full dataset at the parameter level all have corresponding PTEs within the central 90% confidence interval [5.0%, 95.0%], and we conclude there are no significant tensions within the SPT-3G dataset.

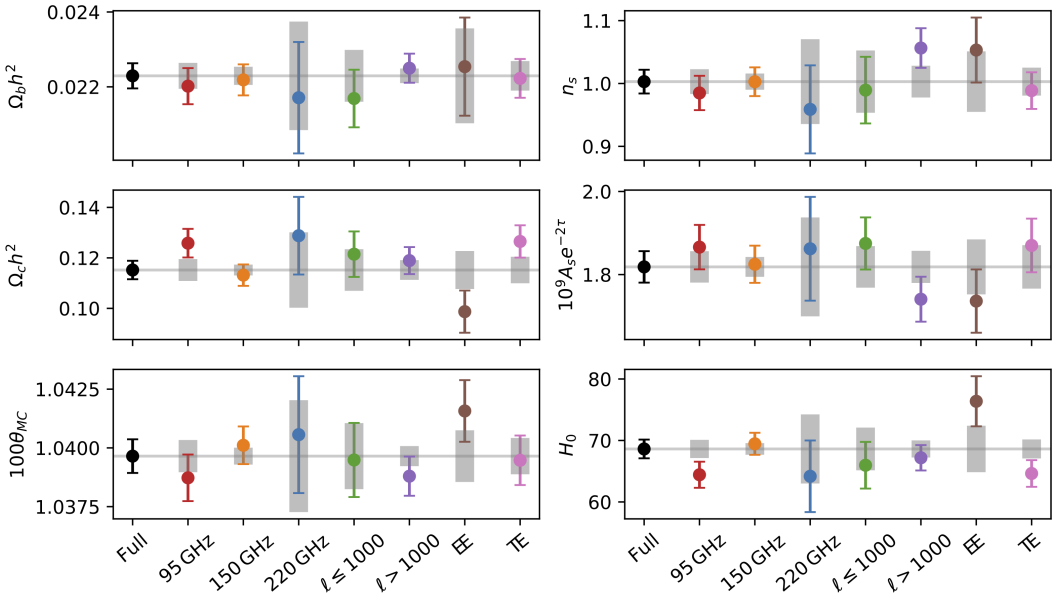

Figure 7.4: Parameter constraints from various subsets of the SPT-3G 2018 data. The gray boxes indicated the expected level of statistical fluctuation, computed according to Gratton & Challinor (2019). Figure generated by Lennart Balkenhol.

7.3.1 *Lensing and* $A_{\rm L}$

The line-of-sight distribution of matter between us and the surface of last scattering results in gravitational lensing of the CMB and smoothing of the acoustic peaks. The additional parameter $A_{\rm L}$ accounts for this damping (Calabrese et al. 2008): in standard ΛCDM $A_{\rm L} = 1$, while $A_{\rm L} = 0$ corresponds to no lensing. Evidence for smaller-than-expected gravitational lensing was reported in H18, with a value of $A_{\rm L} = 0.81 \pm 0.14$, while Planck Collaboration et al. (2020b) preferred a value above unity of $A_{\rm L} = 1.180 \pm 0.065$. If we allow $A_{\rm L}$ to float, the SPT-3G bandpowers prefer

$$A_{\rm L} = 0.97 \pm 0.11 \ , \tag{7.7}$$

with no appreciable shift in the other fitted parameters. This value is within 1.6σ and 0.9σ of the values found by *Planck* and H18, respectively, and is in excellent agreement with both the standard ΛCDM prediction and the value of $A_{\rm L} = 1.01 \pm 0.11$ reported in Aiola et al. (2020).

7.3.2 *Consistency with* ΛCDM

The SPT-3G dataset is consistent with the ΛCDM model. In Figure 7.5 and Figure 7.6 I plot the residuals of the minimum variance *EE* and *TE* bandpowers, respectively, to the best-fit ΛCDM model to the full set of multifrequency bandpowers. The corresponding PTE for both spectra considered together is 0.41, while the *EE*-only PTE is 0.12 and the *TE*-only PTE is 0.82, showing no evidence of tension with the standard ΛCDM model.

7.3.3 *SPT-3G + Planck*

The SPT-3G and *Planck* datasets are naturally complementary, with *Planck* providing the best measurements of CMB power spectra on large scales and SPT-3G providing excellent constraints on intermediate and small scales. We report the joint marginalized constraints from the SPT-3G and *Planck* BASE_PLIKHM_TTTEEE_LOWL_LOWE datasets in Figure 7.7

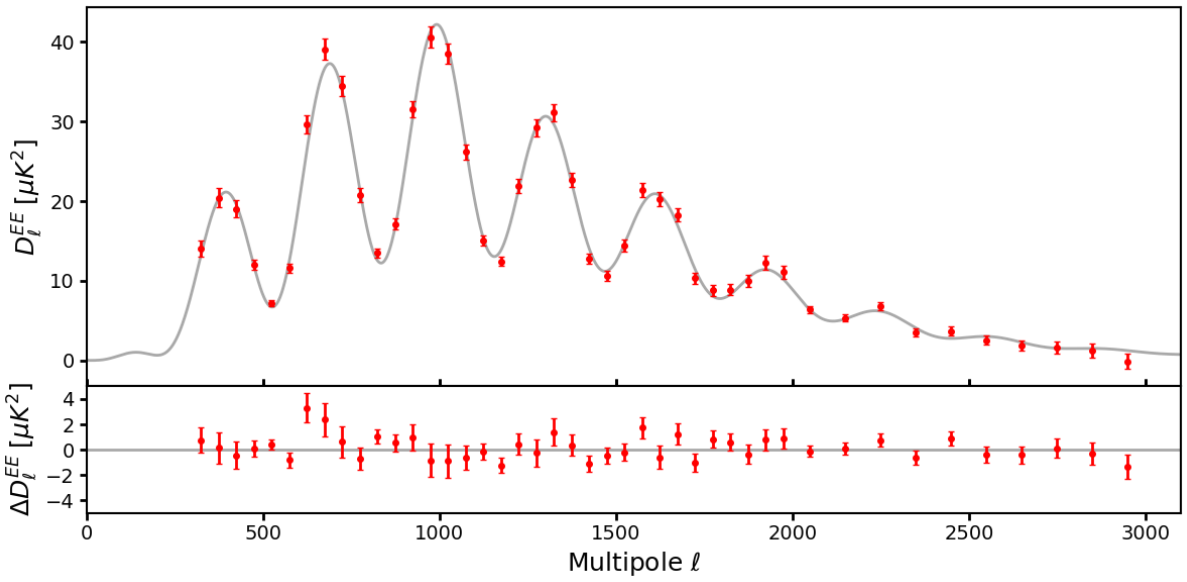

Figure 7.5: Minimum-variance *EE* bandpowers and residuals against the best-fit ΛCDM model. The plotted uncertainties are from the diagonal elements of the covariance matrix and do not include beam or calibration uncertainties.

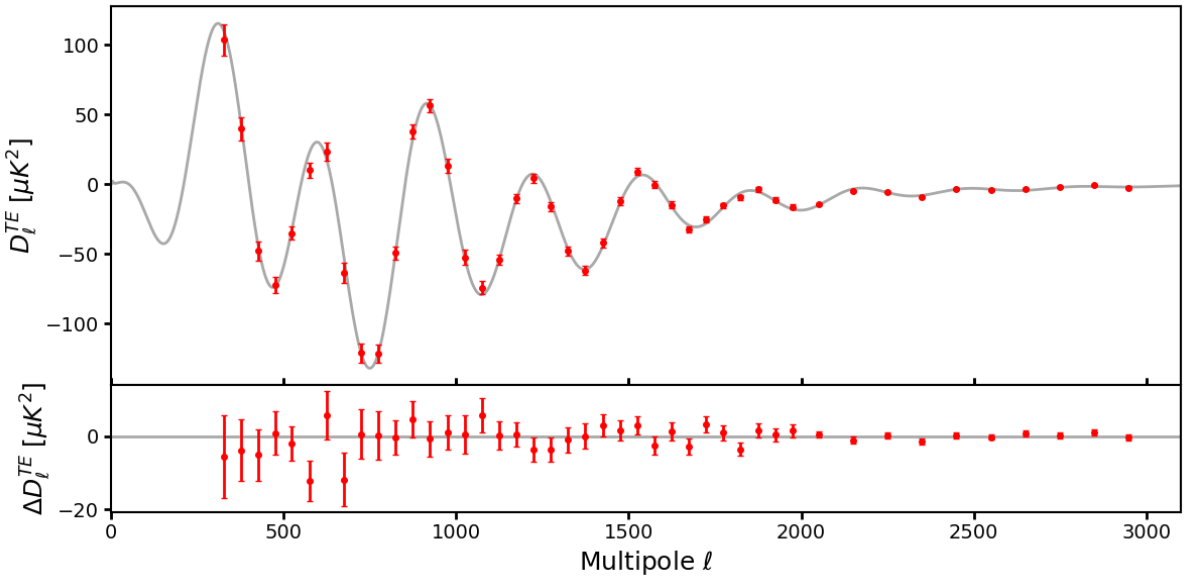

Figure 7.6: Minimum-variance *TE* bandpowers and residuals against the best-fit ΛCDM model. The plotted uncertainties are from the diagonal elements of the covariance matrix and do not include beam or calibration uncertainties.

and Table 7.5. The inclusion of the 2018 SPT-3G dataset to *Planck* does not significantly shift the best-fit parameter values, but by comparing the determinants of the parameter

covariance matrices, we find the inclusion of SPT-3G data reduces the available volume of six-dimensional ΛCDM parameter space by a factor of 1.5.

7.4 Conclusion

This thesis has touched on nearly all stages of the SPT-3G experiment; from initial planning and design, to construction and deployment, to daily operation and production of scientific results. I have analyzed data taken during 2018 to present the very first measurements of CMB power spectra with SPT-3G and shown the resulting constraints on cosmological parameters. Though they are based on just four months of data collection with approximately half of the full detector count, these measurements are already comparable to or exceed other current leading ground-based measurements. The value of the Hubble constant obtained with SPT-3G data is $H_0 = 68.6 \pm 1.5\,\mathrm{km/s/Mpc}$, adding to the collection of CMB measurements preferring a value of $H_0 < 70\,\mathrm{km/s/Mpc}$ and emphasizing the tension with local distance ladder measurements. Despite the lack of significant internal tension within the full dataset, various subsets of the data show intriguing differences in parameter values that are corroborated by external experiments. More measurements with greater precision are required to either confirm or dismiss these discrepancies. While I find no evidence of tension with ΛCDM, further investigations of this dataset will explore extensions to the standard model, including massive neutrinos (Σm_ν), additional relativistic species ($\mathrm{N_{eff}}$), and changes to the primordial helium fraction (Y_p). At the time of writing, SPT-3G has two additional observing seasons' worth of data on disk, with combined map depths 3–4× deeper than what was used for this analysis, and the survey will continue through at least 2023. The full-depth SPT-3G survey, with an unprecedented combination of sensitivity and angular resolution, will be able to address these issues and many more, yielding powerful consistency tests of ΛCDM, constraining the nature of dark energy, and probing the physics of inflation.

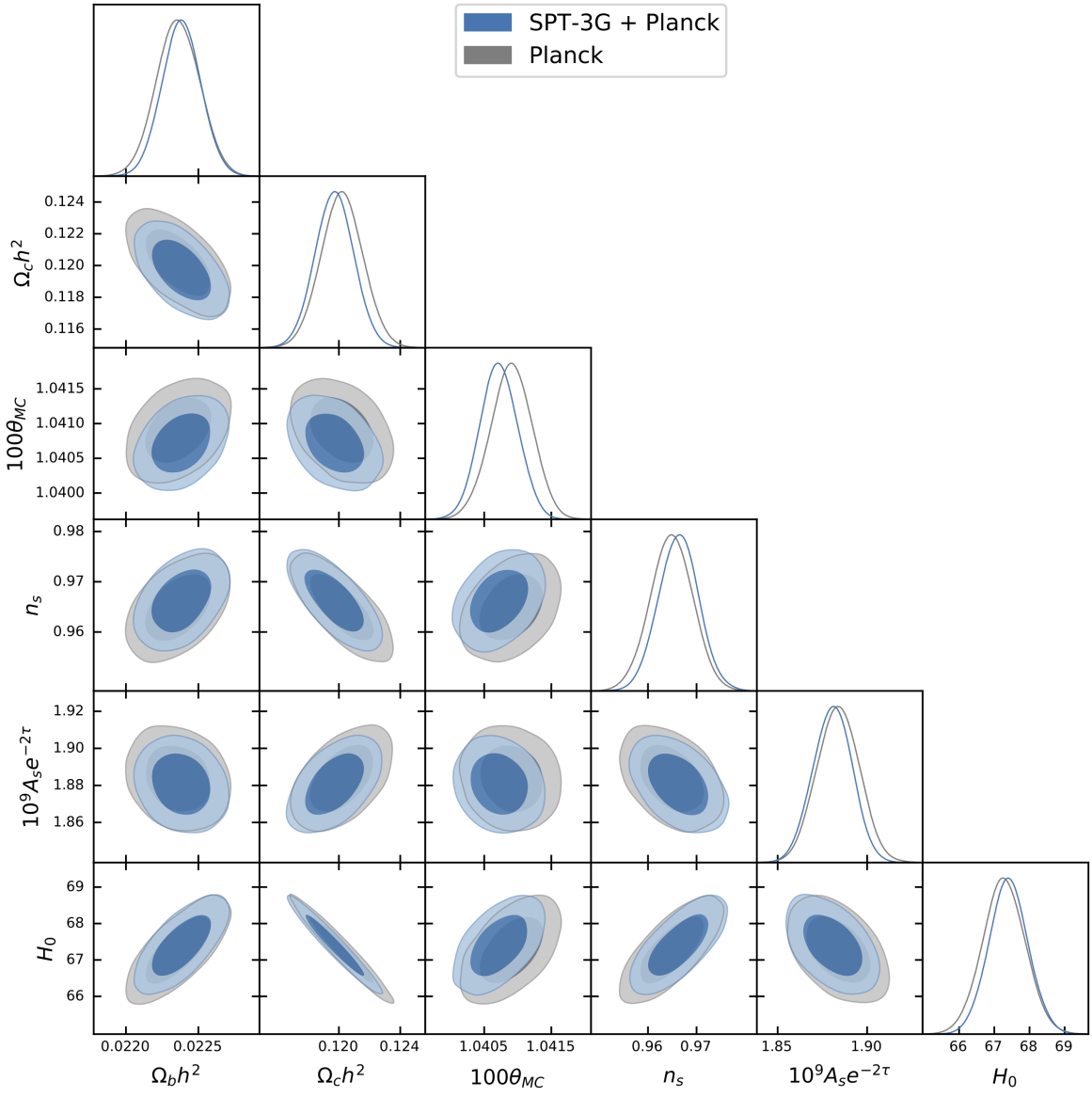

Figure 7.7: Joint marginalized ΛCDM parameter constraints from SPT-3G + *Planck* showing the one-dimensional posterior distributions and two-dimensional contours indicating the 68% and 95% confidence regions. *Planck*-only constraints are shown for comparison. Figure generated by Lennart Balkenhol.

REFERENCES

Adachi, S., Faúndez, M. A. O. A., Arnold, K., et al. 2020, arXiv:2005.06168 [astro-ph]. https://arxiv.org/abs/2005.06168

Aiola, S., Calabrese, E., Maurin, L., et al. 2020, arXiv:2007.07288 [astro-ph]. https://arxiv.org/abs/2007.07288

Anderson, A. J., Ade, P. A. R., Ahmed, Z., et al. 2019, J Low Temp Phys, doi: 10.1007/s10909-019-02259-7

Andrews, D. H., Brucksch, W. F., Ziegler, W. T., & Blanchard, E. R. 1942, Review of Scientific Instruments, 13, 281, doi: 10.1063/1.1770037

Austermann, J. E., Aird, K. A., Beall, J. A., et al. 2012, in Millimeter, Submillimeter, and Far-Infrared Detectors and Instrumentation for Astronomy VI, Vol. 8452 (International Society for Optics and Photonics), 84521E, doi: 10.1117/12.927286

Avva, J. S., Ade, P. A. R., Ahmed, Z., et al. 2018, J Low Temp Phys, 193, 547, doi: 10.1007/s10909-018-1965-5

Bandura, K., Bender, A. N., Cliche, J. F., et al. 2016, J. Astron. Instrum., 05, 1641005, doi: 10.1142/S2251171716410051

Bender, A. N., Cliche, J.-F., de Haan, T., et al. 2014, in Millimeter, Submillimeter, and Far-Infrared Detectors and Instrumentation for Astronomy VII, Vol. 9153 (International Society for Optics and Photonics), 91531A, doi: 10.1117/12.2054949

Bender, A. N., Ade, P. a. R., Anderson, A. J., et al. 2016, in Millimeter, Submillimeter, and Far-Infrared Detectors and Instrumentation for Astronomy VIII, Vol. 9914 (International Society for Optics and Photonics), 321–331, doi: 10.1117/12.2232146

Bender, A. N., Ade, P. a. R., Ahmed, Z., et al. 2018, in Millimeter, Submillimeter, and Far-Infrared Detectors and Instrumentation for Astronomy IX, Vol. 10708 (International Society for Optics and Photonics), 1–21, doi: 10.1117/12.2312426

Bender, A. N., Anderson, A. J., Avva, J. S., et al. 2019, J Low Temp Phys, doi: 10.1007/s10909-019-02280-w

Benson, B. A., Ade, P. A. R., Ahmed, Z., et al. 2014, in Millimeter, Submillimeter, and Far-Infrared Detectors and Instrumentation for Astronomy VII, Vol. 9153 (Montréal, Quebec, Canada: SPIE), 552–572, doi: 10.1117/12.2057305

Béthermin, M., Daddi, E., Magdis, G., et al. 2012, ApJL, 757, L23, doi: 10.1088/2041-8205/757/2/L23

BICEP2 and Keck Array Collaborations, Ade, P. A. R., Ahmed, Z., et al. 2015, ApJ, 811, 126, doi: 10.1088/0004-637X/811/2/126

—. 2018, Phys. Rev. Lett., 121, 221301, doi: 10.1103/PhysRevLett.121.221301

Calabrese, E., Slosar, A., Melchiorri, A., Smoot, G. F., & Zahn, O. 2008, Phys. Rev. D, 77, 123531, doi: 10.1103/PhysRevD.77.123531

Carlstrom, J. E., Ade, P. A. R., Aird, K. A., et al. 2011, Publications of the Astronomical Society of the Pacific, 123, 568, doi: 10.1086/659879

Carter, F. W., Ade, P. a. R., Ahmed, Z., et al. 2018, J Low Temp Phys, 193, 695, doi: 10.1007/s10909-018-1910-7

Chamberlin, R. A. 2001, Journal of Geophysical Research: Atmospheres, 106, 20101, doi: 10.1029/2001JD900208

Choi, S. K., Hasselfield, M., Ho, S.-P. P., et al. 2020, arXiv:2007.07289 [astro-ph]. https://arxiv.org/abs/2007.07289

Crites, A. T., Henning, J. W., Ade, P. A. R., et al. 2015, ApJ, 805, 36, doi: 10.1088/0004-637X/805/1/36

Datta, R., Aiola, S., Choi, S. K., et al. 2019, Mon Not R Astron Soc, 486, 5239, doi: 10.1093/mnras/sty2934

de Haan, T., Smecher, G., & Dobbs, M. 2012, in Millimeter, Submillimeter, and Far-Infrared Detectors and Instrumentation for Astronomy VI, Vol. 8452 (International Society for Optics and Photonics), 84520E, doi: 10.1117/12.925658

De Zotti, G., Ricci, R., Mesa, D., et al. 2005, A&A, 431, 893, doi: 10.1051/0004-6361:20042108

Di Valentino, E., Anchordoqui, L. A., Akarsu, O., et al. 2020, arXiv:2008.11284 [astro-ph, physics:hep-ph]. https://arxiv.org/abs/2008.11284

Dicke, R. H., Peebles, P. J. E., Roll, P. G., & Wilkinson, D. T. 1965, The Astrophysical Journal, 142, 414, doi: 10.1086/148306

Ding, J., Ade, P. A. R., Anderson, A. J., et al. 2017, IEEE Transactions on Applied Superconductivity, 27, 1, doi: 10.1109/TASC.2016.2639378

Dobbs, M. A., Lueker, M., Aird, K. A., et al. 2012, Review of Scientific Instruments, 83, 073113, doi: 10.1063/1.4737629

Doriese, W. B., Morgan, K. M., Bennett, D. A., et al. 2016, J Low Temp Phys, 184, 389, doi: 10.1007/s10909-015-1373-z

DuHamel, R. H. 1987, Dual Polarized Sinuous Antennas, United States Patent 4658262

Dutcher, D., Ade, P. a. R., Ahmed, Z., et al. 2018, in Millimeter, Submillimeter, and Far-Infrared Detectors and Instrumentation for Astronomy IX, Vol. 10708 (International Society for Optics and Photonics), 246–258, doi: 10.1117/12.2312451

Edwards, J. M., O'Brient, R., Lee, A. T., & Rebeiz, G. M. 2012, IEEE Transactions on Antennas and Propagation, 60, 4082, doi: 10.1109/TAP.2012.2207048

Everett, W. B., Zhang, L., Crawford, T. M., et al. 2020, ApJ, 900, 55, doi: 10.3847/1538-4357/ab9df7

Fixsen, D. J. 2009, ApJ, 707, 916, doi: 10.1088/0004-637X/707/2/916

Freedman, W. L., Madore, B. F., Hatt, D., et al. 2019, ApJ, 882, 34, doi: 10.3847/1538-4357/ab2f73

Galitzki, N., Ali, A., Arnold, K. S., et al. 2018, Millimeter, Submillimeter, and Far-Infrared Detectors and Instrumentation for Astronomy IX, 3, doi: 10.1117/12.2312985

Galli, S., Benabed, K., Bouchet, F., et al. 2014, Phys. Rev. D, 90, 063504, doi: 10.1103/PhysRevD.90.063504

George, E. M., Reichardt, C. L., Aird, K. A., et al. 2015, ApJ, 799, 177, doi: 10.1088/0004-637X/799/2/177

Górski, K. M., Hivon, E., Banday, A. J., et al. 2005, ApJ, 622, 759, doi: 10.1086/427976

Gratton, S., & Challinor, A. 2019, arXiv:1911.07754 [astro-ph]. https://arxiv.org/abs/1911.07754

Gupta, N., Reichardt, C. L., Ade, P. a. R., et al. 2019, Mon Not R Astron Soc, 490, 5712, doi: 10.1093/mnras/stz2905

Henderson, S. W., Allison, R., Austermann, J., et al. 2016, J Low Temp Phys, 184, 772, doi: 10.1007/s10909-016-1575-z

Henning, J. W., Sayre, J. T., Reichardt, C. L., et al. 2018, ApJ, 852, 97, doi: 10.3847/1538-4357/aa9ff4

Hivon, E., Gorski, K. M., Netterfield, C. B., et al. 2002, ApJ, 567, 2, doi: 10.1086/338126

Hu, W., & Dodelson, S. 2002, Annu. Rev. Astron. Astrophys., 40, 171, doi: 10.1146/annurev.astro.40.060401.093926

Hu, W., & White, M. 1997, New Astronomy, 2, 323, doi: 10.1016/S1384-1076(97)00022-5

Hubble, E. 1929, Proceedings of the National Academy of Science, 15, 168, doi: 10.1073/pnas.15.3.168

Huber, M., Neil, P., Benson, R., et al. 2001, IEEE Transactions on Applied Superconductivity, 11, 4048, doi: 10.1109/77.947383

Hui, H., Ade, P. a. R., Ahmed, Z., et al. 2018, in Millimeter, Submillimeter, and Far-Infrared Detectors and Instrumentation for Astronomy IX, Vol. 10708 (International Society for Optics and Photonics), 1070807, doi: 10.1117/12.2311725

Irwin, K., & Hilton, G. 2005, in Cryogenic Particle Detection (Springer Berlin Heidelberg), 63–150, doi: 10.1007/10933596_3

Irwin, K. D., Hilton, G. C., Wollman, D. A., & Martinis, J. M. 1998, Journal of Applied Physics, 83, 3978, doi: 10.1063/1.367153

Irwin, K. D., & Lehnert, K. W. 2004, Appl. Phys. Lett., 85, 2107, doi: 10.1063/1.1791733

Jeong, D., Chluba, J., Dai, L., Kamionkowski, M., & Wang, X. 2014, Phys. Rev. D, 89, 023003, doi: 10.1103/PhysRevD.89.023003

Jones, W. C., Montroy, T. E., Crill, B. P., et al. 2007, A&A, 470, 771, doi: 10.1051/0004-6361:20065911

Kamionkowski, M., Kosowsky, A., & Stebbins, A. 1997, Phys. Rev. Lett., 78, 2058, doi: 10.1103/PhysRevLett.78.2058

Keisler, R., Reichardt, C. L., Aird, K. A., et al. 2011, ApJ, 743, 28, doi: 10.1088/0004-637X/743/1/28

Keisler, R., Hoover, S., Harrington, N., et al. 2015, ApJ, 807, 151, doi: 10.1088/0004-637X/807/2/151

Kittel, C., & Kroemer, H. 1980, Thermal Physics, 2nd edn. (San Francisco: W. H. Freeman)

Langley, S. P. 1880, Proceedings of the American Academy of Arts and Sciences, 16, 342, doi: 10.2307/25138616

Lemaître, A. G. 1931a, Mon Not R Astron Soc, 91, 483, doi: 10.1093/mnras/91.5.483

—. 1931b, Nature, 128, 704, doi: 10.1038/128704a0

Lewis, A., & Bridle, S. 2002, Phys. Rev. D, 66, 103511, doi: 10.1103/PhysRevD.66.103511

Lewis, A., Challinor, A., & Lasenby, A. 2000, ApJ, 538, 473, doi: 10.1086/309179

Louis, T., Grace, E., Hasselfield, M., et al. 2017, J. Cosmol. Astropart. Phys., 2017, 031, doi: 10.1088/1475-7516/2017/06/031

Lueker, M., Reichardt, C. L., Schaffer, K. K., et al. 2010, ApJ, 719, 1045, doi: 10.1088/0004-637X/719/2/1045

Manzotti, A., Hu, W., & Benoit-Lévy, A. 2014, Phys. Rev. D, 90, 023003, doi: 10.1103/PhysRevD.90.023003

Mocanu, L. M., Crawford, T. M., Aylor, K., et al. 2019, J. Cosmol. Astropart. Phys., 2019, 038, doi: 10.1088/1475-7516/2019/07/038

Nadolski, A., Vieira, J. D., Sobrin, J. A., et al. 2020, Appl. Opt., 59, 3285, doi: 10.1364/AO.383921

O'Brient, R. 2010, PhD thesis, University of California, Berkeley

O'Brient, R., Ade, P., Arnold, K., et al. 2013, Appl. Phys. Lett., 102, 063506, doi: 10.1063/1.4791692

Pan, Z., Liu, M., Thakur, R. B., et al. 2019, Appl. Opt., AO, 58, 6257, doi: 10.1364/AO.58.006257

Pan, Z., Ade, P. A. R., Ahmed, Z., et al. 2018, J Low Temp Phys, 193, 305, doi: 10.1007/s10909-018-1935-y

Penzias, A. A., & Wilson, R. W. 1965, The Astrophysical Journal, 142, 419, doi: 10.1086/148307

Planck Collaboration, Aghanim, N., Arnaud, M., et al. 2016a, A&A, 594, A11, doi: 10.1051/0004-6361/201526926

Planck Collaboration, Adam, R., Ade, P. a. R., et al. 2016b, A&A, 586, A133, doi: 10.1051/0004-6361/201425034

Planck Collaboration, Akrami, Y., Ashdown, M., et al. 2020a, A&A, 641, A4, doi: 10.1051/0004-6361/201833881

Planck Collaboration, Aghanim, N., Akrami, Y., et al. 2020b, A&A, 641, A6, doi: 10.1051/0004-6361/201833910

—. 2020c, A&A, 641, A5, doi: 10.1051/0004-6361/201936386

Polenta, G., Marinucci, D., Balbi, A., et al. 2005, J. Cosmol. Astropart. Phys., 2005, 001, doi: 10.1088/1475-7516/2005/11/001

Pordes, R., Petravick, D., Kramer, B., et al. 2007, J. Phys.: Conf. Ser., 78, 012057, doi: 10.1088/1742-6596/78/1/012057

Posada, C. M., Ade, P. A. R., Ahmed, Z., et al. 2015, Supercond. Sci. Technol., 28, 094002, doi: 10.1088/0953-2048/28/9/094002

—. 2018, J Low Temp Phys, 193, 703, doi: 10.1007/s10909-018-1924-1

Reichardt, C. L., Patil, S., Ade, P. A. R., et al. 2020, arXiv:2002.06197 [astro-ph]. https://arxiv.org/abs/2002.06197

Richards, P. L. 1994, Journal of Applied Physics, 76, 1, doi: 10.1063/1.357128

Riess, A. G., Casertano, S., Yuan, W., Macri, L. M., & Scolnic, D. 2019, ApJ, 876, 85, doi: 10.3847/1538-4357/ab1422

Rotermund, K., Barch, B., Chapman, S., et al. 2016, J Low Temp Phys, 184, 486, doi: 10.1007/s10909-016-1554-4

Seljak, U., & Zaldarriaga, M. 1997, Phys. Rev. Lett., 78, 2054, doi: 10.1103/PhysRevLett.78.2054

Sfiligoi, I., Bradley, D. C., Holzman, B., et al. 2009, in 2009 WRI World Congress on Computer Science and Information Engineering, Vol. 2, 428–432, doi: 10.1109/CSIE.2009.950

Shoemaker, D. H. 1980, Master's Thesis, Massachusetts Institute of Technology

Silva-Feaver, M., Arnold, K., Barron, D., et al. 2018, J Low Temp Phys, 193, 600, doi: 10.1007/s10909-018-2052-7

Smecher, G., Aubin, F., Bissonnette, E., et al. 2012, IEEE Transactions on Instrumentation and Measurement, 61, 251, doi: 10.1109/TIM.2011.2161012

Sobrin, J. A., Ade, P. a. R., Ahmed, Z., et al. 2018, in Millimeter, Submillimeter, and Far-Infrared Detectors and Instrumentation for Astronomy IX, Vol. 10708 (International Society for Optics and Photonics), 187–197, doi: 10.1117/12.2314366

Suzuki, A. 2013, PhD thesis, University of California, Berkeley

Suzuki, A., Arnold, K., Edwards, J., et al. 2012, J Low Temp Phys, 167, 852, doi: 10.1007/s10909-012-0602-y

Suzuki, A., Ade, P., Akiba, Y., et al. 2016, J Low Temp Phys, 184, 805, doi: 10.1007/s10909-015-1425-4

Suzuki, A., Ade, P. A. R., Akiba, Y., et al. 2018, J Low Temp Phys, 193, 1048, doi: 10.1007/s10909-018-1947-7

Tegmark, M. 1997, ApJ, 480, L87, doi: 10.1086/310631

Tristram, M., Macías-Pérez, J. F., Renault, C., & Santos, D. 2005, Mon Not R Astron Soc, 358, 833, doi: 10.1111/j.1365-2966.2005.08760.x

Trombetti, T., Burigana, C., Zotti, G. D., Galluzzi, V., & Massardi, M. 2018, A&A, 618, A29, doi: 10.1051/0004-6361/201732342

Tucker, C. E., & Ade, P. A. R. 2006, in Millimeter and Submillimeter Detectors and Instrumentation for Astronomy III, Vol. 6275 (International Society for Optics and Photonics), 62750T, doi: 10.1117/12.673159

Wong, K. C., Suyu, S. H., Chen, G. C.-F., et al. 2020, Mon Not R Astron Soc, 498, 1420, doi: 10.1093/mnras/stz3094

Woodcraft, A. L. 2005, Cryogenics, 45, 421, doi: 10.1016/j.cryogenics.2005.02.003

Zaldarriaga, M. 2001, Phys. Rev. D, 64, 103001, doi: 10.1103/PhysRevD.64.103001

Zaldarriaga, M., & Seljak, U. 1997, Phys. Rev. D, 55, 1830, doi: 10.1103/PhysRevD.55.1830